



Influence des montants arrières arrondis sur l'aérodynamique des véhicules bicorps

Giacomo Rossitto

► To cite this version:

Giacomo Rossitto. Influence des montants arrières arrondis sur l'aérodynamique des véhicules bicorps. Autre. ISAE-ENSMA Ecole Nationale Supérieure de Mécanique et d'Aérotechnique - Poitiers, 2016. Français. NNT : 2016ESMA0010 . tel-02402039

HAL Id: tel-02402039

<https://theses.hal.science/tel-02402039>

Submitted on 10 Dec 2019

HAL is a multi-disciplinary open access archive for the deposit and dissemination of scientific research documents, whether they are published or not. The documents may come from teaching and research institutions in France or abroad, or from public or private research centers.

L'archive ouverte pluridisciplinaire **HAL**, est destinée au dépôt et à la diffusion de documents scientifiques de niveau recherche, publiés ou non, émanant des établissements d'enseignement et de recherche français ou étrangers, des laboratoires publics ou privés.

THÈSE

Pour l'obtention du grade de

DOCTEUR DE L'ÉCOLE NATIONALE SUPÉRIEURE DE MÉCANIQUE ET D'AÉROTECHNIQUE

(Diplôme National - Arrêté du 25 mai 2016)

École Doctorale : Sciences et Ingénierie en
Mécanique, Matériaux, Energétique et Aéronautique

Secteur de Recherche : MÉCANIQUE DES MILIEUX FLUIDES

Présentée par

Giacomo ROSSITTO

Influence of afterbody rounding on the aerodynamics of a fastback vehicle

Directeurs de thèse : **Jacques BORÉE**

Co-encadrant : **Valérie FERRAND**

Soutenue le 7 Septembre 2016 devant la Commission d'Examen

JURY

| | | |
|--------------|-------------------------------------|------------|
| M. Passmore | Professeur, Loughborough University | Rapporteur |
| J.L. Aider | Directeur de Recherche CNRS, ESPCI | Rapporteur |
| D. Lo Jacono | Maître de conférence, IMFT | Examineur |
| O. Cadot | Professeur, ENSTA-Paris Tech | Examineur |
| J. Borée | Professeur, ENSMA | Examineur |
| V. Ferrand | Maître de conférence, ISAE-SUPAERO | Examineur |
| C. Sicot | Maître de conférence, ENSMA | Examineur |
| F. Harambat | Ingénieur-Docteur, PSA | Examineur |

Aerodynamics is for those who cannot manufacture good engines.

Enzo Ferrari

Acknowledgements

I would like to thank the Jury for their time reviewing the manuscript and for the questions during the defense. They underlined the need of continuing with this project and pointed out the interest of answering some remaining questions in order to increase the knowledge about this topic.

I would like to thank the "supervisors team". Each of you brought to this PhD knowledge, experience and personality. Even though the distance was not helpful, you have always been able to find a way to share your ideas and advices. I would also like to thank all the members of P' for the discussions during my short stay at ENSMA.

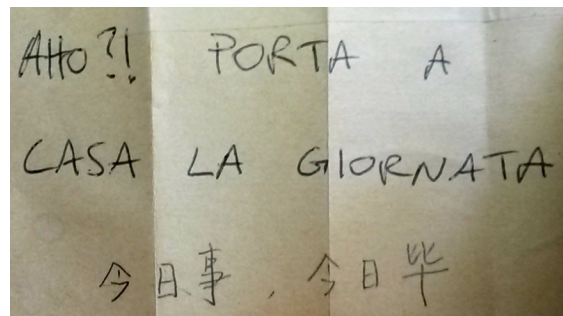
I also need to thank the team in PSA for sharing with me all their knowledge. Every day I learned from you something new, even though sometimes not directly useful for this manuscript!

Since this PhD was mainly experimental, many people were involved in providing CAO, models, data and everything that was needed in order to perform all tests reported in this work. I'm deeply thankful to them, because it would have been impossible to do everything alone. Thanks also to everyone who helped me to discover the magic world of numerical simulations, meshing, seeding and averaging.

I had a post-it for 2 years under my screen with "porta a casa la giornata" [bring your day home] and I should thank the writer for such inspiring note. On the same post-it, there was added a translation in Chinese some months later, but I still doubt on the translation! (Please help me to find out!).

I should really thank all the PhD students in PSA from the "bench" for sharing with me this journey. You all welcomed me warmly and shared with me the important PhD student tricks that are vital for starting a PhD. Thank you Cyril, to be a colleague and a friend. Thanks to the Italian PhD community for increasing the volume of the conversations.

I also need to thank to my family for their support despite the distance and to Žofia for all the love, you were by my side all these years and you supported me at any circumstances.



Grazie a tutti!

Résumé étendu

L'introduction est consacrée à la présentation du contexte industriel et à l'état de l'art sur le sujet. Pour réduire l'impact environnemental des gaz à effet de serre, depuis 2007 la Communauté européenne impose graduellement aux constructeurs automobiles des objectifs de limitation des émissions de CO₂. La traînée aérodynamique représentant la plus grande source de résistance à l'avancement d'un véhicule à haute vitesse, les constructeurs optimisent la forme du véhicule pour réduire la traînée aérodynamique au maximum. La forme optimale pour réduire la traînée étant la même pour tous les constructeurs automobiles, la perte de la signature visuelle de la marque est un réel problème.

Pour garder une distinction de style, des véhicules avec des montants arrière fortement arrondis ont fait récemment leur apparition. La littérature sur l'influence des arrondis sur l'écoulement autour de formes simplifiées est donc présentée. Les structures principales de l'écoulement de la partie arrière d'une automobile sont aussi rappelées au lecteur avant de discuter un peu plus les études autour de "bluff bodies". L'écoulement autour du corps d'Ahmed (un modèle de voiture fortement simplifié mais qui représente fidèlement les principales structures d'écoulement de la partie arrière d'un véhicule) avec un angle de lunette de 25 degrés est alors discuté. Cette géométrie classique présente des arêtes vives et est à l'origine d'un sillage tridimensionnel complexe avec une bulle de recirculation sur la lunette, des tourbillons longitudinaux générés par les arêtes latérales ainsi qu'une paire de recirculations contrarotatives dans le sillage proche. Les différentes stratégies de contrôle, actives ou passives sont aussi évoquées.

Le chapitre 2 présente les moyens d'essais, les moyens de mesures et les géométries utilisées lors de cette étude. Dans le même chapitre la méthodologie mise en œuvre pour les simulations numériques est également présentée. La soufflerie utilisée dans cette thèse est la soufflerie de PSA de la Ferté Vidame, de type Eiffel. Les différentes maquettes testées sont présentées. Le premier modèle utilisé est le corps d'Ahmed. Sept différents arrières ont été étudiés pour comprendre l'influence du rayonnement des arêtes arrière sur le développement de l'écoulement. Le deuxième maquette étudiée, de géométrie plus complexe, représente un modèle simplifié d'une Citroën C4. Le troisième modèle est un véhicule appelé "Crosshatch" censé représenter les silhouettes des futurs SUV compacts du groupe PSA. Pour ce modèle également, différents rayons du montant baie arrière ont été testés. Les techniques expérimentales mises en œuvre au cours de la thèse sont détaillées dans la suite de ce chapitre. Le fonctionnement de la balance aérodynamique à 6 composantes ainsi que les mesures de pression sont rappelés. Les techniques de mesures optiques utilisées telles que la vélocimétrie par images de particules 2D2C basse fréquence (7Hz) et la PIV stéréoscopique 2D3C(SPIV) sont détaillées ainsi que la quantification des incertitudes liées à ce type de système de mesure. Ensuite la méthodologie mise en œuvre pour les simulations numériques est présentée. Les simulations sont réalisées avec le logiciel PowerFLOW (Exa) basé sur une approche de type Lattice-Boltzmann (LBM). Les comparaisons entre des résultats expérimentaux et des simulations numériques mises en œuvre sur le corps d'Ahmed et sur le modèle réaliste sont satisfaisantes. Le critère d'identification des tourbillons (Gamma 1 et 2) basé sur une approche géométrique est introduit. La dernière partie de ce chapitre est dédiée à une discussion sur les problématiques générées par l'utilisation des modèles de forme réduite dans une soufflerie aérodynamique avec un sol fixe. Les effets du nom-

bre de Reynolds et l'influence du sol défilant sont ainsi discutés. De plus, des essais préliminaires numériques sont reportés pour discuter de la robustesse des résultats liés aux modifications de forme de la partie arrière en fonction de la partie avant du véhicule.

Le chapitre 3 constitue la partie principale et il présente les principaux résultats permettant d'évaluer l'influence du rayonnement des arêtes arrière sur le sillage d'un corps d'A Ahmed. Dans la première partie, l'influence du rayonnement des arêtes sur les coefficients aérodynamiques est discutée. L'influence du rayon de courbure sur le développement de la séparation de l'écoulement sur la lunette arrière et le changement d'organisation du sillage proche sont analysés grâce aux torseurs aérodynamiques ainsi que les visualisations de pression pariétale et la vélocimétrie laser. Avec un rayonnement de l'arête à la fin du toit l'écoulement reste attaché sur la lunette et, en plus de la disparition de la bulle de décollement sur la lunette, les structures contrarotatives dans le sillage proche sont nettement symétrisées. Cette modification d'écoulement se traduit par une réduction locale des dépressions sur la lunette et sur le culot, ce qui explique la réduction de traînée (allant jusqu'à 16%) Ensuite, l'influence du rayonnement des arêtes latérales est analysée. Cette modification géométrique influence directement l'origine des tourbillons longitudinaux qui sont générés sur les montants latéraux avec une arête vive. La réduction d'intensité de ces structures permet un gain de pression sur la lunette inclinée (ce qui génère une réduction locale de traînée) mais est accompagné malheureusement d'une réduction de pression importante sur la partie verticale de la maquette (augmentation locale de traînée). La compensation des effets de traînée est mise en évidence aussi par la mesure d'effort via la balance aérodynamique car, malgré ces importants changements dans le sillage, la traînée globale n'est modifiée que de 1%. La dernière configuration analysée est celle qui présente à la fois un rayon de courbure sur le toit et un rayon de courbure sur le côté. Cette configuration est intéressante car sa comparaison avec le modèle présentant uniquement un arrondi sur le toit, permettra de bien comprendre les effets des montants latéraux arrondis sur les efforts aérodynamiques et le développement du sillage. Les enduits visqueux permettent de visualiser le décalage de l'origine des tourbillons sur les arêtes latérales (C-pillar vortex) et aussi la manière dont une grande partie de l'écoulement contourne l'arête arrondie. Les champs de vitesse perpendiculaires à l'écoulement obtenus par SPIV, mettent en évidence une répartition latérale du rotationnel très différente du cas de référence à angle vif. Ces modifications modifications sont attribuées au comportement des tourbillons longitudinaux. En effet, la composante longitudinale du rotationnel est distribuée dans les couches limites au décollement et donc sur l'ensemble du sillage proche, au lieu d'être concentrée d'abord dans les tourbillons longitudinaux. Une quantification de l'évolution longitudinale de la circulation dans le sillage proche est proposée. Cette évolution démontre que le "downwash", induit par l'écoulement latéral qui pénètre sur la lunette, impose une forte rotation selon l'axe longitudinal. Finalement une description de la structure du sillage est proposée avec des visualisations numériques et des schémas de synthèse.

Le chapitre 4 analyse l'influence des rayons de l'arête latérale sur une forme plus réaliste de véhicules réalisée en collaboration avec le département de "style" de PSA. Quatre rayons différents sur le côté sont étudiés pour comprendre l'effet d'un rayonnement progressif sur le développement des tourbillons longitudinaux. Comme pour le corps d'A Ahmed, les effets bénéfiques en termes de réduction de traînée sont contrebalancés par la réduction de pression sur le culot. La réduction de traînée est

donc de seulement 2% pour le modèle fortement arrondi en comparaison avec le modèle présentant des arêtes vives sur le côté. La réduction de la portance est importante, comme dans le cas du corps d’Ahmed, pour la configuration avec des montants arrière latéraux arrondis (-27%). Les performances en vent latéral sont ensuite étudiées. Il apparait clairement que l’utilisation des arêtes fortement arrondies dégrade la stabilité latérale du véhicule. En effet, pour le plus petit arrondi testé, le moment de lacet est augmenté de presque 10%, alors que la portance subit une augmentation importante. Les visualisations de pression issues des simulations numériques permettent de mettre en évidence les mécanismes physiques responsables de cette augmentation du moment du lacet. Une première stratégie de contrôle passif d’écoulement est proposée grâce à l’utilisation d’un rayon non constant. En effet cette solution permet de combiner les effets positifs d’un montant arrondis en ligne droite et de réduire ses effets négatifs en dérapage. D’autres stratégies de contrôle passif sont proposées à la fin du chapitre. Des spoilers de différentes tailles sont placés à la fin de la lunette et permettent de réduire soit la traînée soit la portance du véhicule. Les différents spoilers sont testés pour l’ensemble des modèles. Un comportement différent de performance du spoiler est remarqué en fonction de la valeur de l’arrondi sur l’arête latérale. L’utilisation d’un diffuseur pour faire varier l’angle du sous-plancher est aussi testé. Le diffuseur permet de réduire sensiblement la traînée et n’est pas sensible aux rayons des montants latéraux arrière.

Après un dernier chapitre de conclusions et perspectives où les possibles nouvelles stratégies de contrôle et d’analyse d’écoulement sont discutées, deux annexes sont reportées. Dans l’annexe 1 les essais expérimentaux sur le modèle simplifié de Citroën C4 sont reportés tandis que l’annexe 2 présente les essais sur une Citroën C5 à l’échelle 1 effectués dans la soufflerie S2A.

Contents

| | | |
|----------|---|-----------|
| 1 | Introduction | 1 |
| 1.1 | Context | 1 |
| 1.1.1 | CO ₂ emission overview | 1 |
| 1.1.2 | Importance of aerodynamics in car emissions | 2 |
| 1.2 | History of automotive drag reduction | 4 |
| 1.2.1 | Towards optimal shapes | 5 |
| 1.3 | Rounded edges geometries | 8 |
| 1.3.1 | Application to simplified vehicle models | 9 |
| 1.4 | 25° Ahmed body | 10 |
| 1.4.1 | Natural flow | 10 |
| 1.4.2 | Flow control | 12 |
| 1.5 | Outline of the Thesis | 14 |
| 2 | Methods | 15 |
| 2.1 | Experimental methods | 15 |
| 2.1.1 | La Ferté Vidame Wind tunnel | 15 |
| 2.1.2 | Models | 16 |
| 2.1.3 | Measurements techniques | 19 |
| 2.2 | Numerical method: <i>PowerFLOW</i> settings | 22 |
| 2.3 | Analysis methods for vortex identification | 26 |
| 2.4 | Discussion about the wind tunnel tests | 29 |
| 3 | Effects of edges rounding on the Ahmed Body | 33 |
| 3.1 | Global analysis of the aerodynamic forces | 34 |
| 3.1.1 | Aerodynamic coefficients | 34 |
| 3.1.2 | Interpretation of static wall pressure distribution and velocity fields in the plane of symmetry | 38 |
| 3.2 | 3D effects of pillar rounding on the near wake development | 48 |
| 3.2.1 | Oil flow visualizations | 48 |
| 3.2.2 | Cross-flow analysis | 49 |
| 3.2.3 | Schematic representation of the wake | 59 |
| 3.3 | Towards a realistic model | 61 |

| | | |
|----------|---|-----------|
| 4 | Effects of progressive afterbody rounding on the realistic shape vehicle | 63 |
| 5 | Conclusion and outlook | 65 |
| 5.1 | General synthesis | 65 |
| 5.2 | Perspectives | 66 |
| A | Wind tunnel test over a scaled simplified Citroën C4 | 71 |
| B | Full scale wind tunnel test over a Citroën C5 | 75 |
| C | Articles | 85 |

Chapter 1

Introduction

Contents

| | | |
|------------|---|-----------|
| 1.1 | Context | 1 |
| 1.1.1 | CO ₂ emission overview | 1 |
| 1.1.2 | Importance of aerodynamics in car emissions | 2 |
| 1.2 | History of automotive drag reduction | 4 |
| 1.2.1 | Towards optimal shapes | 5 |
| 1.3 | Rounded edges geometries | 8 |
| 1.3.1 | Application to simplified vehicle models | 9 |
| 1.4 | 25° Ahmed body | 10 |
| 1.4.1 | Natural flow | 10 |
| 1.4.2 | Flow control | 12 |
| 1.5 | Outline of the Thesis | 14 |

1.1 Context

1.1.1 CO₂ emission overview

Greenhouse gases concentration in the atmosphere have historically varied as a result of many natural processes, e.g. solar activities and volcanic eruptions. However, since the Industrial Revolution, human beings have added a significant amount of greenhouse gases by burning fossil fuels and cutting down forests increasing the CO₂ concentration by 31% since 1750 [1]. Because greenhouse gases absorb and emit heat, increasing their density will tend to have a warming effect [2]. The best projections show that average global temperatures are likely to increase within the range of 1.8°C to 4.0 °C by the end of the century depending on the amount of carbon emissions [3]. Global warming, among many catastrophic effects, could lead to a sea level increase of 50 cm by the end of the current century. Six-hundred millions peoples lives less than 1m above the sea level. Roughly one in ten person in the world will be directly impacted by the rising seas [4].

The largest source of CO₂ emissions is the combustion of fossil fuels such as coal, oil and gas in power

plants, automobiles, industrial facilities and other sources. *Figure 1.1* reports the percentage of the European greenhouse gas emissions by sector and modes of transportation. Transport emission represents 25% of the total and its main contributions are navigation 13%, aviation 13% and road transportation 72%. Indeed car transportation represents 12% of carbon dioxide of EU emissions, the main greenhouse gas. In 2007, to reduce these emissions, the European Union has fixed the objective of vehicle emissions to 95 gCO₂/km in 2020 [5]. A first target was set to 130 gCO₂/km in 2015. The 2015 and 2020 targets represent reductions of 18% and 40% respectively compared with the 2007 fleet European average of 158.7 gCO₂/km. The 2015 goal has been attained already in 2013 when the average specific emissions of the new European car fleet was 126.7 gCO₂/km [6]. The 2020 target, that required 25% reduction with respect to 2013, seems very difficult because the market trend is towards vehicles with an important frontal surface area, i.e. high drag. In 2014, this type of vehicle called SUV (sport utility vehicle), represented 20% of the European market share and it has experienced +22% growth in sales with respect 2013 [7]. Some European countries have already started negotiations to postpone the 95 gCO₂/km target to 2024 [8,9]. A first compromise has already been made with a grant of a short phase-in period for the 95 gCO₂/km target. Indeed in 2020, “only” 95% of each manufacturer’s new cars will have to comply with the limit imposed while 100% of the new cars will have to respect the target in 2021. If the average CO₂ emissions of a manufacturer’s fleet exceed its limit value, the manufacturer has to pay an excess emissions premium for each car registered [5].

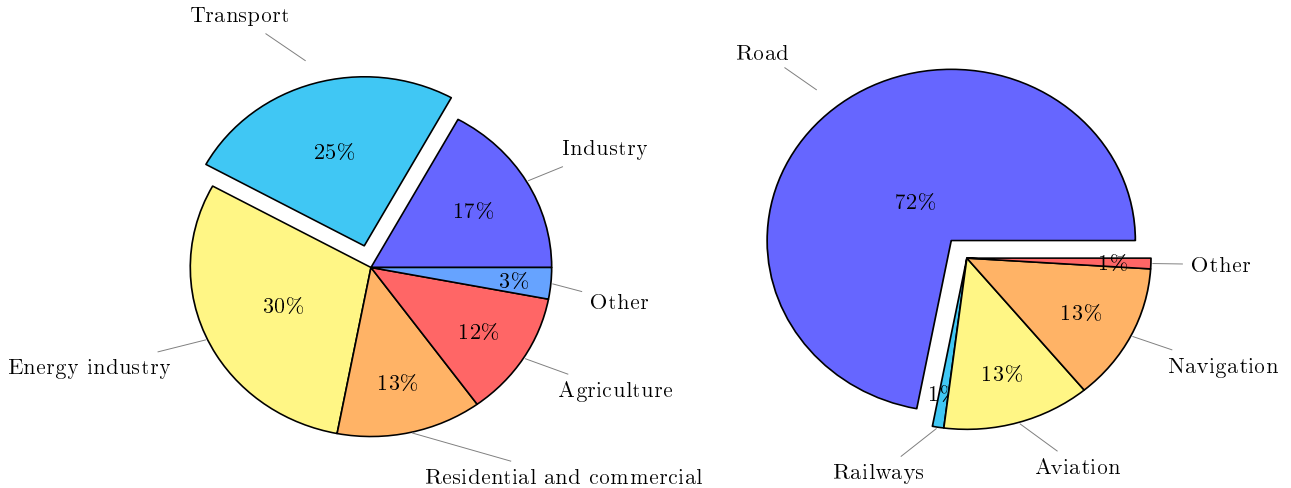


Figure 1.1: European greenhouse gas emissions by sector (left) and mode of transport (right) in 2012 [5]

1.1.2 Importance of aerodynamics in car emissions

Aerodynamics drag, as shown in *figure 1.2*, is the main source of resistance. At 50km/h, aerodynamics drag is 50% of the total drag, but at 130km/h it is almost 80% [11]. The rolling resistance is considered not dependent on speed. Assuming 10% of reduction in the drag coefficient, a reduc-

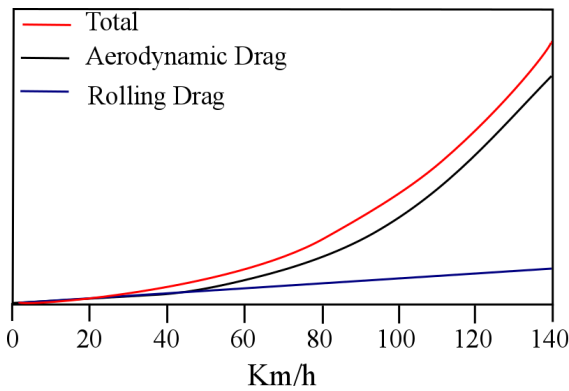


Figure 1.2: Aerodynamic drag and rolling drag Vs the vehicle speed [10]

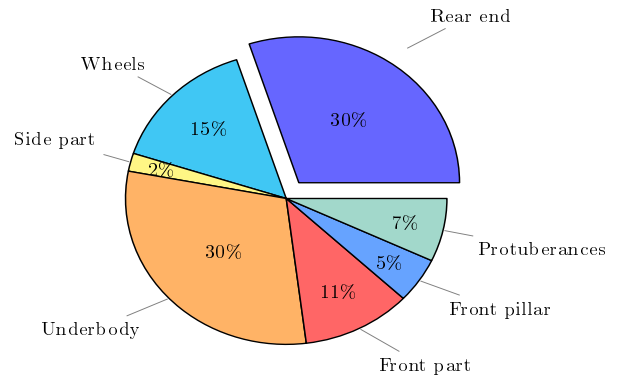


Figure 1.3: Locations of drag generation on road vehicles [Internal source PSA]

tion of 0.21/100km at a stable speed of 90 km/h and about 0.3l/100km on a motorway route is achieved [12]. The same drop of drag reduces the CO₂ emissions by 1g/km in the NEDC cycle [13]. The ambitious target of 95 gCO₂/km cannot be reached alone by aerodynamic improvements. At the same time many others solutions should be explored as engine efficiency, hybrid systems to recover the breaking energy as well vehicles lightening can help all together to reach the target. Nevertheless the role of aerodynamics in car emissions is certainly clear and many efforts have to be done to optimize the shape of the vehicle in order to reduce its aerodynamic drag. *Figure 1.3* reports some orders of magnitude of the sources of drag on a standard vehicle. Of course this contribution is slightly depending on the “family of the car” i.e. fastback, notchback and squareback [14]. Roughly, the upper part of the car contributes to 45% of the total drag, the underbody accounts for 30% and wheels for 15%. The most common solutions to reduce drag are listed in what follows. A simplified vehicle is drawn in *figure 1.4* to represent the nomenclature of the main components of a vehicle.

To reduce the front part drag, variable air intake made its appearance few years ago [15]. At stable high speed on highway the air intake is closed since the need to cool down the engine is reduced. The mechanism is base on the fact that the pressure loss due to the flow that enters the under-hood is higher than the pressure loss due to the stagnation area in the vehicle front part. This device can reduce almost 10% of drag at stable speed of 130km/h [13]. Regarding the forebody, the lower is the stagnation point the better it is for drag recovery [16].

Modern underbody panels, initially applied only under the power train, are used to cover more than half underbody surface to reduce drag and lift [17,18]. The angle of the windshield and the radius of the front pillars are the main parameters influencing the front upper part drag. Rear view mirrors can be optimized to reduce drag, noise in the cabin and dirt accumulation on the side window [19]. Nowadays engineers are ready to replace them by cameras but some legal impediments are still present. Tires are normally produced by an external company so the aerodynamic engineers have not much room for maneuver on the shape of the tire itself. Drag reduction is performed changing the shape of the rim [20,21].

In this PhD work particular attention is given to the rear end of the vehicle that contributes for 30%

of the total drag. The rear end is responsible also for the rear lift. Reductions of rear lift and drag are achieved normally with a rear spoiler to impose massive flow separation [22,23]. Unfortunately such devices used to alter the original shape of the vehicle. Vehicles designer are nowadays trying to replace those devices while keeping good performances.

In the next paragraph the history of vehicles drag reduction will be presented focusing on cars rear end. It will be shown that rear end drag and lift reduction can be achieved not only with the addition of an external device, but also with an optimization of the rear pillar geometry.

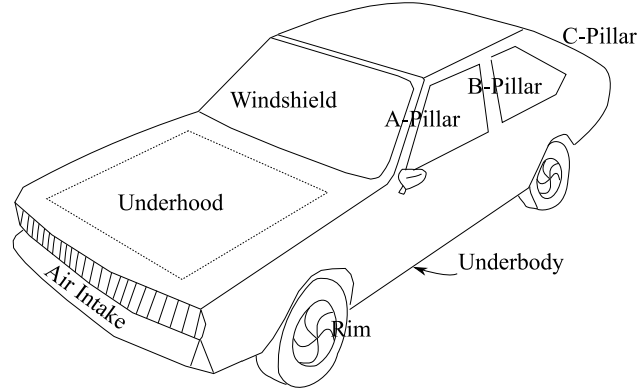


Figure 1.4: Nomenclature of main geometrical features of a vehicle. Redraw from [24]

1.2 History of automotive drag reduction

Reduction of fuel consumption has become a main objective for the automotive industry since 1973, when the first oil crisis occurred. In the early '80s many seminal works appeared related to the flow field analysis around vehicles or simplified models [25]. It is worth citing the work of Ahmed et al. [26] in 1984 who studied the influence of the rear slant angle on drag evolution over a simplified vehicle model (*figures 1.12 and 1.13*). An entire section will be dedicated in what follows to the description of this particular geometry. The work of Ahmed et al. is one of the first work that separated the contributions of the different parts of the model to the total drag thanks to a local integration of surface pressure. Moreover, a detailed wake survey was performed to understand the influence of the slant angles on the side pillar vortices intensity. The sketch of the Ahmed body wake topology still occupies many introduction of scientific papers related to car aerodynamics. In 1984 the wake of simplified models was analyzed also in the work of Bearman [27], Onorato et al. [28] and Hackett et al. [29]. The idea behind these works was to study, through wake analysis, the role of longitudinal vortices in the development of aerodynamic forces over the models. The drag was calculated from the change of longitudinal mean momentum flux between a section upstream and downstream the model. The total drag was decomposed into 3 terms: a total pressure loss, a positive longitudinal velocity deficit in the near wake flow and a loss due to the rotating kinetic energy embedded in the longitudinal vortices. Still in 1984, Sovran presented an analysis of the ambient wind on the aerodynamic drag [30]. An earlier effort to quantify the effects of crosswind

on the aerodynamic work was reported by Buckley et al. in 1975 [31] with the introduction of the "averaged crosswind drag". Taking into account yaw sensitivity increases the complexity of shape optimization. It can occur, in fact, that a vehicle with excellent performances at zero yaw angle results in opposite behavior on a windy day [30]. Since 1984 then, reduction of the aerodynamic drag for future passenger cars was led by those works and it became a priority for many car producers [32]. The important focus on vehicles aerodynamics allowed to decrease rapidly the resistance coefficient C_d , (figure 1.5). The drag coefficient has been reduced by 50% since 1970.

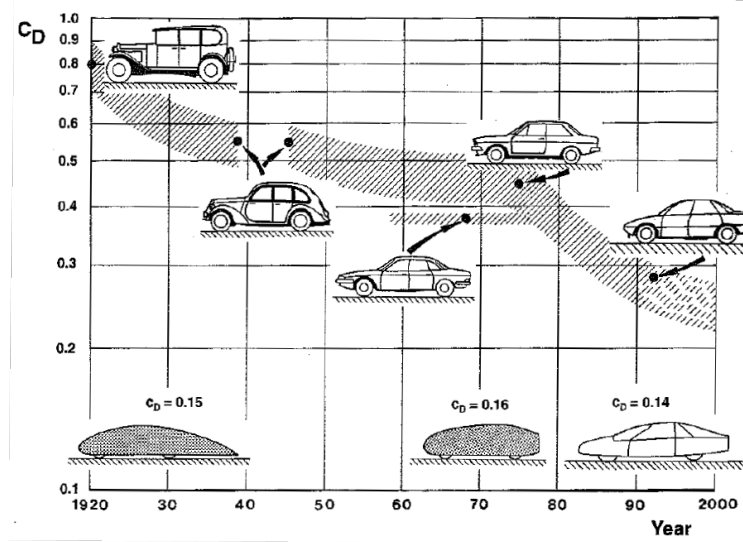


Figure 1.5: History of drag coefficient of European passenger cars in comparison to low drag configurations [16]

1.2.1 Towards optimal shapes

An expert of car aerodynamics, former Volkswagen engineer Dr. W.H. Hucho, author of the reference book "Aerodynamics of Road Vehicles" [16], declared in 1982 that "streamlining will offer the most efficient way of improving fuel economy over the next few years" but "in contrast to the streamlining of the 1930s, aerodynamics will be more cautious, the anxiety that all low-drag cars of the future will look alike is not realistic" [33]. The prediction of Hucho turned out to be truthful as it is possible to see in figure 1.6. The shape of the car moved then from the drop shape, heritage of an aeronautical approach, to a characteristic shape proper to each company.



Figure 1.6: Saab shape evolution from 1930 to 2000 [34]

Unfortunately, in the last 10 years, in contrast with Hucho's statement, the shapes of cars have a tendency to look alike. The author challenges the reader to recognize the brands from the shapes of the cars produced around 2010 shown in *figure 1.7*¹. *Figure 1.8* overlays all the shapes of the eight different cars. The match of the lines is quite striking. In fact, due the previous mentioned imposition by the EU, the search for an optimum shape to reduce drag becomes a vital objective for many companies unable to pay the fee for exceeding gCO₂/km. Car producers unfortunately seems to converge to the same shape.



Figure 1.7: "Different" shapes of cars [35]



Figure 1.8: Silhouettes of the different car from *figure 1.7*

The lost of differentiation among car shapes is a big issue that must be resolved. “Design must reflect the values of a product and a brand”, as recently declared by the director of Peugeot style department [36]. Nowadays, to give back a brand signature, the process of shape optimization has been modified. The shape is imposed by the style department and then it is up to aerodynamic engineers to optimize the drag with relatively little room for manoeuvre in order not to alter the initial stylistic shape. It is a hard task because, as declared by General Motors aerodynamic engineer Nina Tortosa: “what the stylist find beautiful, is not necessarily streamlined [efficient -ed]” [37]. In the “race” to differentiate shapes of modern vehicles, some new geometries have made their appearance in the last years. It is difficult to place them among the three standard classifications (fastback, notchback and squareback). A recent example is the Honda Civic presented in *Figure 1.9*. This car has a very short trunk, typical of notchback, however the angle of the rear window is closer the one related to classical fastback. Moreover it shows pronounced rounding at the end of the roof and on the side rear pillars. To optimize the rear drag of this model, the aerodynamic engineers had to use a rear spoiler in the middle of the rear windscreen. It is interesting to highlight the position of the spoiler. In fact, this device is located in the middle of the rear windscreen impacting sensibly the rear view.

¹**Solution:** Nissan Altima, Toyota Camry, Ford Fusion, Hyundai Genesis, Honda Accord, Chevy Cruze, Audi A4, Lexus LS

A better understanding of the flow field modifications due to afterbody rounding should allow to improve the aerodynamic performances and to keep differentiating the shapes of the future vehicles. For instance removing the rear spoiler while keeping low drag and lift can be an interesting solution for the style improvement.



Figure 1.9: Honda Civic 2.2 i-CTDi 5 Evolution special edition. 2010

It is important to introduce briefly the main averaged flow structures, source of drag, related to the vehicle afterbody. Mean streamlines from numerical simulation over a realistic vehicle model with sharp side pillars are reported in *Figure 1.10*. The lateral shear layer interacting with the flow over the rear slant rolls up into a longitudinal vortex, similar to low aspect ratio wings [26], forming the so-called C-pillar vortex. At the top and bottom edges of the vertical base, the shear layers rolls up into two counter-rotating structures. Depending on the slant angle and the roof edge radius, separation can also occurs at the end of the roof. Rounding the afterbody edges will have a direct influence on the roof separation and on the origin and intensity of the C-pillar vortices.

The use of rounded edges is not a novelty in car aerodynamics, aeronautics and in academic research overs simple bodies. In the next section selected studies about rounded edges will be reported first on simple geometries and subsequently on simplified vehicle models. The analysis of the flow past simple geometries it is of great interest for the study of rounded edges in vehicles aerodynamics. In fact, for both bluff bodies and wings, the characteristic wakes structures as longitudinal vortices or boundary layer separation can be founded in vehicles wakes.

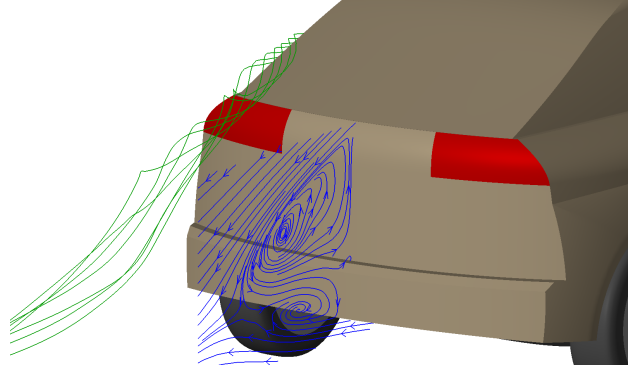


Figure 1.10: Numerical mean streamlines over a realistic model rear end with sharp side pillars.

1.3 Rounded edges geometries

At first, works related to the effects of afterbody rounding on flow separation are reported. Subsequently the works analyzing the effects of side radius on the development of longitudinal vortices will be discussed.

Flow passing a cylindrical body was extensively studied for its interest to tall buildings, suspension bridges, semi-submersible drilling rigs etc. [38]. Regarding to the latter, Bearman et al. [39] investigated the effect of edge radius on the loads experienced by square and diamond shaped cylinders in oscillatory flow. In this experimental analysis, the drag of a square section did not follow a linear trend with edge radius modifications, nevertheless the authors evidenced that drag coefficient in oscillatory flow is found to be more sensitive to corner radius than in steady flow.

Also Okamoto et al., Hu et al. and Tamura et al. investigated numerically and experimentally the aerodynamic forces on square cylinders [38,40,41]. It results that the drag of the cylinder decreases for an increasing edge radius. The vortex formation length and the wake closure length decrease as well. Moreover the maximum vorticity of the vortex shedding at the edge of the squared cylinder and the associated circulation decrease for an increasing radius.

Buresti et al. [42] studied the influence of afterbody rounding on the pressure drag of an axisymmetrical bluff body. The drag was found to have a non-monotonic variation as a function of the afterbody radius. Nevertheless, for radius bigger than $0.1 r/D$, where D is the diameter of the body and r the edge radius, increasing radius decreases drag. It is stated also that the pressure distribution at the end of the body depends also on the property of the boundary layer upstream the rounded edge [43].

Regarding the influence of side rounding on the origin of longitudinal vortices, the recent International Vortex Flow Experiment 2(VFE-2) analyzed the performance of a rounded leading edge delta wing [44]. The flow field over a delta wing is characterized by a pair of vortices generated at the wing apex. The vortices are called leading edge vortices and are located above the leeward (upper) surface of the delta wing. The vortex flow of a typical sharp-edged delta wing is presented in *left side of figure 1.11*. Blunt leading edge, compared to the sharp leading edge, displaces the origin of the primary vortex towards the end of the wing resulting in a the vortex closer to the wing surface

(right side of figure 1.11). At low angle of attack, increasing the leading edge radius decreases the lift force [45]. This could be associated with the decrement in magnitude of the primary vortex [46]. The displaced vortex origin varies also with the angle of attack, the Mach and Reynolds number. Similar effects will be found in *chapter 3* in the development of the rear pillar vortices due to side rounding over a vehicle model.

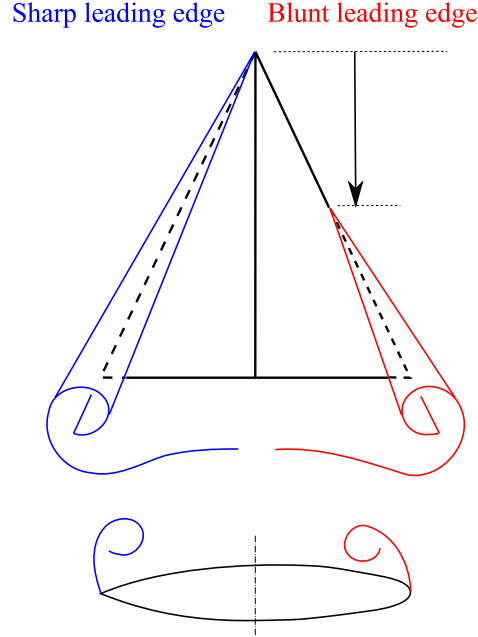


Figure 1.11: Leading-edge bluntness consequences for the primary vortex separation [45].

1.3.1 Application to simplified vehicle models

In 1983, Buchheim et al. in the framework of the Audi 100 development indicated that a rounded C-pillars has the advantage of producing lower drag with respect to the sharp-edged pillars [47]. Gilhaus et al. in 1986 analyzed the influence of rounding the C-pillars on a basic 3/8-scale vehicle model [48]. The rounded pillars reduced drag and rear lift of the model but they increased the yaw moment. The influence of rounded pillars on crosswind was tested also by Howell [49]. The yawing moment has a pronounced increase as soon as the side edges have a small radius. These experimental works analyzed the influence of afterbody rounding only by the use of aerodynamic balance, but unfortunately they did not explain what are the modifications of the flow field resulting in drag reduction or yawing moment increase.

Only recently have very few papers addressed the question of rear edge curvature using advanced flow field visualization techniques, expanding the understanding of the previous works. Thacker et al. showed that rounding the edge between the roof and the rear slant on the Ahmed body results in a 10% drag reduction and 25% lift reduction [50]. Authors attributed this reduction to the fully attached flow over the backlight and the downstream motion of the structures developing in the near wake. The spatial stability of the longitudinal vortices was also analyzed. The elimination of

the separated bubble over the slanted surface does not impact the mean location of longitudinal vortices, but seems to slightly reduce the vorticity fluctuations of the vortex core.

Fuller et al. analyzed the benefits of rounding the rear pillars on the Davis model [51]. Small rounding causes significant differences compared to the sharp pillars in the steady and unsteady behavior of the near wake [52]. They also observed that side rear rounded edges generated weaker longitudinal vortices, resulting in a different wake structure. The rounded edge model results in drag and lift reduction of 11% and 25% respectively. They underlined that in the previous literature this new topology had never been studied.

In a recent paper of Palin et al., the influence of afterbody rounding is mentioned during the analysis of the development of the Tesla Model S [18]. Highly curved rear end were avoided to reduce highly dynamic wake which caused large variation in base pressure.

Based on literature review, it appears that afterbody rounding considerably affected aerodynamic loads and flow fields, but systematic investigation on the effects of changing radii of upper and side backlight edges was not reported. The present PhD work addresses this question initially by rounding alternatively, then simultaneously, the roof and lateral edges of the backlight of vehicle models. The first investigation was conducted over an Ahmed body with 25 degrees rear slant and subsequently the complexity of the model was increased. The choice of such a simple model, far from the shape of a real car, is justified from its wake very similar to the one of a fastback vehicle. Many other models could have been chosen to conduct the first investigation over a simplified vehicle model [25]. It has to be acknowledged that models as the MIRA reference car, the Rover model or the Davis model are more suitable due to their more realistic forebody with respect to the Ahmed model. These models permit then to study also crosswind effects, that are very sensitive to the forebody geometry. The choice of the Ahmed body was motivated by the direct availability of such model for the experimental tests. Moreover many internal validation in the in-house wind tunnel were conducted over this model. The author has also took great advantage of the PSA team knowledge since several PhD works were completed by colleagues using the Ahmed model [53–57]. It is important now to introduce the flow characteristics of the Ahmed body. A short review of the literature of flow control based on this model is presented as well.

1.4 25° Ahmed body

1.4.1 Natural flow

As mentioned earlier, this geometry was proposed by Ahmed et al. in 1984 [26]. The overall dimensions of the body are reported in *figure 1.12*. The original model featured different slant angles, but in what follows, only the 25 degrees rear slant will be analyzed. The nomenclature of flow and geometrical features are presented in *figure 1.13*. The main flow structures are presented to give to the reader a clear picture of the flow field past the Ahmed body.

The sharp edge at the end of the roof generates closed flow separation over the slanted surface,

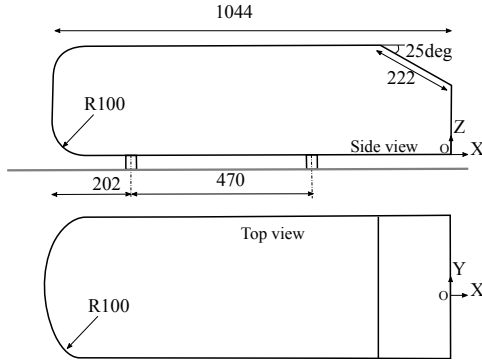


Figure 1.12: Ahmed body overall dimensions (in *mm*) and origin of the Cartesian coordinate system.

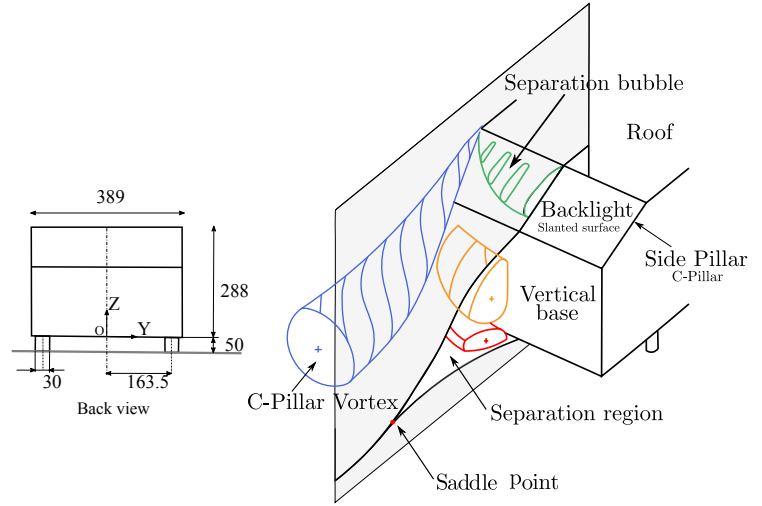


Figure 1.13: Nomenclature of flow and geometrical features generated by the 25 degrees rear slant Ahmed body. Redraw from [26]

figure 1.14. Normally, this separation experiences a reattachment around 75% of the length of the backlight [58]. Some differences are reported in the literature about the position of the reattachment point. The separation appears in fact to be very sensitive to the quality of the upper sharp edge [58]. This problem will be illustrated in *chapter 3*. It may be noted that the position of the separation bubble reattachment point over the slanted surface is also a major challenge of numerical simulations as in [59–61].

The near wake is characterized by two counter-rotating structures generated by the upper and lower shear layer. The length of the separation region is commonly measured with the position of the mean saddle point. Unfortunately a simple 2D analysis of the symmetry plane is not sufficient to describe the entire flow field for this kind of geometry because the side effects due to its low aspect ratio are not negligible [62]. Nevertheless, in the symmetry plane, a correspondence between the length of the recirculation region and the base pressure will be remarked. Increasing the length of the recirculation region reduces the curvature of the separatrix resulting in an increase of base pressure [63–65]. The changing in curvature is associated then to important changes of the mean vertical pressure gradients in the near wake [66].

The sharp side pillars generate longitudinal vortices, the so called C-pillar vortices, presented in *figure 1.15*. As for a wing tip, these vortices owes their existence to a pressure difference. For a finite wing, the pressure difference takes place between the lower surface and the upper surface, while for the rear end of a vehicle, the pressure difference is between the side of the vehicle and the rear window. These vortices are responsible for low pressure foot-print over the backlight side, resulting in a local increase of lift and drag. They also induce a central downwash that influences the pressure over the center line of the backlight [52].

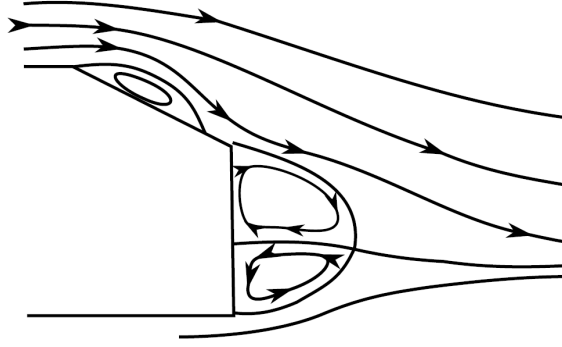


Figure 1.14: Schematics of the flow field characteristic in the symmetry plane of the 25 degrees rear slant Ahmed body [67]

In the next subsection, different strategies to control the flow structures generated by an Ahmed body with 25 degrees slant angle are presented.

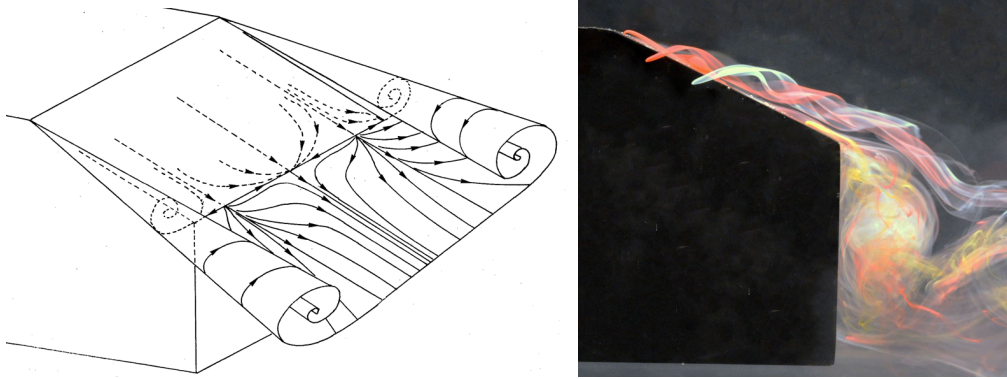


Figure 1.15: Left: skin friction line pattern and detachement surface of C-pillar vortices, Courtesy of J. Déleury. Right: Water tunnel color visualizations in the Cuve “Werlé” from [68]

1.4.2 Flow control

To give an idea of the work done over the Ahmed body, since its first appearance, it is enough to mention that the paper of Ahmed et al. has been cited more than 600 times and 78 times only in 2015! The mean topology of the 25 degrees rear slant flow field was analyzed in the works of [69–71]. New schematic representations of the time-averaged wake flow were proposed with particular focus on the 3D organization of structures in the near wake. Unfortunately those authors do not resolve the thorny issue of the side interaction of the counter-rotating structures in the near wake with the C- pillar vortices. Numerical works are performed by [59, 61, 72–74]. The Ahmed body is actually widely used to validate numerical models in vehicles aerodynamics. It has become common practice to compare either the experimental test or the numerical simulation to the experimental work of Lienhart et al. [75] performed in the framework of the 10th joint ERCOFTAC (SIG-15) and available online.

Among many experimental papers, Thacker et al. [76] and Wang et al. [77] focus on the analysis of the base flow unsteadiness.

Many strategies of flow control are developed over this emblematic geometry and they can be separated between active control and passive control.

For this last category, Beaudoin et al. used flaps on the sides of the model to control the C-pillar vortices and at the end of the roof to force the flow separation [78]. The rear end was equipped as well with horizontal flaps at the end of the rear window to act directly on the wake. Combining all the flaps, drag was reduced by 25% and lift by 105%. Fourrié et al. used a deflector with a variable inclination at the end of the roof [79]. Forcing flow separation at the end of the roof affects the development of the C-pillar vortices resulting in a drag reduction of 9%. Recently Hanfeng et al. analyzed both deflectors and side flaps on 1:2 scale Ahmed model [80]. The maximum vorticity concentration of the trailing vortices seems to be more influenced by the top edge mounted deflector rather than the side one. It resulted, in fact, that the drag reduction is 12% from the first setting and 8% for the latter. Aider et al. used vortex generator(VGs) on a modified rear end of the Ahmed body [81]. The reduction of the longitudinal vortex circulation in the wake was achieved with a row of VGs at the roof end, acting as a spoiler, that forced flow separation. Drag was reduced up to 12% while lift can be even canceled out (more than -100%). Pujals et al. [82] used coherent streamwise streaks over the roof to modify the boundary layer property approaching the sharp edge at the roof end. The maximum drag reduction achieved here being about 10% thanks to the elimination of the separation bubble over the slanted surface. The organization of the separated zone was modified by vertical splitter plate in the work of Gillieron et al. [83]. These devices allowed drag reduction up to 10%.

Active flow control consists mostly on blowing or aspirating at the end of the roof or on the side pillars [84–88]. It is interesting to notice how these localized controls can affect the entire flow field. The suction of the separation zone permits to reduce the rear window drag, while the vertical surface drag unfortunately increases [86]. On the contrary blowing at the edge between the end of the roof and the rear slant seems to have a double positive effect on both the rear window drag on vertical surface drag [87]. Vortex breakdown can be induced as well by continuous and uniform blowing distributed on the side of the rear slant [89]. For a summary of the studies on active flow control, one can refer to [90,91].

Unfortunately, active flow control has rarely seen application in everyday vehicle due to its cost. At first it requires adding elements to the vehicles resulting in a increase of weight and a lost in space for passenger or payload. Secondly active flow control requires energy. Solenoid valves to create pulsed jet required a pressure chamber filled constantly with pressure up to 4 bars [56]. An example of active flow control by active spoiler and MEMS(Micro electro mechanical system) was integrated in the Citroen C-Sportlounge, a concept car presented by Citroen in 2005 [92]. Active flow control using pulsed microjets was tested also on a full-scale production car by Aider et al. [93]. Results proved that it is possible to prevent flow separation over the rear slant of a real full-scale vehicle using micro- perturbations induced by pulsed micro-jets.

This PhD work deals with flow control through shape modification. It will not be considered as shape optimization because no algorithms are used to choose the geometry studied. This low cost

strategy of flow control can find a rapid integration in new vehicles. It helps also to keep style design optimizing small geometry details to improve aerodynamic performances.

1.5 Outline of the Thesis

The manuscript is organized as follows.

After the CO₂ emissions overview and the introduction of the importance of aerodynamics on car emissions, the history of drag reduction was introduced. The use of rounded edges to improve aerodynamics was described for both simple geometry and for vehicles. The Ahmed body was introduced as well to present its characteristic flow structures.

In *Chapter 2* the experimental and the numerical methods are described. A discussion about the wind tunnel tests limitation is proposed as well.

Chapter 3 describes the effects of edges rounding on the Ahmed body. At first, a global analysis of the aerodynamic forces permits to get an overview of the flow modification due to afterbody rounding. At second, a detailed investigation of the near wake development is reported to gain further insight on the influence of afterbody rounding on the near wake development. The necessity of additional test over realist model is discussed at the end of *Chapter 3*.

Chapter 4 is dedicated to the realist model called “Crosshatch”. The effects of progressive afterbody rounding will be presented at zero yaw angle as well as its effects on crosswind performances. The sensitivity of passive flow control to afterbody rounding is presented at the end of *Chapter 4*.

In Appendix A the experimental results over a scaled simplified Citroën C4 are analyzed whereas in Appendix B the experimental results on a real scale Citroën C5 are reported.

Chapter 2

Methods

Contents

| | | |
|------------|--|-----------|
| 2.1 | Experimental methods | 15 |
| 2.1.1 | La Ferté Vidame Wind tunnel | 15 |
| 2.1.2 | Models | 16 |
| 2.1.3 | Measurements techniques | 19 |
| 2.2 | Numerical method: <i>PowerFLOW</i> settings | 22 |
| 2.3 | Analysis methods for vortex identification | 26 |
| 2.4 | Discussion about the wind tunnel tests | 29 |

2.1 Experimental methods

2.1.1 La Ferté Vidame Wind tunnel

The experimental tests presented in this PhD work were performed in the PSA Groupe wind tunnel of La Ferté Vidame (France). The acronym “LFV” will be used in what follows to refer to this wind tunnel. This Eiffel wind tunnel is 52 meters long and has a test section 2 meters high, 5,2 meters wide and 6 meters long. The top view schematic plan is reported in *figure 2.1*. The wind tunnel is equipped with a rain cover at the inlet to avoid blowing rain inside the test section (*figure 2.2*). The models tested are 1/4 scaled models compared to the size of a real car. The characteristic models dimensions are 0.5m width and 1m long. The size of the test section is then enough to avoid wall proximity effects [94]. The wind tunnel blockage ratio is 1.4%. Only the area above the false floor is considered for the calculation. Crosswind test may induce changes in the blockage ratio, but even with the model at 90 degrees of yaw angle, the blockage ratio is lower than 6%, no corrections are then applied to the aerodynamic forces [95]. The wind tunnel maximum speed is 53 m/s. The free stream velocity U_0 was set at 40m/s, yielding a Reynolds number based on the length of the model of $2.6 \cdot 10^6$. All velocities are normalized with U_0 and are noted as starred values. The wind tunnel is equipped with 4 electric engines of 200 kW equipped with rotors of 2,7m of diameter.

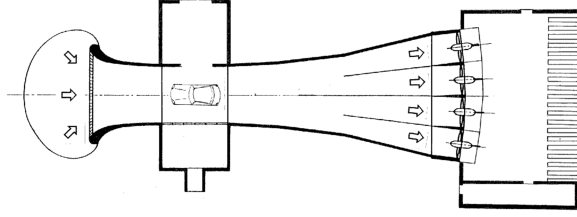


Figure 2.1: Top view plan of the wind tunnel. The flow is from left to right

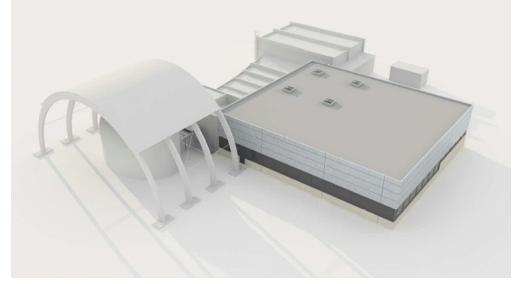


Figure 2.2: 3D rendering of the wind tunnel

2.1.2 Models

Three different scaled models were tested experimentally in the LFV wind tunnel and they are presented hereunder. Furthermore, a full scale Citroën C5 sedan was tested as well in the GIE S2A wind tunnel [<http://www.soufflerie2a.com/>], the resulted will be reported in *Appendix B*.

Ahmed body

The schematic of the model, the relevant dimensions and the coordinates system are reported in *figure 2.3*. The dimensions correspond to the model presented by Ahmed et al. [26]. The reference length, $\xi = 201mm$, is the length of the horizontal projection of the rear window model. Normalized lengths are noted as starred values. The locations of the rounded edges are reported as well in *figure 2.3*. *Rer* stands for the upper edge of the backlight, at the roof junction, *Res* for the side edges and *Rers* for both roof and side radius. The models are then called $R_\alpha S_\beta$, where R stands for *Roof* and S for *Side*. α and β represent the values of the radii expressed as a percentage of the reference length. For instance the standard Ahmed body is $R_0 S_0$, whereas a model with a rounded edge of 10% between the roof and the rear window and sharp side pillars is referred as $R_{10} S_0$.

The maximum side radius for the experimental model was limited by technical hindrances. In fact, to have a good quality surface connection between the side and the roof edges, the rounded side edge is extended upstream the roof edge. Since the experiments were performed by changing just the rear end of the entire model, the maximum radius is imposed by its upstream extension. Numerical simulations with *PowerFLOW* were performed over seventeen different rear ends beforehand to investigate the influence on drag and lift of afterbody rounding over the Ahmed body. The analysis of the numerical simulation helped to select the model tested in the wind tunnel.

Citroën C4

The model and its relevant dimensions are exhibited in *figure 2.4*. Two different rear ends were tested: one with a sharp lateral rear pillars and one with a pillar radius corresponding to 40% of the span of the vehicle. Both rear ends have a rounded edge at the end of the roof to avoid flow separation over the rear window. The results of the wind tunnel experiments over this model are reported in *Appendix A*.

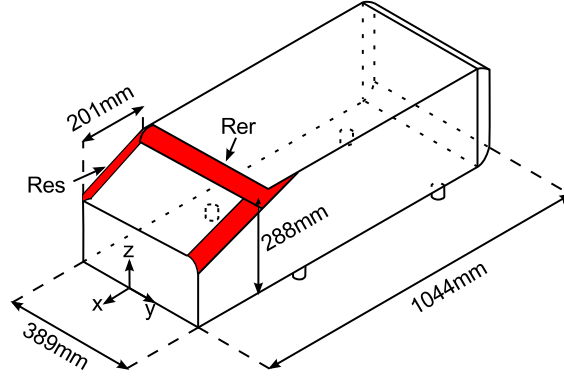


Figure 2.3: Ahmed body and location of the rounded edges. *Rer* stands for Rounded Edge at the end of the Roof and *Res* for Rounded Edge on the Side.

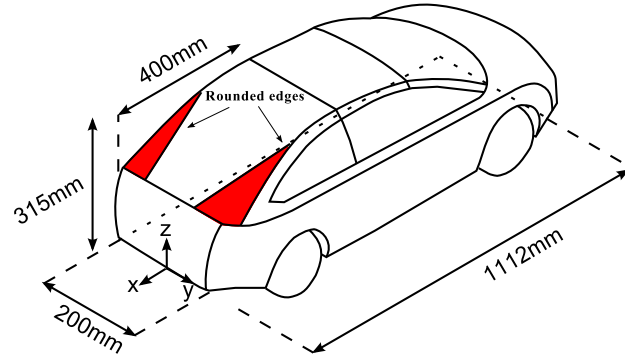


Figure 2.4: Citroën C4 model and location of the rounded edges.

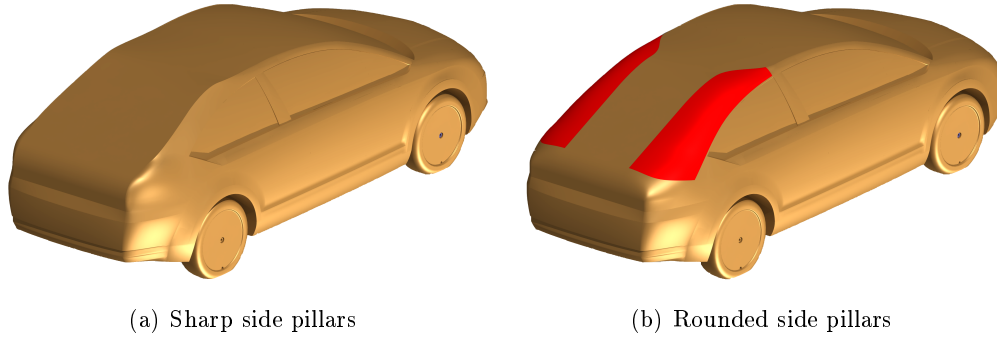


Figure 2.5: Citroën C4 models rendering. The rounded side rear pillars are highlighted in red.

Crosshatch

This model it is called “Crosshatch” by the PSA style department to emphasize the high ground clearance. It is not yet a production vehicles but its style summarized the future market tendency of small SUV. The model and its relevant dimensions are reported in *figure 2.6*. Four rear ends with different side pillar curvature were tested. The curvature radius is given as a percentage of the model span, i.e. 300mm. The model equipped with sharp pillars having 0% radius is referred as S_0 and it is considered as the reference case. The others models are S_8 , S_{20} and S_{40} . All the rear ends have the same curvature at the end of the roof to avoid flow separation. The corresponding radius

is chosen to maximize the room for the rear passengers for a fixed backlight angle of 23° . The horizontal projection of the slanted surface, $\xi = 440\text{mm}$, will be used as reference length. Starred spatial coordinates are normalized by the reference length.

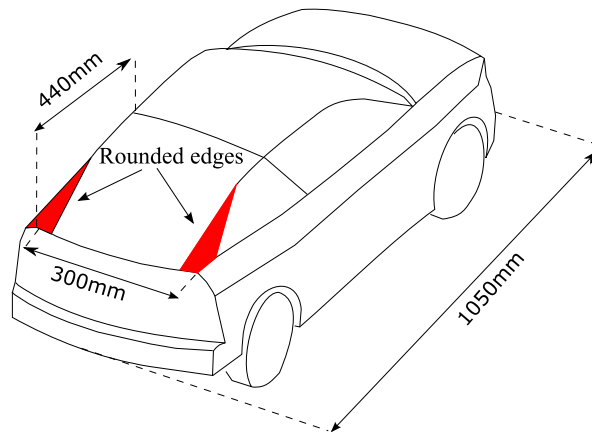


Figure 2.6: Crosshatch model and location of the rounded edges

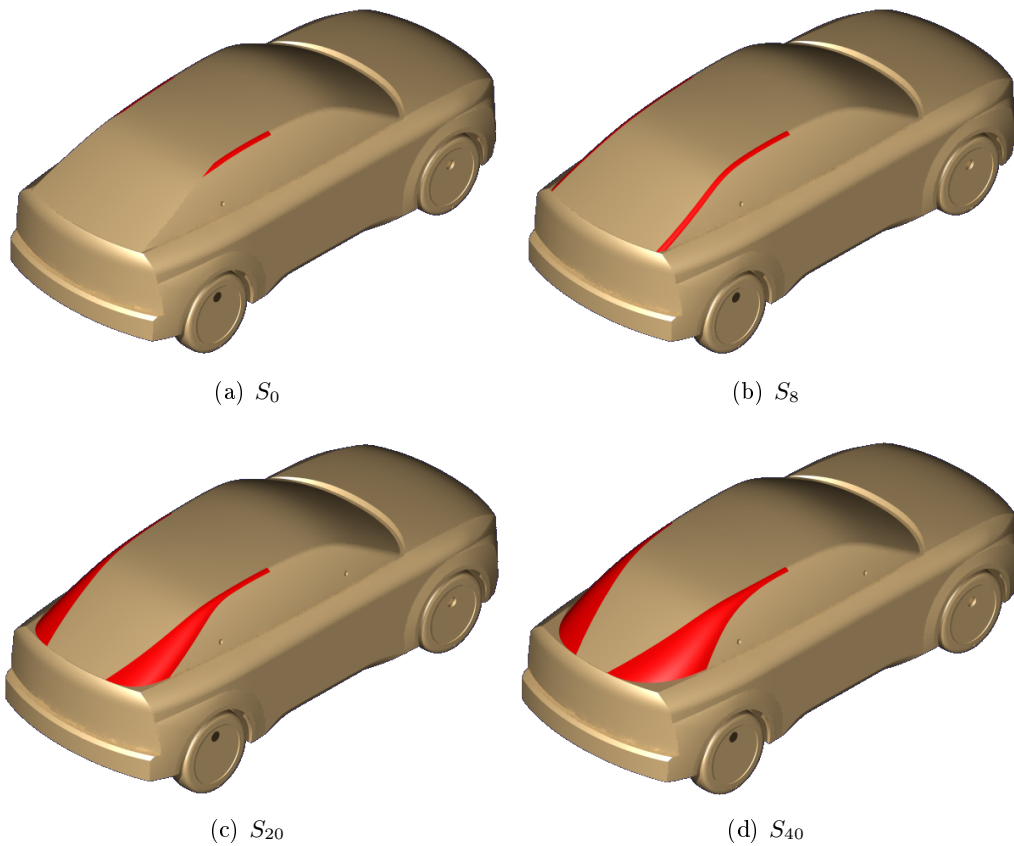


Figure 2.7: Crosshatch models rendering. The rounded side rear pillars are highlighted in red.

2.1.3 Measurements techniques

Aerodynamic balance

To evaluate the aerodynamic forces, a 6 component balance was used. The drag, lift and side force coefficients were calculated as follows:

$$C_{d,l,y} = \frac{F_{d,l,y}}{\frac{1}{2}\rho U_0^2 S}$$

where F is the force measured by the balance, ρ the density of the air, and S the frontal surface area of the model. The precision of the balance was 0.001 for the drag coefficient Cd and 0.002 for the lift coefficient Cl [96]. The balance is able to record both front and rear forces. The yawing moment (CM_Z) is calculated directly by the acquisition software using the front (Cy_{front}) and rear (Cy_{rear}) contribution of the side forces. It is computed by using the middle of the wheelbase and truck as a reference. The measurement period is 60s and the measurement frequency 1 kHz with a low pass filter of 10 Hz [97]. Unfortunately the in-house software used for the balance measurements reports only the averaged results.

Pressure

The static wall pressure coefficient at one point i was computed from the expression:

$$C_P(i) = \frac{P(i) - P_0}{\frac{1}{2}\rho U_0^2}$$

where $P(i)$ is the static pressure of point (i) and P_0 the static pressure measured upstream of the model. The left hand-side of the models was equipped with pressure probes connected to a SCAN-daQ 8000 acquisition system. The PSA acquisition standard foresees an acquisition rate of 40 Hz for 3000 samples, thus giving 75s of time recording. The number of the probes varies according to the different models: for the Ahmed body 115 probes were used while for the realistic models only 100 were used for the Citroën C4 and 35 for the Crosshatch. The static accuracy at the full range of $\pm 1psi$ is $\pm 13Pa$, i.e. $0.015 Cp$ [98].

PIV-SPIV

- For the PIV acquisition two planes iso Y were recorded over the model and subsequently interpolated to generate a plane of 650mm*650mm (*figure 2.8*). The seeding particles are olive oil droplets in the range of $1 - 10 \mu m$ diameter. The laser sheet was set by a 2*120mJ Nd:Yag Quantum Big Sky Laser. All the models are painted in black to limit reflections due to the laser sheet. The Dantec Flowsense 4M mkII (2024pixel*2024 pixels) camera equipped with 105 mm lens generated 462mm*462mm fields of view. 2D PIV was performed on xz planes: $Y^*=0$, $Y^*=0.49$ and $Y^*=0.97$. 800 images were recorded with a 7Hz trigger rate. Post-processing is

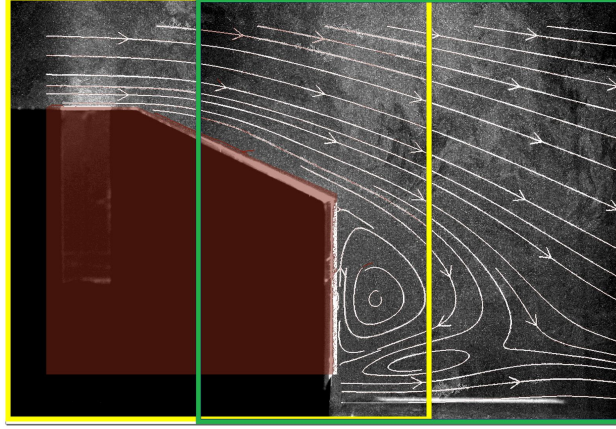


Figure 2.8: Composition of the two planes for the PIV measurements in the isoY plane. In the background the raw pictures of the oil droplets without post-processing. White streamlines are added to show the overall flow.

performed with the Dantec software *Dynamic Studio*. An interrogation domain of 16×16 pixels was used, after an initial window of 32×32 pixels, with an overlap of 50% in the horizontal and vertical directions. Grid resolution was 1.82mm. A SNR (*Signal Noise Ratio*) filter was applied to remove vectors with $\text{SNR} < 1.2$. With a maximum local turbulence intensity of 15% and with 800 number of samples, the error on the mean velocity is 1.03% with a 95% confidence interval according to Montgomery [99] and Benedict et al. [100]. The time between the two pulses was set to $\Delta t = 15 \mu\text{s}$ to ensure an average particle displacement of the measurements of 4 pixels, i.e. 25% of the final interrogation window. Considering that the ability to measure a displacement has an accuracy of ± 0.1 pixels, therefore the total error is 2.5% [101]. *Figure 2.9* reports the percentage variation of moving average with respect to the average as function of the number of samples. It is possible to notice that the mean velocity converges already at 400 images while the standard deviation starts to converge at 600 images.

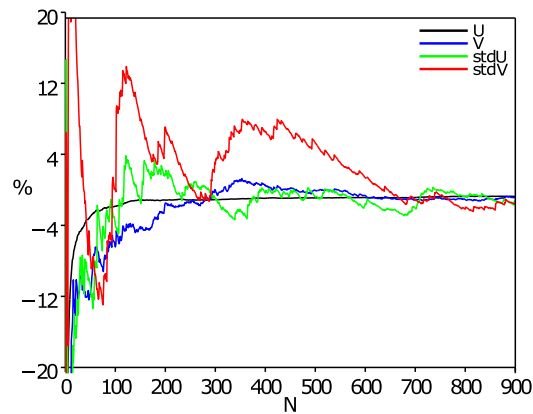


Figure 2.9: Percentage variation of moving average respect to the total average as function of the number of samples

- Stereo-PIV techniques was used to obtain the 3 velocity components of the flow field in crossflow planes (i.e. $X=\text{cst}$). The system was developed during the PhD work of Cyril Jermann [53] and the sketch of the system is reported in *figure 2.10*. The cameras are placed on a motorized traverse moving along X , to be able to record several planes without performing the calibration every time. The angles of the cameras are 45° and 40° . The asymmetry on the angles is due to the fact that the zone of measurement is on the passenger side. The Scheimpflug angle is approximately 4° . The laser sheet thickness is approximately 4mm and the separation time between the two pulses is $\Delta t = 10\mu s$. This combination permits to keep the oil particle inside the laser sheet between the two pulses. The specification of the laser and the post-processing are the same as for the PIV technique. A particular attention was required to choose the aperture of the camera diaphragm since the cameras are pointing to the entrance of the wind tunnel characterized by strong sun light varying during the day. Even though the objectives are capable of an aperture of $f/2$, $f/2.8$ was used to gain in depth of field and to reduce the mean SN ratio [102]. The Defocus Image Control (Nikon patent) of the lens was not used.

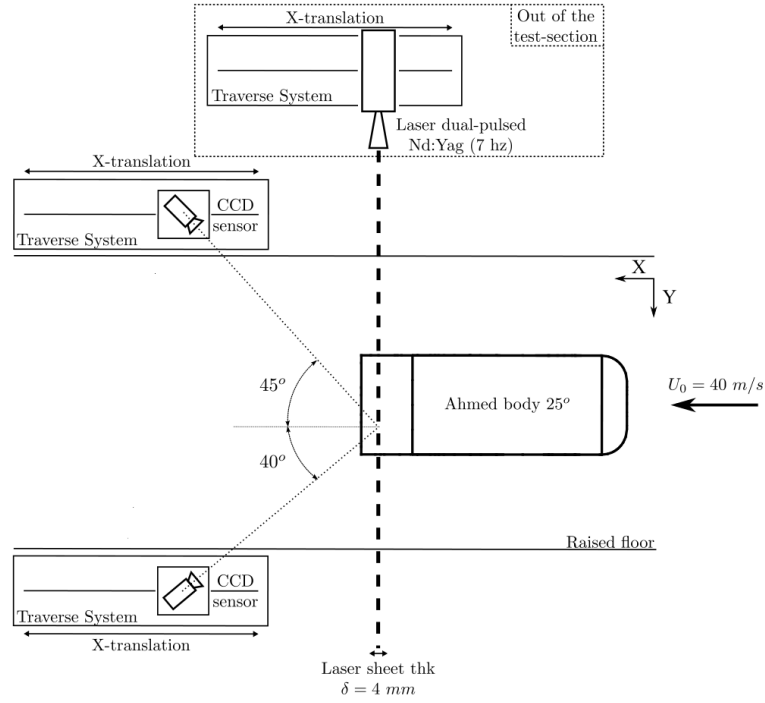


Figure 2.10: Sketch of the S-PIV acquisition system from [53]

Oil flow visualizations

This viscous coating (M10+DD100) used in the experiments, is a mixture detailed in *table 2.1* based on the work of [103]. Once the model rear end was covered with this mixture, the wind tunnel was launched for few minutes.

| Product | Concentration |
|------------------|---------------|
| Vaseline oil | 32.8% |
| Oleic acid | 16.4% |
| Titanium dioxide | 18% |
| Dodecane | 32.8% |

Table 2.1: Oil flow visualization paint.

2.2 Numerical method: *PowerFLOW* settings

The numerical simulations presented in this work are computed with the commercial code *PowerFLOW* (version 5.0c) developed by Exa and based on lattice Boltzmann model (LBM). Most of the simulations were run directly by the Exa engineers.

The idea of LBM is to simulate fluid at microscopic level rather than macroscopic [104]. The flow field can completely be described from a macroscopic point of view, starting from the interaction of particles in a mesoscopic and microscopic scales. Kinetic Boltzmann equation provides information on molecular dynamics, but it also has the advantage of giving clear description of the overall physical fluids and has the possibility to implement calculation algorithms totally parallelizable and moreover has easy implementation of its boundary conditions [105]. In general, a method "Lattice "

consists of a regular mesh with particles that are on its nodes. From an initial state, the configuration of the particles at each time step, evolves in two successive sub-steps: 1 convection, wherein each particle moves to the nearest node in the direction of its speed and 2 collision, which occurs when particles, arriving on a node, interact and change their speed directions. *PowerFLOW* directly simulates the largest turbulent structures and the smallest are modeled. This approach is known as the "Very Large Eddy Simulation "or" VLES ". For the calculation of turbulent coefficients present in the closure equations, *PowerFLOW* exploited the theory of "renormalization group" (RNG), which calculates analytically those unknown coefficients. The boundary layer is modeled by *PowerFLOW* through the laws of the turbulent boundary layer adding a corrective term which depends on the longitudinal pressure gradient. Unfortunately, critical modeling choices result from *had hoc* parameters settings that are not available to the users. It has been therefore used this code as a "black box" model, following the methodology used by PSA. The results wont be used to compared quantitatively the forces predicted by the computations but the simulations will enable to complete the physical understanding by considering 3D velocity and pressure data. Local variable refinement regions VRs are defined to locally allow coarsening the grid by a factor of 2 starting from the *Minimum Level of VR* [106]. The smallest VR (VR=9 in the present numerical simulations) is used in selected zones according to the geometry complexity as reported in *figure 2.11*. If the friction velocity u_τ is approximated by $u_\tau = 5\%U_0$, then the value of the minimum level of VR in terms of wall units is $VR9+ \approx 100$. However, in *PowerFLOW* the boundary layer is modeled until $y^+ \leq 300$ [105].

The simulation setting is resumed in *table 2.2* for the two models tested numerically. The difference in Reynolds number for the realistic model depends on the characteristic length. The time-steps

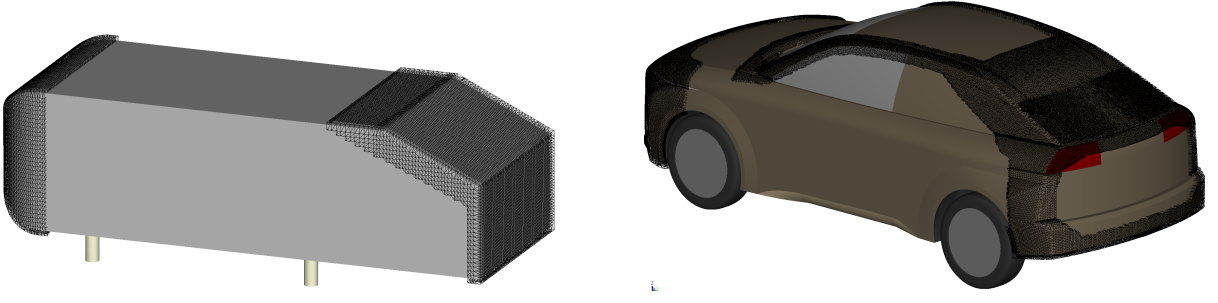


Figure 2.11: Location of the smallest Vr for the numerical simulation.

computed are spatially averaged every 2 voxels (volume cell) and temporally averaged and saved in a frame. A final inverse average is computed with the converged values. The protocol of EXA foresees to plot the aerodynamics forces over the model and to fix (arbitrarily) the frames from which the results is considered to be converged (*figure 2.12*). Only 1151 frames are reported because *PowerFLOW* saves the average of the time-steps results only when all the VR are updated. In fact, the physical time-step δt used on each VR is accordingly proportional to the local grid size [106]. Since the higher VR that contains the simulation domain is VR2 and the finest is VR9, the saving of the results is performed every $2^{9-2} = 128$ time-steps (*figure 2.13*). The Ahmed model simulations were run just for 0.4 sec, that corresponds to approximately 15 convective time scales L/U_0 where L is the length of the body and U_0 the external velocity. A simulation of 552499 time-steps (i.e. 1.5 sec that corresponds to 60 convective time) was computed for the Ahmed body to verify the difference in drag and lift with respect to the short simulation. The drag and lift coefficients resulted in less than 1% discrepancy with the short simulation.

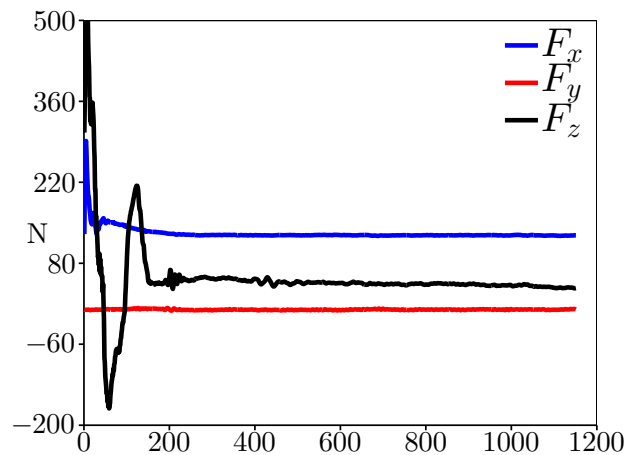


Figure 2.12: Time frames evolution of the reference Ahmed body forces.

Figure 2.14 reports the streamwise profiles comparison over the Ahmed body slanted surface. The experimental blue line is related to the tests performed in the wind tunnel of La Ferté Vidame

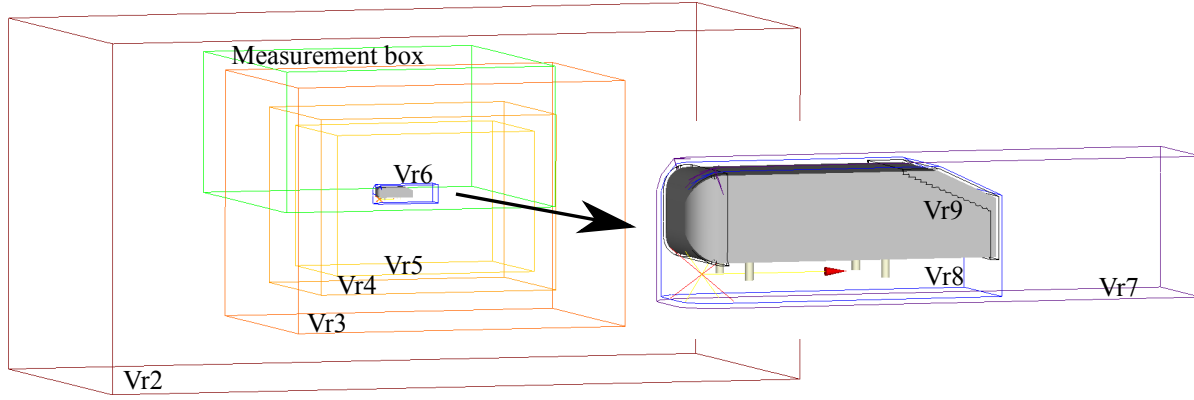


Figure 2.13: Visualization of the box refinement for the numerical simulations.

| Variable | Ahmed Body | Realistic Model |
|-----------------------|-------------------------------|-------------------------------|
| Physical Time Scaling | 1 timestep = $2.715e - 06sec$ | 1 timestep = $9.308e - 06sec$ |
| Minimum Level of VR | VR 9 ($7.50e-04$ m/voxel) | VR 9 ($2.50e-03$ m/voxel) |
| Simulation time | 147333 timesteps (0.400 sec) | 324000 timesteps (3 sec) |
| Reynolds | $2.68456e+06$ | $1.04402e+07$ |

Table 2.2: Power Flow set-up

previously described, the red lines are the numerical results from *PowerFLOW* and the “Lienhart LDV” are issued from Lienhart et al. [107]. Good agreement is found with the Lienhart data from both the numerical and experimental data despite the differences between the numerical and experimental drag and lift coefficients reported in *table 2.3*. The averaged surface pressure reported in *figure 2.15*, shows small differences at the end of the roof between the numerical simulation on the left and the experimental results from Lienhart on the right. The low pressure at the end of the roof seems underestimated by the numerical simulation. At first, this problem was related to a too coarse meshing on the roof because the finest VR (VR9) was set just in the front and the rear part of the model. An expensive simulation was run with the smallest VR all over the roof but not any differences were noticed respect to the cheaper setting used for all the simulations. The work of Regulski et al. [108] proposed a different source for the underestimation of the pressure right after the sharp edge. The “stair-case” form of implementing a geometry in *PowerFLOW*, can result in roughness effects that can impact the numerical results. Moreover, the LBM calculation seems to be locally not adapted to a geometry with a sharp edge, nevertheless is able to recover very fast after the edge to the right value of the speed and the pressure. To investigate deeper the sharp edge sensitivity, a simulation was run with a radius of curvature at the end of the roof of $0.5mm$, considering this small value radius as a sharp edge. Not even this type of correction is able to estimate properly the detached zone after the sharp edge. Even for the experimental results reported in *Chapter 3*, it will be remarked the hard task of capturing the right separation point due sharp edges. Nevertheless, the numerical simulation resulted to have nice agreement with the experimental data issued from the wind tunnel tests for both Ahmed body and the realistic model

regarding streamwise velocity profiles and crossflow S-PIV measurements reported in figures 2.16 and 2.17.

| | Cd | Cl |
|-------------------------|-------|-------|
| Ahmed body Experimental | 0,356 | 0,311 |
| Ahmed body Numerical | 0,345 | 0,334 |

Table 2.3: Aerodynamic coefficients comparison.

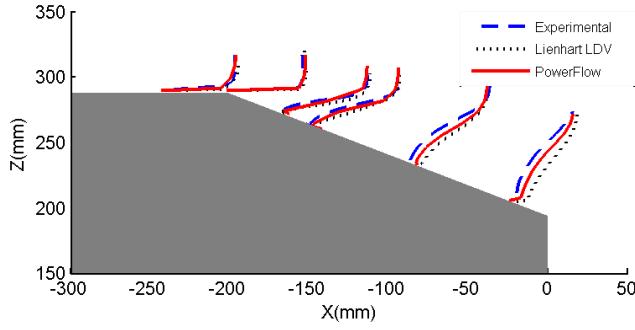


Figure 2.14: Comparison of mean streamwise velocity profiles in the symmetry plane $Y^*=0$

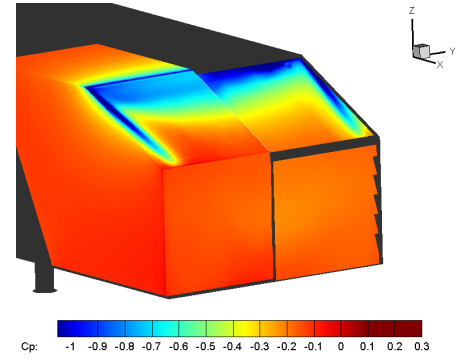


Figure 2.15: Pressure wall measurement: left numerical simulation, right experimental from [107]

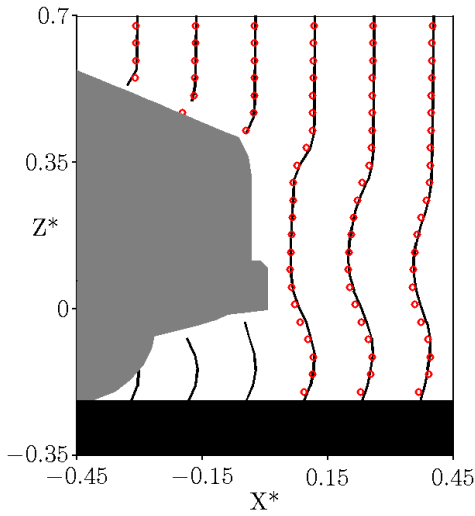


Figure 2.16: Comparison of mean streamwise velocity profiles in the symmetry plane $Y^*=0$.
– Numerical, \circ Experimental

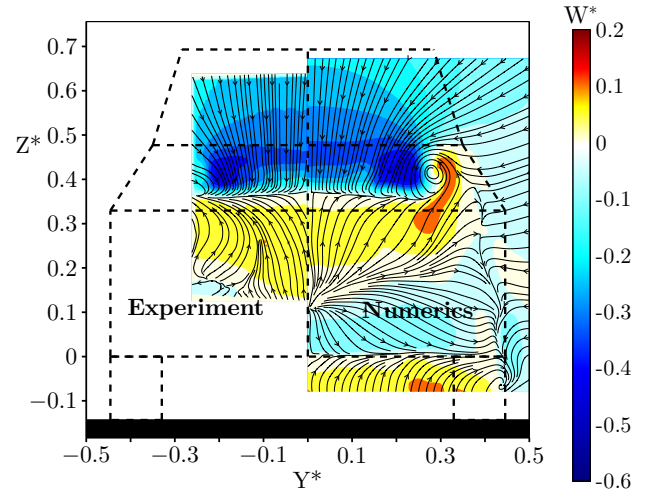


Figure 2.17: Comparison of mean normal velocity W^* . Plane at $X^*=0.02$. The dashed lines represent the geometry of the model. Left: experiments. Right: numerical simulations.

2.3 Analysis methods for vortex identification

Most of the visualization presented in this work are based on averaged velocity and wall pressure measurements. To gain a deeper understanding of the flow organization a geometry criterion was used to overcome the limitation of the criteria based on the velocity gradient tensor as Q-criterion [109], Δ -criterion [110] and λ_2 -criterion [111]. In fact, especially for the counter-rotating structures in the near wake as well the longitudinal overall rotation of the flow field behind the model, the velocity gradient based criteria fail to detect those structures because they are related to low vorticity. It will be use then the Γ vortex identification algorithm that allows the identification of regions of dominant rotation in a flow with an integral and normalized criterion. It was introduced by Graftieaux et al. [112] in order to identify vortices for unsteady turbulent flows.

- **Γ_1 -criterion**

The Γ_1 -criterion is a vortex centre identification algorithm.

Let \mathbb{A} be the global domain (a plane) and $P \in \mathbb{A}$ a fixed point in this domain. $\Gamma_1 \in [-1, 1]$ is a dimensionless scalar at P :

$$\Gamma_1(P) = \frac{1}{S} \iint_{M \in S} \frac{[P\vec{M} \wedge \vec{U}_M] \cdot \vec{e}_z}{\|P\vec{M}\| \cdot \|\vec{U}_M\|} dS = \frac{1}{S} \iint_{M \in S} \sin(\theta_M) dS \quad (2.1)$$

Where S is a two dimensional area surrounding P and M a point in S . The vortex center is then determined when $|\Gamma_1| = 1$

The discrete expression for Γ_1 is :

$$\Gamma_1(P) = \frac{1}{N} \sum_S \frac{[P\vec{M} \wedge \vec{U}_M] \cdot \vec{e}_z}{\|P\vec{M}\| \cdot \|\vec{U}_M\|} = \frac{1}{N} \sum_S \sin(\theta_M) \quad (2.2)$$

Where N is the number of points inside S .

- **Γ_2 -criterion**

The Γ_2 -criterion is a vortex core identification algorithm. It's a similar criterion of Γ_1 on the exception that it takes into account the local convection velocity around P . The Γ_2 criterion, taking into account the average convection velocity in the domain S , is a Galilean invariant Γ_2 is defined by the relation :

$$\Gamma_2(P) = \frac{1}{S} \iint_S \frac{[P\vec{M} \wedge (\vec{U}_M - \vec{U}_P)] \cdot \vec{e}_z}{\|P\vec{M}\| \cdot \|\vec{U}_M - \vec{U}_P\|} dS$$

where $\vec{U}_P = \frac{1}{S} \iint_S \vec{U} dS$

Once again, as the data treated is in a discrete mode, the Γ_2 definition changes into:

$$\Gamma_2(P) = \frac{1}{N} \sum_N \frac{[P\vec{M} \wedge (\vec{U}_M - \vec{U}_P)] \cdot \vec{e}_z}{||P\vec{M}|| \cdot ||\vec{U}_M - \vec{U}_P||} \quad (2.3)$$

$$\text{where} \quad \vec{U}_P = \frac{1}{N} \sum_N \vec{U} \quad (2.4)$$

The vortex bound is then defined for $|\Gamma_2| > \frac{2}{\pi}$

Discussion on the Γ_2 criterion

The integration domain S for the present calculation is square and defined by the number of layers N as illustrated in *figure 2.18*. The choice of the shape of S as well the number of layer N is not trivial. Two articles in the bibliography deals with this subject. Ismail [113] suggested that a judicious choice for the number N of Layers is generally 3 to 5 depending on the nature of the flow. Koched [114] studied the influence of layers and shape of the integration domain (square and circular). It appears that the vortex bound originally determined for a values $\Gamma_2 > \frac{2}{\pi}$ varies slightly with the number of layers. However, a weak value of $\frac{N}{N_x}$ threatens the definition of Γ_2 because of the loss of the local convection velocity information, N_x is the discretization of the domain. It is actually important to choose the parameter N with regard to the discretization of the data. The choice of N in the present calculation of Γ_2 is adjusted observing its influence in the Lamb-Oseen vortex detection. This works was done by A. Nazarians during his first year master internship supervised by the author [115]. The Lamb-Oseen analytic expression of azimuthal velocity and vorticity are :

$$U_\theta(r, t) = \frac{\Gamma}{2\pi r} \left[1 - \exp\left(-\frac{r^2}{a^2}\right) \right] \quad (2.5)$$

$$\Omega(r, t) = \frac{\Gamma}{\pi a^2} \exp\left(-\frac{r^2}{a^2}\right) \quad (2.6)$$

Figure 2.19 reports the characteristic vorticity contour and velocity vectors of the Lamb Oseen vortex. Considering a plane containing $[N_x \cdot N_y]$ points, the calculus of the Γ criteria for different range of $1\% < \frac{N}{N_x} < 8\%$ are reported in *figure 2.20*. The vortex center location seems not dependent on the choice of $\frac{N}{N_x}$ for Γ_1 . On the contrary, small values of $\frac{N}{N_x}$ do not succeed to capture the vortex core. For $\frac{N}{N_x} = 1\%$ at $r/l_0 = 1$, Γ_2 is $0.5 < \Gamma_2 < 0.6$, the correct value should be $\Gamma_2 = 0.63$. For the experimental results presented in *Chapter 3*, the value of N used vary between 2 and 3 due to the high resolution of the spatial discretization.

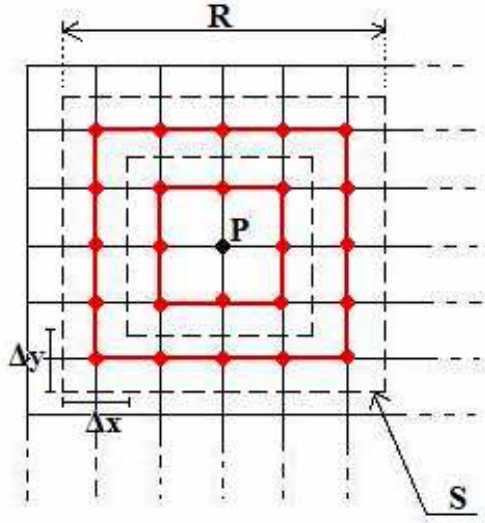


Figure 2.18: Domain of integration [114]

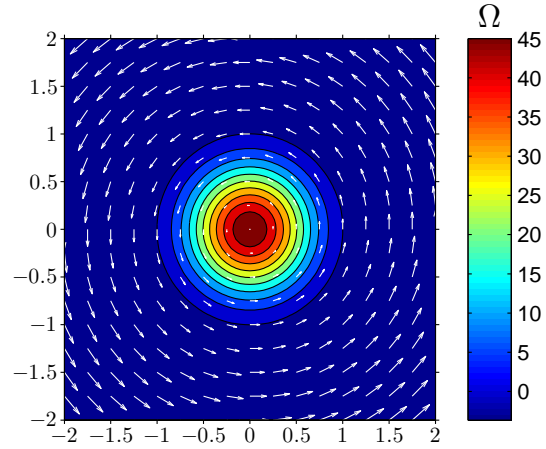
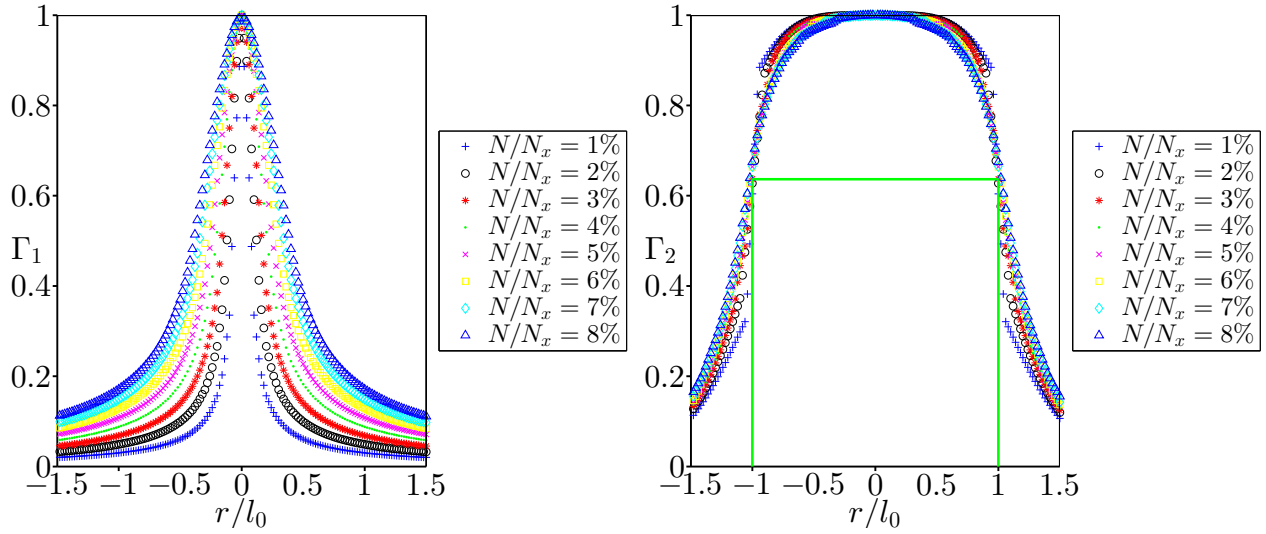


Figure 2.19: Lamb-Oseen vorticity contour and velocity vectors


 Figure 2.20: Evolution of Gamma criteria over number of layers for the Lamb-Oseen vortex. The green lines represent the value of $\Gamma_2 = \frac{2}{\pi}$

2.4 Discussion about the wind tunnel tests

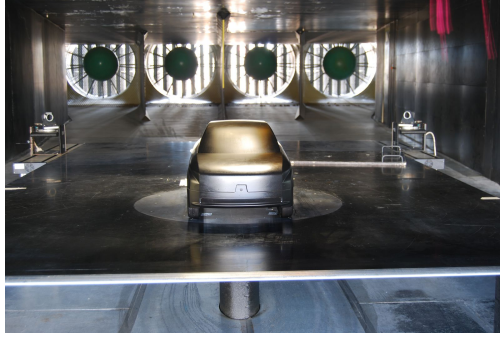
The positive and negative characteristics of the wind tunnel have to be acknowledged, especially in what concerns the approximations made with respect to the realistic environment in which vehicles are used. The physical restrictions for the use of ground-simulation techniques in automotive wind tunnels are elucidated in the works of [116] and [24]. In what follows it is proposed a discussion of such limitations.

- Road representation and moving floor

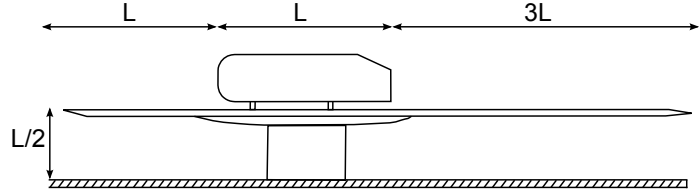
The model is placed on a false floor which is a fix elevated surface approximately half model length high (*figure 2.21*). The false floor leading edge is situated approximately 1 body length in front of the model and the trailing edge is 3 length behind the model [97]. The leading edge is a NACA 0015 to ensure a the boundary layer eight of $24 \pm 3\text{mm}$ at 40m/s at $3/2L$ from the leading edge. The shape factor of the boundary layer H is $1.18 < H < 1.67$ at 40m/s [117]. Those values are typical of a turbulent boundary layer.

Therefore, over the false floor a turbulent boundary layer develops and it is thicker than the unsteady boundary layer generated at the road under a moving car [116]. In road vehicles aerodynamic tests, a way to avoid errors in drag and lift measurements compared to real road conditions, is to simulate the relative motion between road and vehicle by means of a moving belt or boundary layer control. Unfortunately, the present wind tunnel is not equipped with moving floor nor with boundary layer control. In order to anticipate the implication of this fixed floor, it is briefly outline some bibliographic results. Krajnović et al. [118] estimated that floor motion reduces the Ahmed body drag and lift by 8% and 16% with respect to the use of a fixed floor. In their LES numerical simulations, the overall wake flow organization resulted to be quite insensitive to the floor movement even thought important modifications are found close to the floor and on the slanted surfaces. The numerical discrepancy in drag and lift measurements reported by Krajnović et al. between moving and fix floor are actually the same order of magnitude of the experimental ones reported by Cooper over different vehicles geometries [119]. Regarding the Ahmed body rear end, as reported by Strachan et al. [120], the moving ground should have indeed little influence on the formation of longitudinal vortices over the rear slant. The errors induced by the fixed floor are then undoubtedly, nevertheless the idea of all the tests is to study the comparison between models that featured different upper rear side edges. It is supposed that, if an error is induced with respect to the real road flow, it should be constant for all the models. Actually, Howell et al. [121], reported that the trends of drag and lift characteristic of the MIRA model due to geometry modifications were similar for both moving and stationary belt.

Numerical simulations were performed with *PowerFLOW* to test the moving floor influence on drag and lift of the realistic model presented in *Chapter 4*. The drag differences between the most rounded side edges model and the sharp one are -2.3% and -1.5% with fix and moving floor respectively. In fact, the drag experiences approximately 8% reduction for both models when the moving floor is computed with respect to fix floor conditions. Unfortunately, lift differences are



(a) Model location over the elevated surface



(b) Dimensions in body length of the false floor

Figure 2.21: Wind tunnel false floor details.

more important. The moving floor resulted in 55% lift reduction for the sharp side edges model and in 85% lift reduction for the rounded edges model with respect to the fix floor. The lift differences between the two models were then 37% with the fixed floor and 80% with the moving floor. It means that the rounded edges model results are more sensitive to the moving floor condition and that, unfortunately, the lift trend of the fixed floor are not respected once the moving floor is simulated. It is important also to mention that the lift discrepancy will be much more important at low ground clearance with an underbody incorporating a rear diffuser [122], as in the case of the realistic model analyzed in *Chapter 4*.

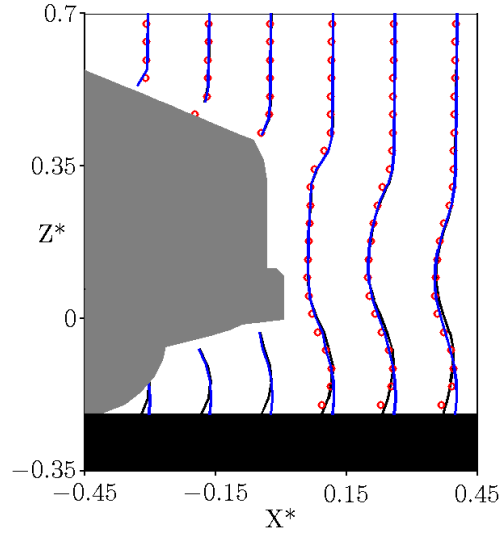


Figure 2.22: Comparaision between numerical and experimental mean streamwise velocity profiles for the realistic sharp rear side pillars model. \circ Experimental, — Numerical fix floor, — Numerical moving floor

- Reynolds similitude

Another element to be clarified in the experimental set-up presentation concerns the model scaling. Since the model tested are $1/4$ of the size of a real vehicle and the free stream velocity U_0 was set at

40m/s for all tests, the question of the “Reynolds similitude” rises automatically. In fact, two flows are kinematically similar if their Reynolds number is the same [16]. First at all, the maximum wind speed was limited by the engines power at 53m/s. Moreover, even if it will possible to increase the speed, it is not recommend because road vehicles are very sensitive to compressibility effects ($M=0.2$) [123]. An earlier boundary layer transition, that could represent an higher Reynolds number, can be “forced” with the use of a strip of sandpaper or increasing the turbulent level of the incoming flow. None of these solutions were applied in the present wind tunnel tests. However, turbulent separation at the vehicle forebody is dependent on the Reynolds number and it might be expected that the quantitative effects of rear edge rounding are dependent on this parameter. Especially for the Ahmed body, the forebody edge separation is very sensitive to Reynolds number as reported by Spohn et al. [69]. In fact, at the leading edge, the flow experiences separation due to the small radius between the forebody and the roof. Normally, the separation is not Reynolds number dependent for sharp edges but the reattachment point is Reynolds number dependent [124]. It is assumed then that for the Ahmed body both separation at the forebody and the reattachment point are Reynolds number dependent. The effect of front edge rounding in vehicles aerodynamic was studied in 1985 by Cooper over different truck models [125]. Leading edge flow separation followed by flow reattachment was observed at subcritical Reynolds number for different forebody radii of the truck. The resulting separation bubble was usually smaller in size at larger radii, for a given Reynolds number. It is interesting to note that, the front radii having equal asymptotic drag coefficient at high Reynolds number, all had fully attached leading edge flow [125]. The influence of the front radius on the structure of the recirculation bubble was reported also in the water tunnel visualization performed by Courtine et al. [126]. They confirmed the strong influence of curvature on the front bubble structure and in addition they highlighted the influence of the bubble aspect ratio on its breaking dynamics.

It is undoubtedly then that the forebody separation of the Ahmed body is Reynolds number dependent. Of course, since the Reynolds number changes the properties of the leading edge separation and then the boundary layer over the roof, it could be suggested that also the effects of the rear geometry rounding will be sensitive to the Reynolds number. To better analyze the experimental Reynolds number sensitivity of the Ahmed body afterbody rounding, preliminary wind tunnel tests are showed in *figure 2.23* for different afterbody rounding. *Reference* stands for the reference Ahmed body with sharp edges, *Roofradius* for the model with 10% roof radius and *Roof-sideRadius* for the model with both side and roof radii of 10%. For low Reynolds numbers - below around $Re=1.5 \cdot 10^6$ corresponding to $Uo = 20m/s$ - the effect of the Reynolds number on drag is important due to the high rate of variation among the different Reynolds numbers. However, whatever the Reynolds number, the hierarchy of C_d and C_l among the different cases is the same. Moreover, for $Re > 1.5 \cdot 10^6$, the drag behavior is weakly dependent on the Reynolds number. The constancy of C_d after a certain “critical “ Reynolds number was observed as well by [127] in the same wind tunnel. Regarding the constancy of drag, an interesting example of vehicle that has not and asymptotic value of drag for different Reynolds numbers is the Audi A2 in both scaled and full scale tests [123].

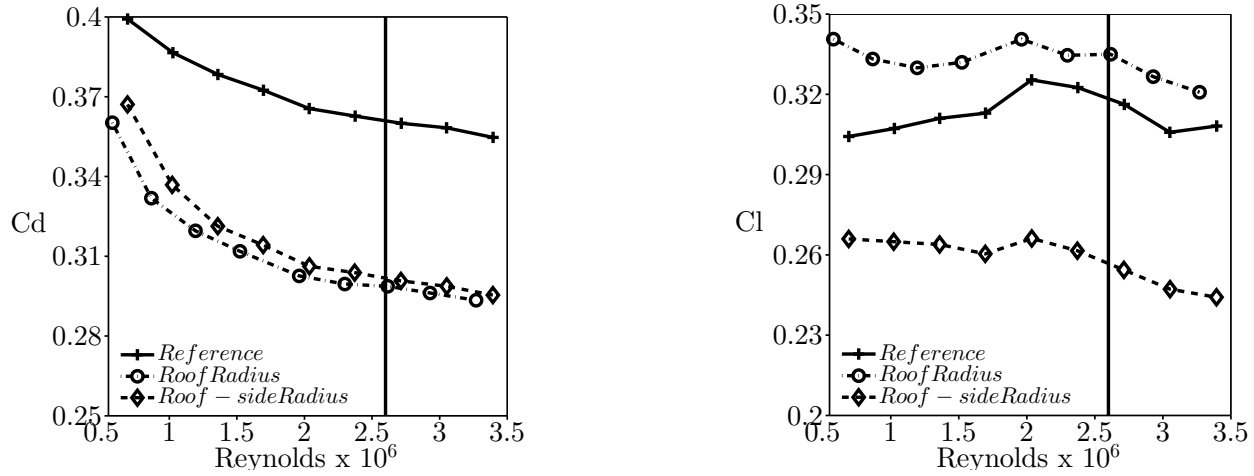


Figure 2.23: Reynolds dependence of the aerodynamics forces. The solid vertical line represents the experimental Reynolds number, $Re = 2.7 \times 10^6$. Left: drag coefficient. Right: lift coefficient.

- Forebody shape influence

This last item is not directly related to the wind tunnel limitation but it is an interesting point to analyze. A numerical preliminary simulations were performed to explore how the afterbody rounding effects could be sensitive or not to the forebody geometry. The forebody of the Ahmed body was modified with a slant surface at the forebody (figures 2.24(b) and 2.24(d)). This modification strongly changed the flow field at the forebody with the consequent modification of the flow property over the roof due also to the presence of the A-pillar vortices. Adding a roof radius of 80mm to the reference Ahmed body resulted in a 11% of drag reduction and 2% lift increase. Adding the same roof radius to the modified forebody Ahmed body, resulted in a 8% of drag reduction and 1% lift increase. This “rough test” showed that similar order of magnitude are achieved despite important forebody modifications.

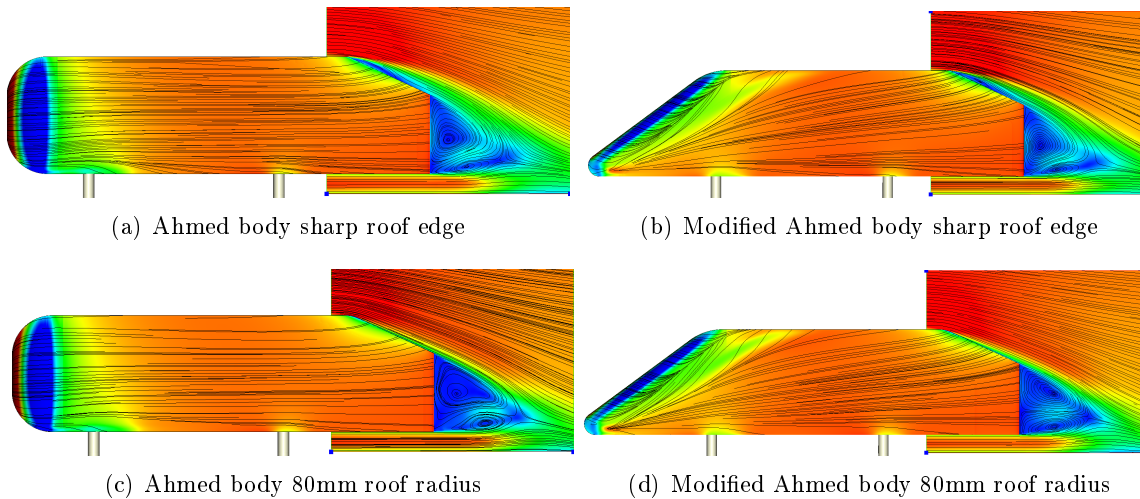


Figure 2.24: Influence of forebody shape on the effects of roof edge rounding

Chapter 3

Effects of edges rounding on the Ahmed Body

Contents

| | | |
|------------|--|-----------|
| 3.1 | Global analysis of the aerodynamic forces | 34 |
| 3.1.1 | Aerodynamic coefficients | 34 |
| 3.1.2 | Interpretation of static wall pressure distribution and velocity fields in the plane of symmetry | 38 |
| 3.2 | 3D effects of pillar rounding on the near wake development | 48 |
| 3.2.1 | Oil flow visualizations | 48 |
| 3.2.2 | Cross-flow analysis | 49 |
| 3.2.3 | Schematic representation of the wake | 59 |
| 3.3 | Towards a realistic model | 61 |

This chapter aims to explore the influence of afterbody rounding over the Ahmed body featuring 25 degree rear slant. Experimental analyzes as well as numerical simulations were performed to understand the forces evolution and the flow field modifications resulting from afterbody rounding on the Ahmed body. Curvature effects were investigated experimentally using balance measurements, oil visualizations, wall pressure, and particle image velocimetry measurements. The rear end of the original well-known Ahmed body has sharp connections between the roof and the rear window as well as squared rear pillars. In addition to the reference case, six modified rear ends were tested to study the drag and lift evolution due to side and roof pillar rounding. The tridimensional organization and vorticity transport in the near wake were analyzed and connected to the aerodynamic characteristic modifications of the Ahmed body.

Most of the results of the second part of the chapter were published in Rossitto et al. [128].

3.1 Global analysis of the aerodynamic forces

3.1.1 Aerodynamic coefficients

The effect of afterbody rounding are hereunder analyzed by means of drag and lift coefficients variations. For each set of edges rounding, i.e. R_{er} , R_{es} and R_{ers} , the comparison with the numerical simulations is presented in order to justify the choice of the selected experimental radii. Table 3.1 reports the experimental aerodynamic coefficients for all models as well as their percentage variation with respect to the reference case.

| | Cd | Cl | ΔC_d | ΔC_l |
|-----------------|-------|-------|--------------|--------------|
| $R_0 S_0$ | 0,356 | 0,311 | - | - |
| $R_5 S_0$ | 0,298 | 0,333 | -16% | +7% |
| $R_{10} S_0$ | 0,297 | 0,333 | -16% | +7% |
| $R_{40} S_0$ | 0,297 | 0,331 | -16% | +6% |
| $R_0 S_5$ | 0,358 | 0,264 | +1% | -15% |
| $R_0 S_{10}$ | 0,359 | 0,241 | +1% | -22% |
| $R_{10} S_{10}$ | 0,298 | 0,254 | -16% | -18% |

Table 3.1: Aerodynamic coefficients and their variation with respect to the reference case $R_0 S_0$.

Reference case ($R_0 S_0$)

The present experimental drag coefficient is higher than the one presented by Ahmed et al. [26]. As a matter of fact, the experimental set-up of Ahmed et al. was slightly different from the one used in this work. The Ahmed et al. wind tunnel test was set to 60m/s, i.e. Reynolds= $4.29 \cdot 10^6$, and the test section was open. It resulted in $C_d = 0.285$. Among the various source of drag discrepancy between different works, the differences in blockage ratio can generate important increase of drag as reported by [129]. Recently, Keogh et al. related the high scattering of Ahmed body drag values to the different blockage ratios of the various wind tunnel used in literature [130]. Different blockage ratios could not justify all the differences among the values reported in the literature. Small differences in the bubble lengths over the rear slant could also explain deviations on the drag coefficient between similar studies. In fact, the recirculation bubble length over the rear window appears to be very sensitive to the quality of the upper sharp edge [58]. The models used here were made in wood or produced by milling machine. For both processes, sharp edges show always a small radius. For instance a high quality milling machines produces 0.5mm radius when a sharp edge is required. To reduce this problem, a tiny nylon wire was carefully installed at the end of the roof to improve the quality of the sharp edge.

Figure 3.1 reports the isocontour of the zero streamwise velocity extracted from PIV measurements and numerical simulations in the symmetry plane of $R_0 S_0$. Without the improved edge, no recirculation bubble is shown over the rear slant in the experimental results, i.e the flow is attached. On the contrary, the tiny wire succeeds to force flow separation at the end of the roof, thereby forming a separated bubble along the slanted surface. The length of the experimental recirculation bubble

was found here to cover 75% of the rear window, which is consistent with available literature [58]. Roof edge improvement was performed over the three experimental models featuring sharp edges at the roof end (R_0S_0 , R_0S_5 and R_0S_{10}). Numerical contours of zero streamwise velocity are reported as well to show the comparison with the experimental data. It is noticeable that the numerical separation bubble over the slanted surface is smaller than the experimental improved edge. The numerical comparison between experimental and numerical results for R_0S_0 is reported in *figure 3.2*. It is found that the experimental drag and lift coefficients are respectively +3% and -7% with respect to the numerical simulations.

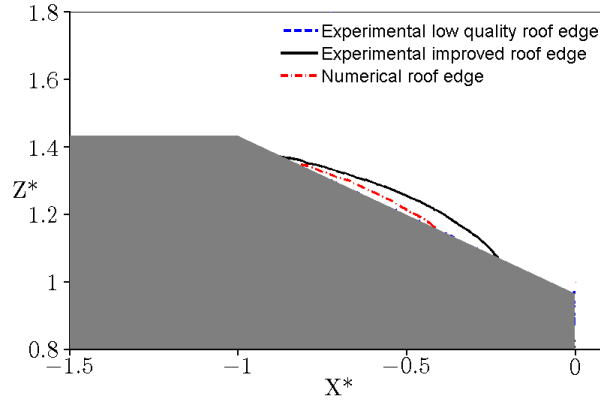


Figure 3.1: Sharp roof edge improvement comparison. The contour lines represent the zero streamwise velocity

Roof edge rounding ($R_{10}S_0$ and $R_{40}S_0$)

The comparison between the numerical and the experimental results for different roof radii configurations is presented in *figure 3.2*. Focusing on the small roof radii, R_5S_0 drag is not in a agreement with the numerical results. In fact, the experimental set up promotes an early suppression of the separated bubble over the rear slant, resulting in a important drag reduction. The numerical simulations, on the contrary, seem to capture a progressive influence of small radius at the roof end on the behavior of the separation bubble and thus on the drag. In fact, for such small values of roof radius, the numerical simulation still presents a tiny recirculation over the rear slant. It is actually important to notice how the flow sensitivity to the quality of the roof radius analyzed previously for the reference case is quite important also for R_5S_0 that presents different flow behavior for numerical and experimental test.

Good drag and lift agreement is then achieved for roof radius greater than 5% ($R_{>5}S_0$), when the flow is fully attached over the slanted surface for both numerical simulations and experiments. The idea behind the first two selected *Rer* (R_5S_0 and $R_{10}S_0$) for the experimental tests, was to analyze the influence of small rounding at the roof end and thus to study the evolution from separation bubble towards a complete attached flow over the window. The third *Rer* model, $R_{40}S_0$, was chosen to establish a comparison with the work of Thacker et al. [50].

Analyzing the experimental results of the *Rer* models, it can be noticed that lift is increased com-

pared to R_0S_0 . This effect is associated to the flow acceleration over the rounded edge and is constant for the three model tested. When comparing R_5S_0 with R_0S_0 , 16% drag reduction is observed. This reduction can be directly related to the elimination of the separation over the rear slant and the lengthening of the near wake. Hence, R_5S_0 drag and lift are similar to $R_{10}S_0$, as well as the flow topology. This is the reason why, in what follows, the R_5S_0 rear end will not be further analyzed. Further roof radius increase seems not to affect drag nor lift. Thacker et al., with 40% roof curvature radius, measured a comparable reduction, i.e a 10% drag reduction [50].

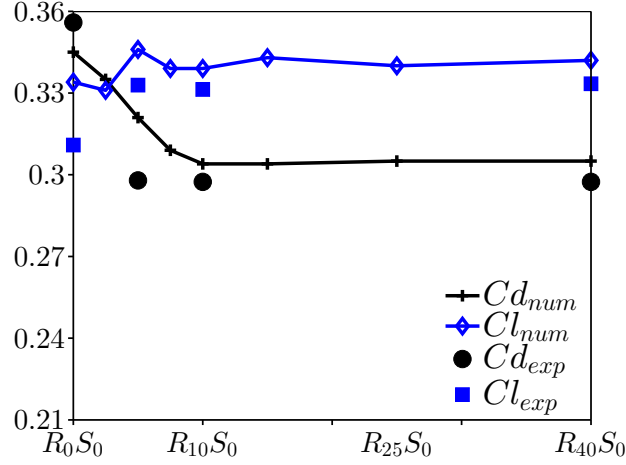


Figure 3.2: Drag and lift coefficients. Comparison between numerical and experimental results for different roof radii configurations (all configurations have sharp pillars)

Side edge rounding (R_0S_5 and R_0S_{10})

Figure 3.3 reports the drag and lift coefficients related to the *Res* models. The experimental side radii were chosen to estimate the impact of side rounding on the development of the side pillar vortices. Due to the technical limitations mentioned in Chapter 2, the side radii chosen for the experiments were 5% and 10%, even though numerical simulations were performed up to 20%. The experimental maximum drag and lift deviation from the numeric results are respectively +1% and -5%. Rounding the side pillars has a negligible effect on the total drag. On the contrary, strong lift reductions are measured. Increasing the side radius, from R_0S_5 to R_0S_{10} , results in a further lift reduction compared to the reference case. It can be reminded at this point that, in automotive aerodynamics, lift reduction is a positive effect in terms of stability and braking distance [23].

For R_0S_{10} , no drag modifications are noticed when compared with R_0S_0 . It will be explained in what follows that this zero net balance results from opposite effects related to the slanted surface and the rear base. In the past literature, as in the work of Gilhaus et al. [48], side pillars rounding were stated as a geometry modifications that generate global drag reduction on a 3/8 scaled European compact size vehicle. 10% of side pillar radius resulted in 5% drag reduction compared to the sharp edge rear end. Drag reductions associated with side rounding were reported also during the development of the Audi 100 III [47]. The minimal impact in drag of the Ahmed body side rounding,

highlights that the balance between local opposite effects depends on the ratio of the rear surfaces, i.e. slanted surfaces and base [131].

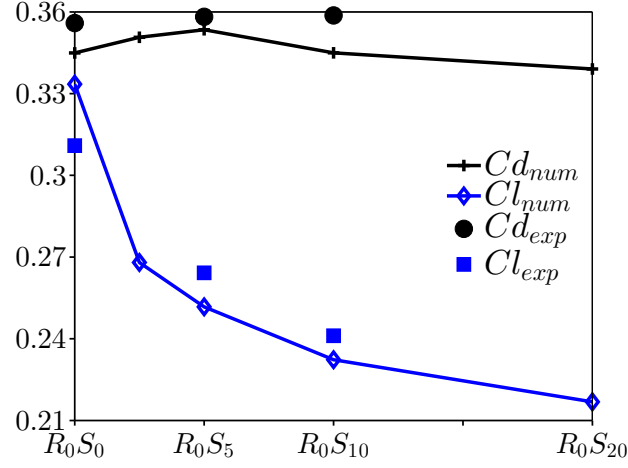


Figure 3.3: Drag and lift coefficients. Comparison between numerical and experimental results for different side radii configurations (all configurations have sharp roof edge)

Roof and side edges rounding ($R_{10}S_{10}$)

A good agreement between numerical simulation and experimental results is found also for the double rounding configuration $R_{10}S_{10}$ as reported in figure 3.4. Surprisingly, the rear end with both roof and side rounded edges, $R_{10}S_{10}$, shows the same drag coefficient as $R_{10}S_0$. The lift value, on the contrary, experiences reduction similar to side rounding as R_0S_{10} .

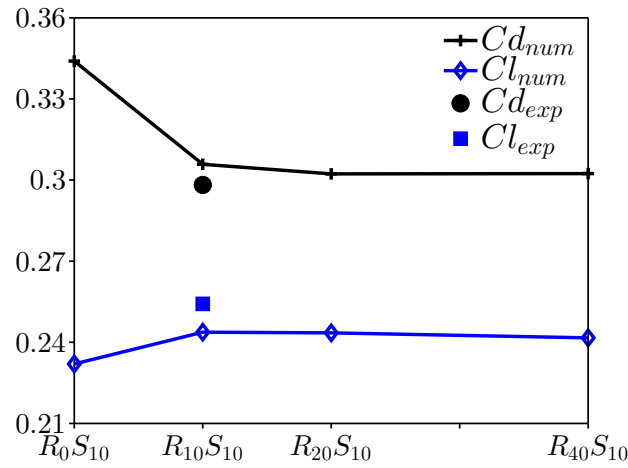


Figure 3.4: Drag and lift coefficients. Comparison between numerical and experimental result for $R_{10}S_{10}$. The plot reports also the different numerical roof radii configurations results (all configurations have 10% side pillars radius)

After this overview of the influence of afterbody rounding on drag and lift, the wall pressure measurements and the flow field in the symmetry plane will be presented. Subsequently, additional experimental results as oil flow visualizations and S-PIV cross flow acquisitions will be reported to analyze in detail the effects of side rounding. The analysis will be done comparing $R_{10}S_0$ with $R_{10}S_{10}$.

3.1.2 Interpretation of static wall pressure distribution and velocity fields in the plane of symmetry

Reference case (R_0S_0)

For the reference configuration R_0S_0 , Ahmed et al. [26] identified three main sources of pressure drag generated along the slanted surface and in the near wake of the body. Due to the sharp edge between the roof and the backlight, the flow experiences separation-reattachment, thereby forming a separated bubble along the slanted surface. The low pressure area due to the separation bubble is visible in *figure 3.5* in the upper part of the rear slant.

The second drag source is associated with the highly energetic longitudinal vortices, the so-called C-pillar vortices, developing along the rear side pillars. These vortices are generated by the pressure gradient between the side of the model and the rear slant. It will be shown in what follows that, despite similar pressure gradient, different edge radii can change the characteristics of the origin of such vortices. The presence of these longitudinal vortices leads to a strong localized low pressure on the side of the rear slant.

The third major source of drag is associated with the separated region in the near wake, leading to the low pressure distribution along the vertical base.

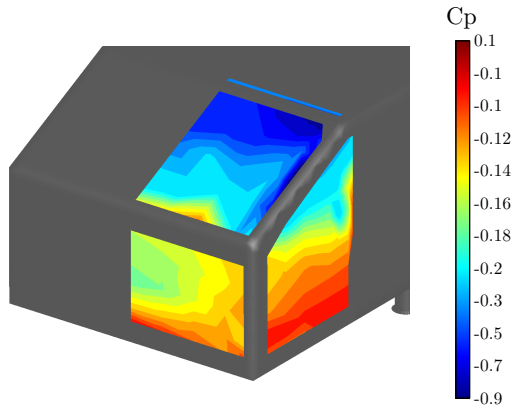


Figure 3.5: R_0S_0 , wall pressure coefficient C_p

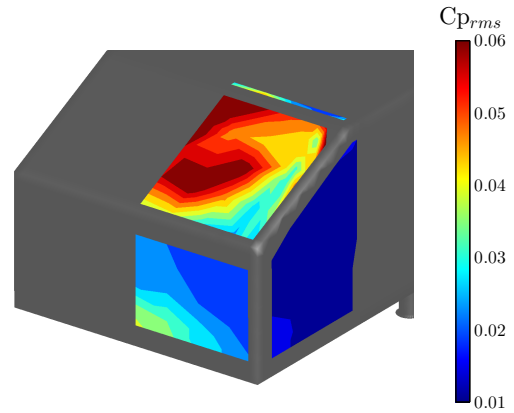


Figure 3.6: R_0S_0 , wall pressure coefficient root mean square $C_{p_{rms}}$

The root means square pressure coefficient ($C_{p_{rms}}$) is reported in *figure 3.6*. It is interesting to notice that the high levels of pressure fluctuations are localized over the rear slant. Hinterberger et al. [132] analyzed the unsteadiness of the flow over the rear end. The authors showed that unsteady activities are associated with the recirculating zone over the window that can be alternatively

separated or fully attached. The PIV measurements in the symmetry plane are reported to analyze the mean characteristic of the near wake organization. The previously mentioned separation bubble is easily identified by the negative streamwise velocity over the slanted surface (*figure 3.7*). The separation region is composed by two counter-rotating structures confined inside the upper and lower shear layer. The upper structure is more extended than the lower one. An attempt to quantify the energy of the rotating structure was performed in the work of Nazarians [115]. Using the Γ_2 criterion to define the limit of the rotating upper and lower structure, it resulted that the upper structure averaged spanwise vorticity was twice than the lower one. Venning et al. estimated that the circulation in the upper structure has 45% as much circulation as the slant recirculation and the lower structure only 30% [133]. It is useful to define here a variable L^* as the length of the mean recirculation region identified by the saddle point in the streamlines of the near wake. Precisely, $L^*=0.89$ for R_0S_0 . L^* will be used afterward as a characteristic length for the cross-flow analysis. Maximum level of turbulent kinetic energy are localized close to the separation at the end of the roof underlining the separating shear layer. The interaction between the high speed underbody flow and the near wake results as well in elevated levels of kinetic energy as shown in *figure 3.8*.

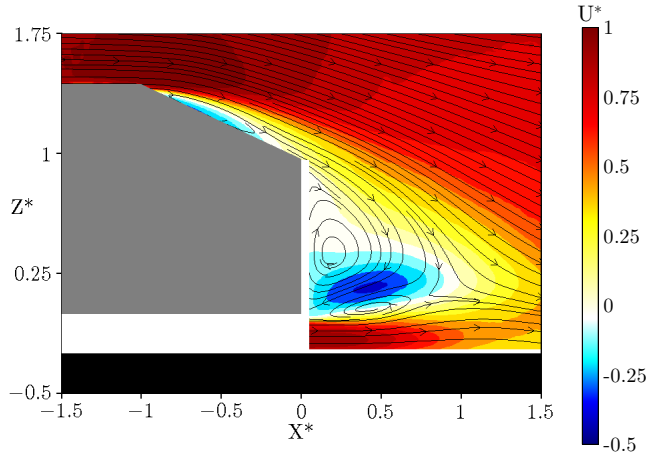


Figure 3.7: R_0S_0 , time averaged streamlines and mean streamwise Velocity U^* at $Y^*=0$

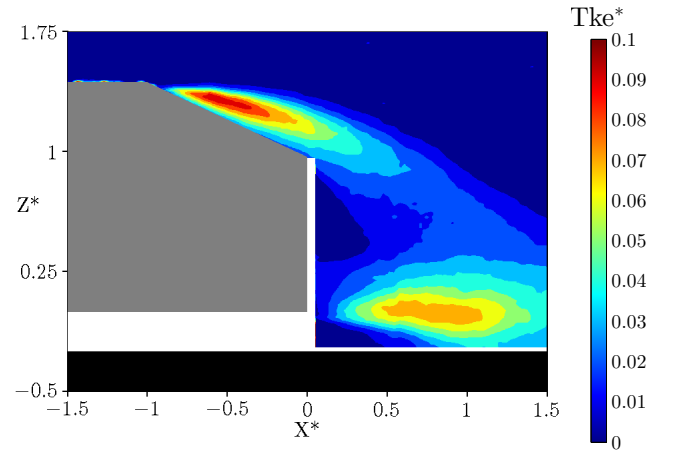
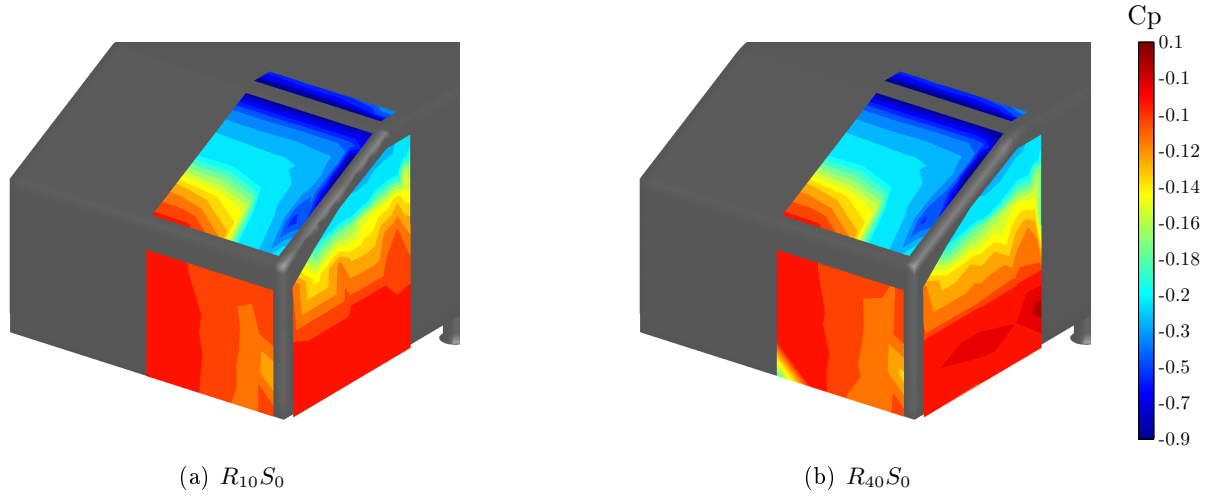
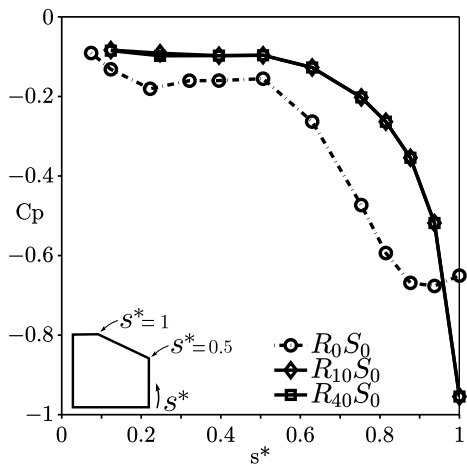
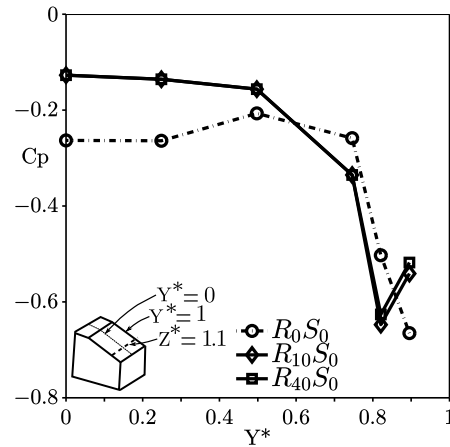


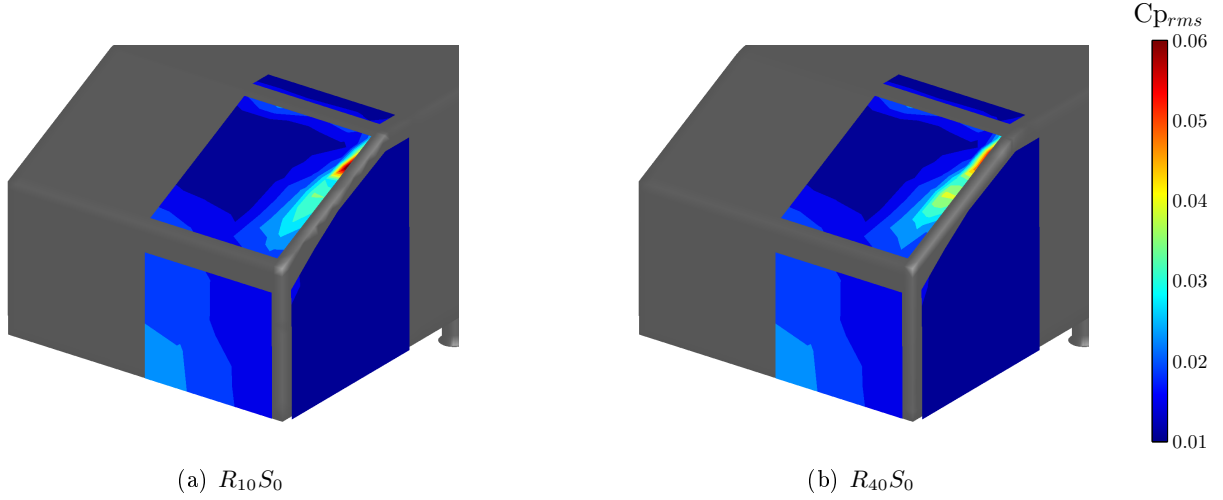
Figure 3.8: R_0S_0 , turbulent kinetic energy Tke^* at $Y^*=0$

Roof edge rounding ($R_{10}S_0$ and $R_{40}S_0$)

When rounding the upper edge of the slanted surface, noticeable changes are observed in the flow field. No separation occurs at the junction between the roof and the rear slant for $R_{10}S_0$. A low-pressure area around the rounded edge is generated due to the flow acceleration, followed by a pressure recovery over the rear slant (*figure 3.9(a)*). A similar behavior is found with $R_{40}S_0$, despite the roof radius is four times bigger (*figure 3.9(b)*). The flow remains fully attached until it separates at the end of the rear window. *Figure 3.10* shows the evolution of C_p along the symmetry plane for the models more quantitatively. At the first probe along the slanted surface, $s^*=1$, the low C_p due to the acceleration over the rounded edge on the roof is remarked. For the reference case, the

sharp edge at the end of the roof generates a separation region, constant C_p until $s^*=0.85$. On the contrary, the pressure coefficient of the models with a rounded roof edge exhibits a pressure recovery all over the rear window. Over the vertical base, the pressure coefficient for both rounded models is higher than the reference case. On the side of both models, the C-pillar vortex is similar to R_0S_0 , as illustrated in *figures 3.9(a) and 3.9(b)* by the concentrated low-pressure footprint. *Figure 3.11* reports the spanwise evolution of C_p for $Z^* = 1.1$, (this location corresponds to $s^*=0.6$ in *figure 3.10*). Both rounded models present a higher C_p value across the backlight due to the pressure recovery previously mentioned. The flow over the rear windows is now fully attached for both models resulting then in weak pressure fluctuations over the rear window. Fluctuations are now present only on the side of the rear window model due to the C-pillar vortex (*figures 3.12(a) and 3.12(b)*).

Figure 3.9: Wall pressure coefficient C_p Figure 3.10: Pressure distribution in the symmetry plane ($Y^* = 0$) for all modelsFigure 3.11: Pressure distribution at constant $Z^* = 1.1$ for all models

Figure 3.12: Wall pressure coefficient root mean square $C_{p_{rms}}$

To help interpreting the origin of lift and drag alteration for the rounded Ahmed bodies, the static pressure coefficient has been integrated separately over the slanted surface and the vertical base. Table 3.2 reports the percentage change in the pressure coefficient for the $R_{10}S_0$ and $R_{40}S_0$ models compared to R_0S_0 . Although the lack of pressure probes along the rounded pillars makes these results an estimation, it appears clearly that the downstream motion of the wake structures, analyzed in details in what follows, leads to an increase in base pressure of up to 28% for the $R_{40}S_0$ configuration. The elimination of the bubble over the rear slant results in a local pressure increase of 11%. Figure 3.13 reports the percentage contribution to the total drag of the rear slant and the vertical base from the numerical simulations. Increasing the roof radius reduces the rear slant and base contributions.

| | Rear window ΔC_p | Vertical surface ΔC_p |
|-------------|--------------------------|-------------------------------|
| R_0S_0 | - | - |
| $R_{10}S_0$ | +11% | +28% |
| $R_{40}S_0$ | +9% | +20% |

Table 3.2: Variation in spatially averaged mean C_p over the rear window and vertical surface relative to the reference case R_0S_0 .

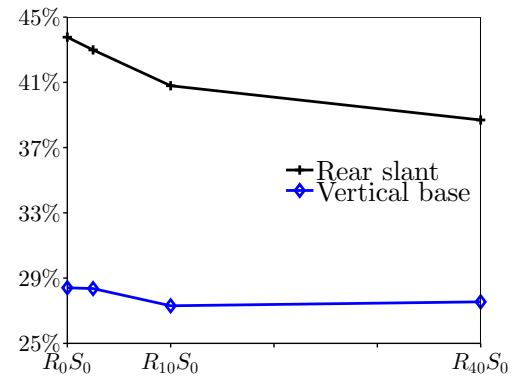


Figure 3.13: Influence of roof edge rounding on the contributions to total drag of rear slant and base, from numerical simulations

The time-averaged streamlines in the plane of symmetry of the near wake, reported in figures 3.14(a) and 3.14(b), show that no separation occurs at the end of the roof and that the two counter-rotating

structures are more symmetrical than R_0S_0 wake flow. Moreover, these structures, related to low static pressure, are shifted further downstream, thus increasing the mean recirculation length for both $R_{10}S_0$ and $R_{40}S_0$ by 12 % ($L^* = 1$) compared to R_0S_0 . In term of spanwise vorticity Ω_Y , the upper structure is 20% weaker than R_0S_0 for both $R_{10}S_0$ and $R_{40}S_0$ [115]. It means that, not only the upper structure is shifted farther, but since its intensity is reduced, the pressure inside is increased resulting in a double positive effects for base drag reduction. Regarding the turbulent kinetic energy, important changes are noticed when comparing with the reference case R_0S_0 . Since the flow overcomes smoothly the roof rounded edge, the turbulent kinetic energy in this area is close to zero, in contrast with the high level for the R_0S_0 model, due to the imposed separation at the roof sharp edge (*figures 3.15(a) and 3.15(b)*). Maximum levels of turbulent kinetic energy are localized downstream the vertical base around the closure of the separated zone.

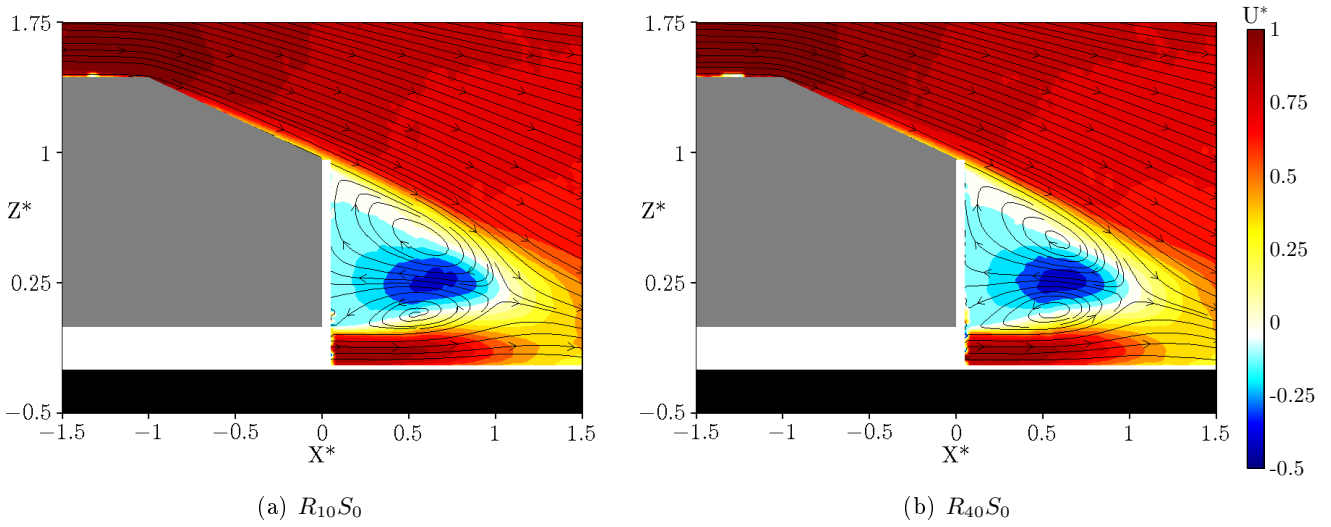


Figure 3.14: Time averaged streamlines and mean streamwise Velocity U^* at $Y^*=0$

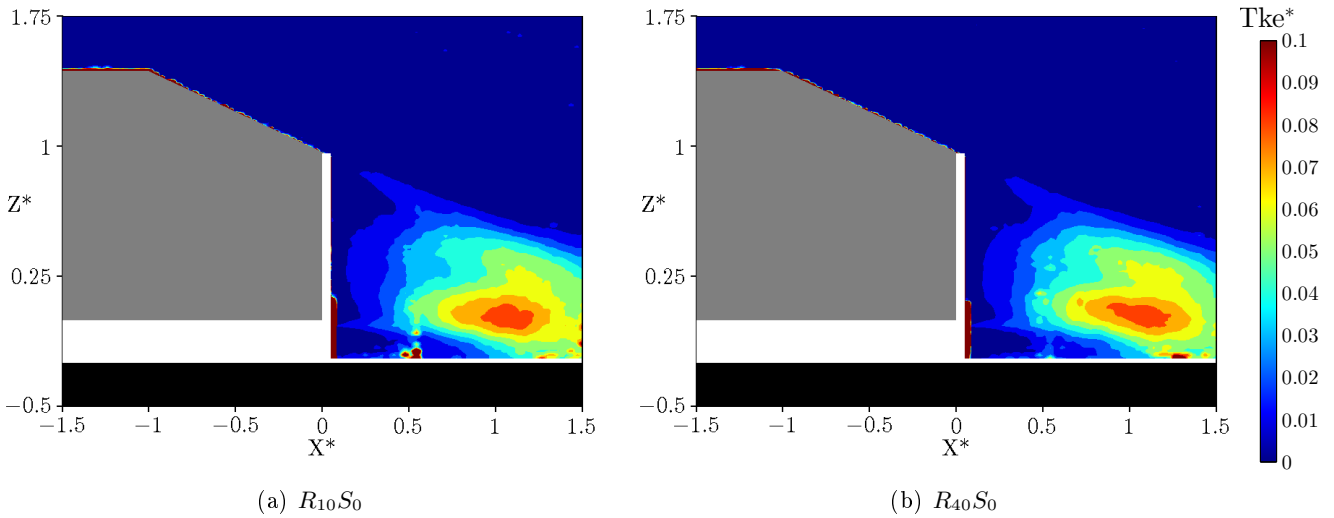


Figure 3.15: Turbulent kinetic energy Tke^* at $Y^*=0$

Side edge rounding (R_0S_5 and R_0S_{10})

The rear ends presented here have a constant sharp edge at the end of the roof to fix the flow separation as in the reference case R_0S_0 . The side edges, on the contrary, are rounded progressively. Starting the analysis from the wall pressure measurements in *figures 3.16(a) and 3.16(b)*, it can be noticed that the pressure foot-print on the side of the models associated to the C-pillar vortex is reduced compared to R_0S_0 , resulting in a local pressure recovery. A constant C_p area is remarked as well over the slanted surface and it is associated to flow separation as in the reference case even though its extension seems higher as well as the pressure. On the contrary, regarding the vertical base, the C_p is reduced generating thus a local drag increase with respect to the reference case. *Table 3.3* reports the percentage variation of the averaged mean C_p for R_0S_5 and R_0S_{10} compared R_0S_0 . It is confirmed that the rear slant experiences a pressure recovery while the base averaged pressure is reduced. As mentioned in the overall analysis of drag and lift, side rounding does not affect the total drag. Nevertheless wall pressure visualization underlines the two opposite effects acting over the rear ends. Analyzing the numerical local drag reported in *figure 3.18*, it can be noticed that, once the side radius is increased, drag is “redistributed” from the rear slant to the base, resulting in no total drag modifications. It is interesting to notice that the tendency of the plot is to invert the major drag contribution from the rear slant to the vertical base. It is suggested that important side rounding drastically reduces the contribution of the rear slant while increasing the base drag (*table 3.3*). *Figure 3.19* shows the pressure recovery over the rear slant and the reduction of the vertical base pressure for both side rounded models with respect to the reference case. The pressure distributions at constant $Z^*=1.1$ are quite similar to the reference case apart for the intensity reduction of the side pillar low pressure for R_0S_{10} (*figure 3.20*).

Wall pressure fluctuations, reported in *figures 3.17(a) and 3.17(b)*, display high levels of fluctuations over the slanted surface centerline. Increasing the side radius from 5% to 10% results in an increase of $C_{p_{rms}}$ levels. The increase of $C_{p_{rms}}$ can be directly related to the reduction of the intensity of the C-pillar vortices and the consequent size increase of the recirculation bubble over the rear slant. Indeed, the induced velocity of the C-pillar vortices tends to force the recirculation bubble reattachment. The relation between the side rounding and the size of the recirculation bubble is analyzed in what follows. At first it has to be reminded that side rounding delays the origin of the side vortex towards the rear slant end. In automotive applications, C-pillar vortices have been determinant in flow development over and downstream the rear slant surface. Beaudoin et al. [78], with the use of side flaps over the 25° Ahmed body, showed massive flow separation at the roof end when eliminating side vortices. In this work, it is confirmed that longitudinal vortices interact with the flow away from the edges all over the window and increase the tendency for reattachment in the central portion of it [134]. So C-pillar vortices have a downwash effect that forces the flow to reattach on the rear window. This is the reason why, their elimination or delay, induces strong flow separation at the end of the roof. Another approach to study the influence of the side pillar on the near wake development was performed by Venning et al. [62]. The width of the 25° Ahmed body was increased to reduce the proximity of the side pillar effects to the body centerline. It results that, as the C-pillar vortices are moved further apart from the center of the window, the influence

that their downwash has on promoting flow reattachment diminishes [135].

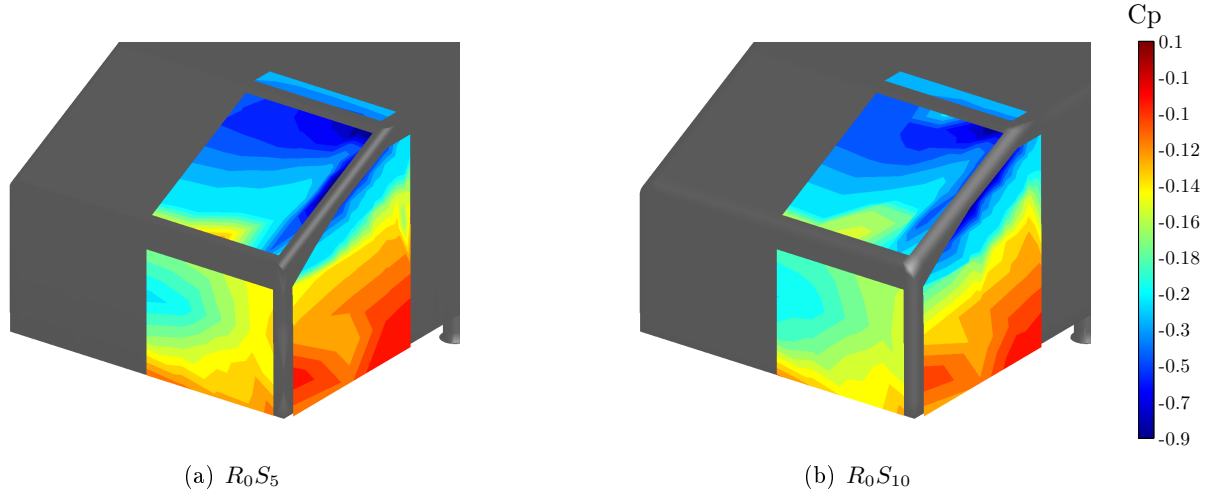


Figure 3.16: Wall pressure coefficient C_p

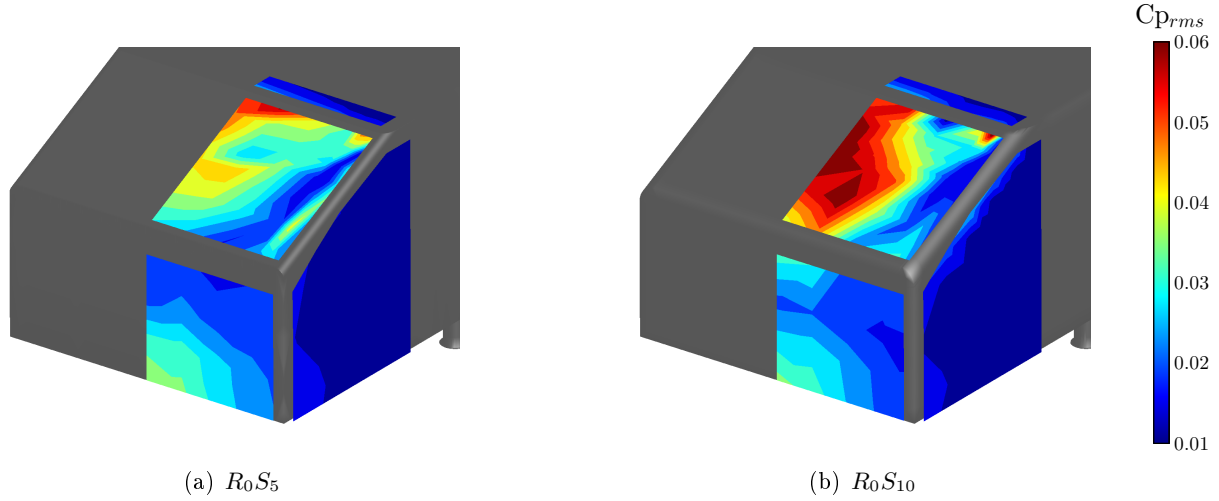


Figure 3.17: Wall pressure coefficient root mean square $C_{p_{rms}}$

Experimental velocity measurements in the symmetry plane, (*figures 3.21(a) and 3.21(b)*) provide a clear picture of the new flow organization. The flow at the roof end experiences a larger separation when compared to the reference case. The reattachment point of the separation bubble is shifted further, from 75% of the rear slant projected length for R_0S_0 , to 81% and 84% respectively for R_0S_5 and R_0S_{10} . The length of the recirculation region downstream the vertical base is shortened. L^* , the length of the mean recirculation region is 0.78 for R_0S_5 and 0.68 for R_0S_{10} , resulting in 12% and 24% reduction with respect to R_0S_{10} . The spanwise contra-rotative structures are then moved closer to the base. Moreover the upper rotating structure results in an increase of the mean spanwise vorticity by 20% for R_0S_5 and 50% R_0S_{10} [115]. Both the shortening of the near wake and the increased spanwise vorticity result in an increase of base drag. *Figures 3.22(a) and 3.22(b)* report

| | Rear window ΔC_p | Vertical surface ΔC_p |
|-------------|--------------------------|-------------------------------|
| R_0S_0 | - | - |
| R_0S_5 | +1% | -10% |
| R_0S_{10} | +14% | -18% |

Table 3.3: Variation in spatially averaged mean C_p over the rear window and vertical surface relative to the reference case R_0S_0 .

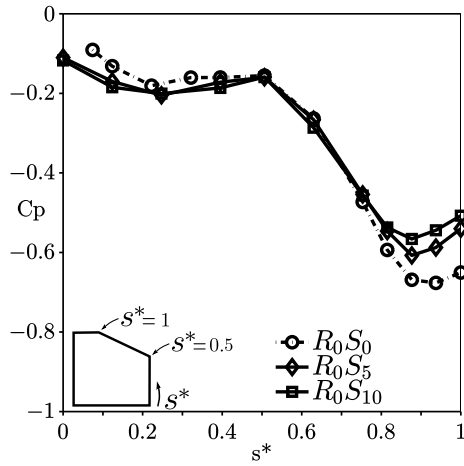


Figure 3.19: Pressure distribution in the symmetry plane ($Y^* = 0$) for all models

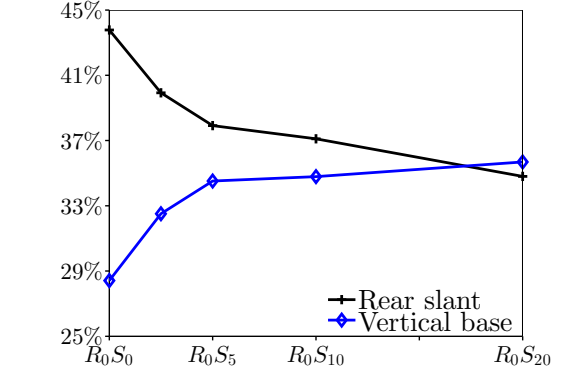


Figure 3.18: Influence of side edges rounding on the contributions to total drag of rear slant and base, numerical simulations

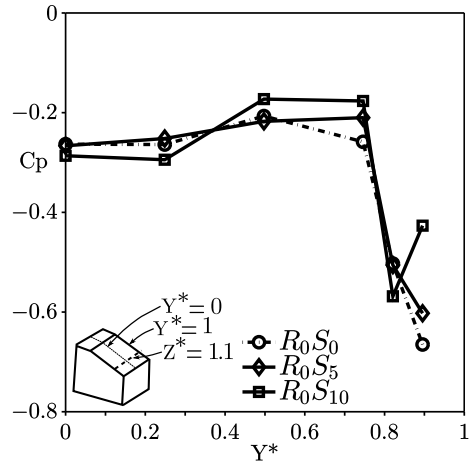
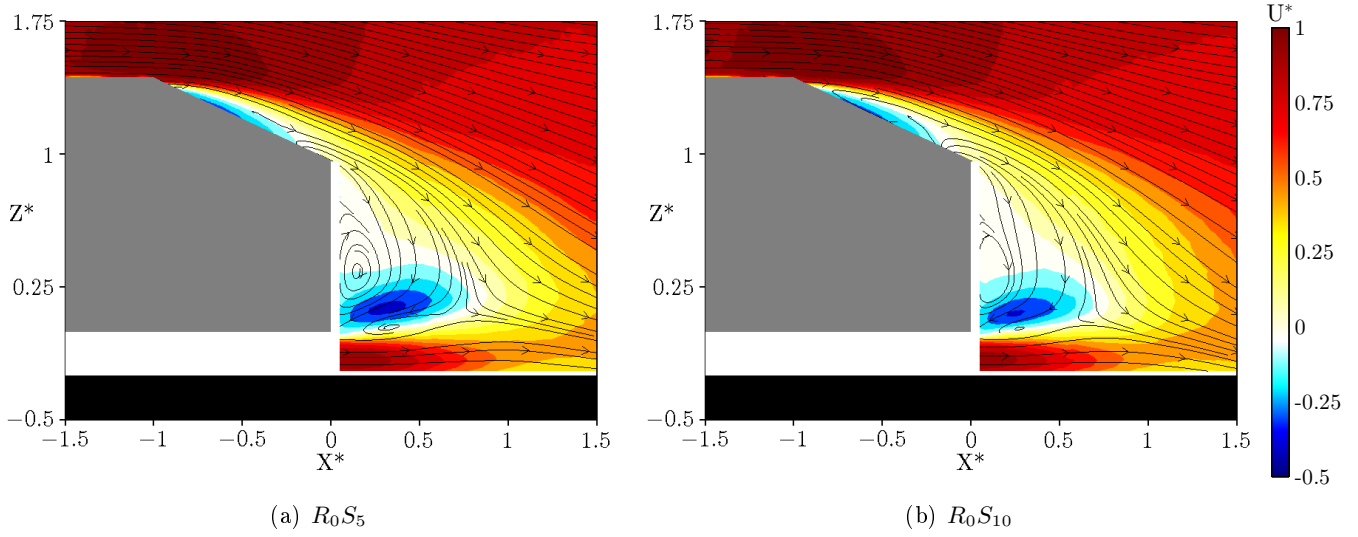
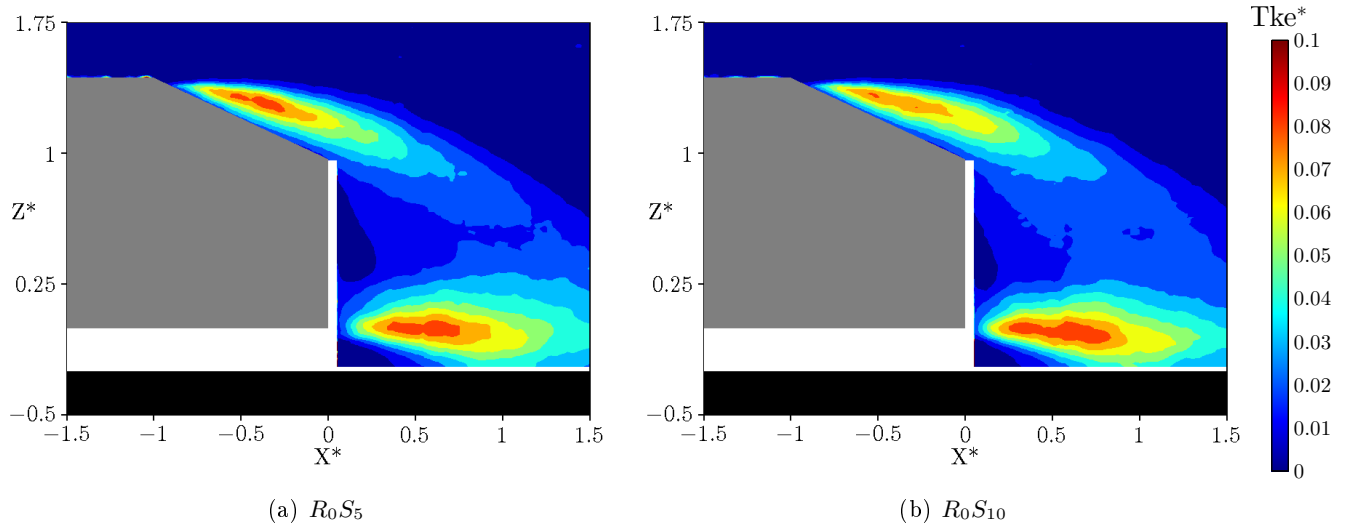


Figure 3.20: Pressure distribution at constant $Z^* = 1.1$ for all models

the contours of the turbulence kinetic energy. The localization of the maximum level of turbulence kinetic energy in the symmetry plane is similar to the reference case R_0S_0 . It is located at the roof end where the sharp edge fixes flow separation. Nevertheless the maximum value is reduced with respect to the reference case for increasing side rounding. It is suggested that the induced velocity of the C-pillar vortices for R_0S_0 , contributes to the high value of turbulence kinetic energy in the symmetry plane. The lower area of high levels of turbulence kinetic energy seems to not be affected by side rounding.

Figure 3.21: Time averaged streamlines and mean streamwise Velocity U^* at $Y^*=0$ Figure 3.22: Turbulent kinetic energy Tke^* at $Y^*=0$

Roof and side edges rounding ($R_{10}S_{10}$)

This last model is an interesting configuration because, its comparison with $R_{10}S_0$, will permit to appreciate in detail the effects of side rounding since the separation bubble is eliminated in both cases by the roof round edge. *Figure 3.23* reports the wall pressure measurements. As previously seen for $R_{10}S_0$, the roof edge allows a fully attached flow over the rear slant.

For $R_{10}S_{10}$, the side radius reduces the C-pillar vortices intensity and thus the pressure footprint, as for R_0S_{10} . It is interesting to notice that the pressure recovery on the slanted surface appears much more effective and uniform along the transverse direction compared to $R_{10}S_0$ (*figures 3.25 and 3.26*). As stated by Fuller et al. [52], the higher central downwash speed over the rear window,

induced by the stronger trailing vortices for the $R_{10}S_0$, is expected to contribute to the lower C_p values in comparison with $R_{10}S_{10}$ case. A weaker C-pillar vortex is also responsible for the more uniform C_p distribution across the backlight [134]. Pressure fluctuations are strongly reduced with respect to R_0S_{10} , since neither separation at the roof edge nor C-pillar vortex are present. Actually, it will be seen in what follows that the side vortices are still present but their intensity is strongly reduced. The averaged streamlines are similar to the $R_{10}S_0$ case over the rear slant, since the flow is fully attached (*figure 3.27*). On the contrary, the contra-rotative structures in the near wake are closer to the base with respect to $R_{10}S_0$ and the size symmetry between the upper and the lower structure seems reduced. In fact, the length of the recirculation region is $L^*=0.9$ in the rounded side configuration $R_{10}S_{10}$, while it was $L^*=1$ for $R_{10}S_0$. The C_p distribution on the vertical base (*figure 3.23*) and the corresponding average surface value (*table 3.4*) indicate a clear decrease in pressure on the base (-32% compared with $R_{10}S_0$) despite the strong increase over the slanted surface. In terms of drag generation, the unfavorable effect on the base balances perfectly the positive effect on the slanted surface. Note that this zero net balance is of course specific to the shape of the rear end and to the ratio between the base height and the vertical projection of the rear window [131].

| | Rear window ΔC_p | Vertical surface ΔC_p |
|----------------|--------------------------|-------------------------------|
| $R_{10}S_0$ | - | - |
| $R_{10}S_{10}$ | +23% | -32% |

Table 3.4: Variation in spatially averaged mean C_p over the rear window and vertical surface relative to the roof rounded case $R_{10}S_0$.

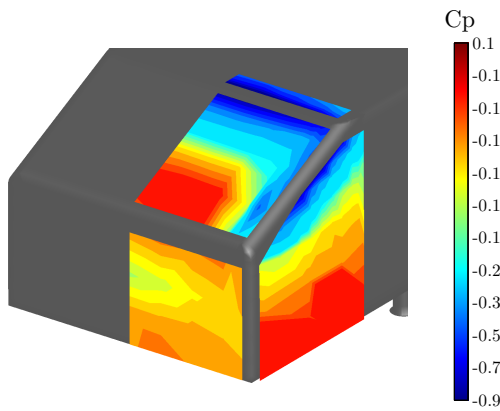


Figure 3.23: $R_{10}S_{10}$, wall pressure coefficient C_p

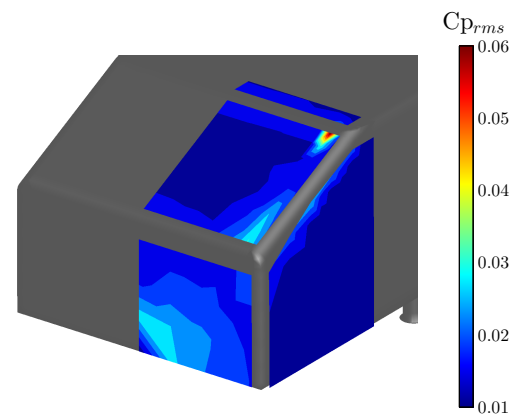


Figure 3.24: $R_{10}S_{10}$, wall pressure coefficient root mean square $C_{p_{rms}}$

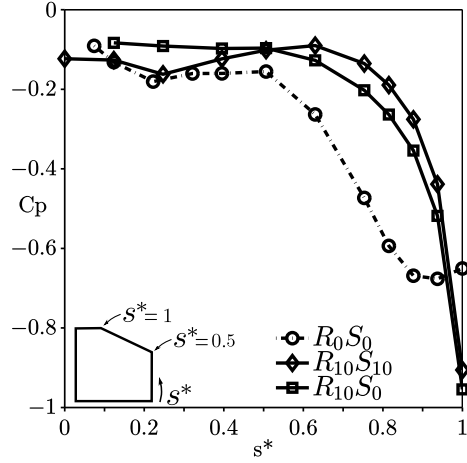


Figure 3.25: Pressure distribution in the symmetry plane ($Y^*=0$) for all models

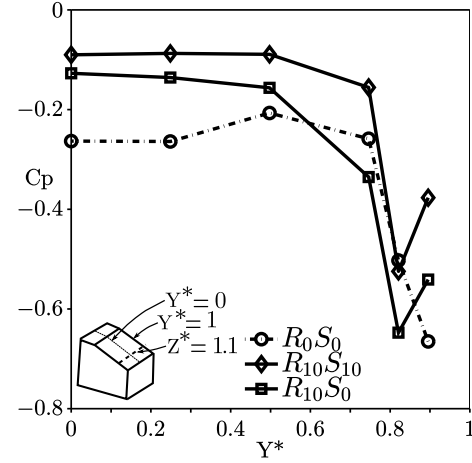


Figure 3.26: Pressure distribution at constant $Z^*=1.1$ for all models

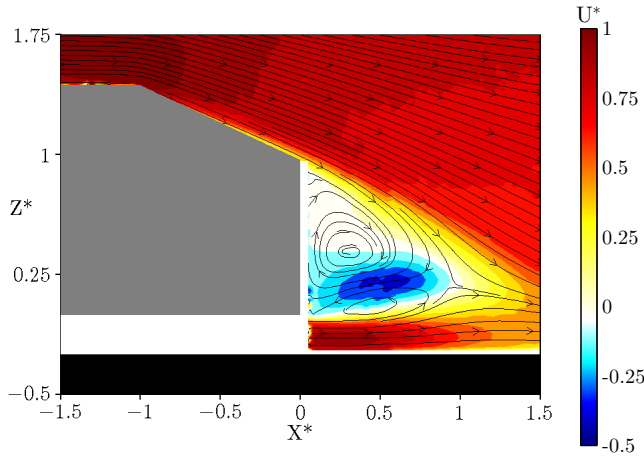


Figure 3.27: $R_{10}S_{10}$, time averaged streamlines and mean streamwise Velocity U^* at $Y^*=0$

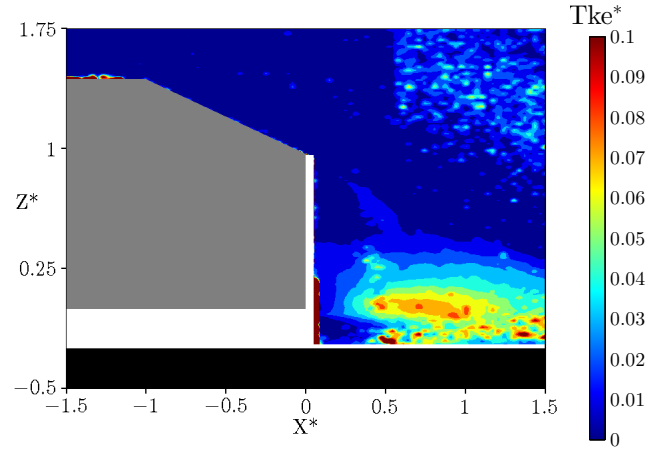


Figure 3.28: $R_{10}S_{10}$, turbulent kinetic energy Tke^* at $Y^*=0$

3.2 3D effects of pillar rounding on the near wake development

In this section, additional experimental measurements are reported to establish a fine comparison between $R_{10}S_0$ and $R_{10}S_{10}$ models and to describe the way side rounding modifies the 3D flow organization in the near wake.

3.2.1 Oil flow visualizations

Oil flow visualizations were performed to investigate the skin friction lines (figure 3.29). White and black lines were superimposed to the pictures to emphasize the main flow structures for both models. On the side of the models, the dashed black line represents the attachment line of the primary vortex and the solid white line the separation line of the secondary vortex [69]. The separation of the primary vortex as well the attachment of the secondary vortex are not shown in the picture.

In the recent automotive aerodynamics literature over the Ahmed body, a third small vortex is evidenced by the experimental work of Jermann et al. and the numerical simulation of Krajnović et al. [71, 136]. This structure was not observed in the presented work neither with the oil flow visualization nor with the S-PIV measurements presented in what follows. Closer to the center region, skin friction lines cannot be interpreted directly and long black arrows indicate the overall direction of the flow along the surface. These lines are drawn in agreement with the Stereo-PIV visualization presented in what follows. It can be observed also that the C-pillar vortex footprint is wider for the $R_{10}S_0$ case and, moreover, its origin is shifted downstream for $R_{10}S_{10}$. On the upper part of the rounded pillar model, $R_{10}S_{10}$, some attached flow penetrates toward the center line. That flow comes from the side of the model and does not roll up directly in the C-pillar vortex as in the sharp case, but enters directly over the rear window.

The analysis of the oil flow visualization brings to evidence the different topologies of the skin friction lines over the rear window due to the geometrical differences of the side rear pillars of the models.

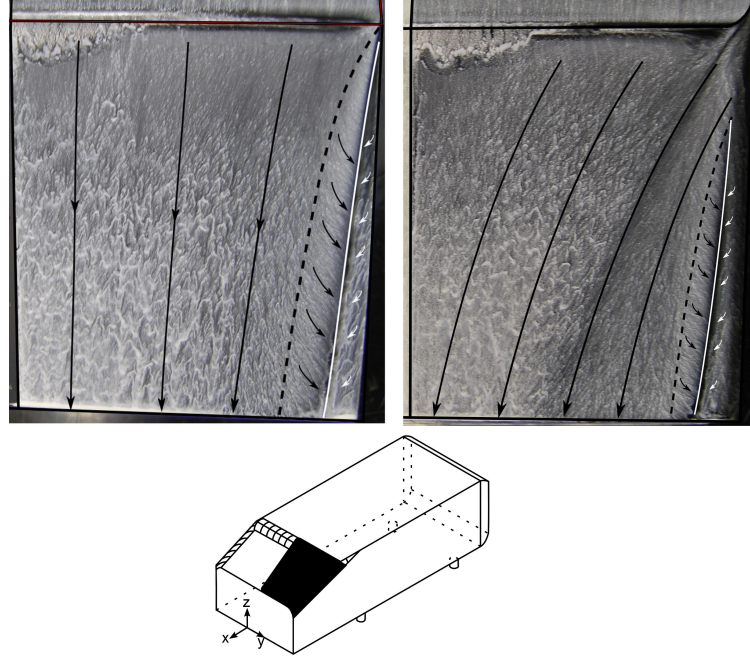


Figure 3.29: Oil flow visualization: Left: $R_{10}S_0$. Right: $R_{10}S_{10}$. Dashed black line is the attachment line of the primary vortex, solid white line is the separation line of the secondary vortex. Bottom: Position of the paint visualization.

3.2.2 Cross-flow analysis

To achieve a better understanding of the flow modifications generated by the side rounding, velocity cross-flow planes are reported in this section. The length of the recirculation region L^* is used as a scale quantity to keep consistency among the models in the way the cross-flow planes cut the rotating spanwise structure of the near wake. In fact, as seen in the 2D analysis of the symmetry

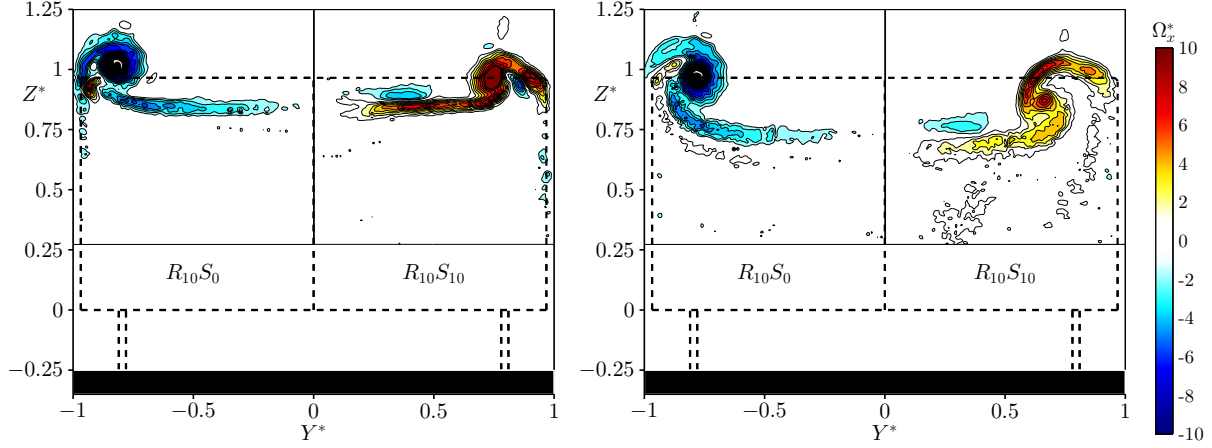


Figure 3.30: Mean Streamwise Vorticity $\Omega_x^* = \frac{\Omega_{x*}\xi}{U_0}$, left plane at $X^* = L^*/4$, right plane at $X^* = L^*/2$. The dashed lines represent the geometry of the model.

plane, differences are shown at the position of the saddle point between $R_{10}S_0$ and $R_{10}S_{10}$.

At first, it is proposed to analyze the streamwise vorticity to get a quick picture of the main differences between the $R_{10}S_0$ and $R_{10}S_{10}$ models. Contours of the mean streamwise vorticity in the planes $X^* = L^*/4$ and $X^* = L^*/2$ are proposed in *figure 3.30*. Small values of streamwise vorticity are not displayed, so as to focus the attention on the main vortical structures generated from the side pillars. Each picture is divided in two: the left side represents the $R_{10}S_0$ configuration and the right side the $R_{10}S_{10}$ one. The data are all recorded for $Y^* \in [0; 1]$, so the data visualization related to $R_{10}S_0$ are a mirror symmetry.

At $X^* = L^*/4$ (i.e. $X^* = 0.25$ and $X^* = 0.22$ for $R_{10}S_0$ and $R_{10}S_{10}$), higher concentration of streamwise vorticity due to the sharp edge is remarked for $R_{10}S_0$ with respect to $R_{10}S_{10}$. The secondary vortex, mentioned in the oil visualizations, is also observed for $Y^* \approx \pm 0.9$ and $Z^* \approx 0.9$ in both models. A small region of negative vorticity is also observed for $Y^* \approx 0.4$ and $Z^* \approx 0.9$ just for $R_{10}S_{10}$. A closer look at the oil visualizations in *figure 3.29* and to V^* in *figure 3.31(b)* shows that the vorticity sign change occurs in the zone of confluence between the flow over the top of the body and the lateral flow drawn from the side. In that region, a clear change of sign of the gradient $\frac{\partial V^*}{\partial z}$ is observed (*figure 3.31(b)*), and this contributes to the change of sign of the streamwise vorticity. In the past literature over the reference Ahmed body, a similar region of opposite vorticity with respect to the C-pillar vorticity, located close to the symmetry plane, has been investigated over the reference Ahmed body by Depardon et al. [127] and Spohn et al. [69]. Authors attributed this vorticity to the vortex filaments emanating from the separation bubble wall-foci. Wang et al. [77] remarked as well this area of vorticity, but they related it to the shear layer interaction with the upper recirculation structure of the near wake. Moreover, the PhD work of Bingfu associated, to this area, the same frequency as the front separation bubble at the forebody [90].

To confirm that in the present work the small region of negative vorticity is associated to the flow coming from the side for $R_{10}S_{10}$, since moreover no separation occurs at the roof end, additional hot wires measurements were performed over 1:2 scaled Ahmed body with the same roof and side radius.

This work was performed in the framework of the 3rd year project of Gaignard and Lagny [137]. In their experiments, one hot wire velocimetry probe was placed in the area of opposite vorticity at the end of the rear slant, while another synchronized hot wire investigated the rear slant flow. The maximum correlation between the hot wires was achieved when the mobile wire was placed in the zone where the flow overcomes the rounded pillar. Those tests confirmed that in the case of a rounded edge, the area of opposite vorticity is directly related to the side flow that overcomes the edge.

A second cross flow plane in the wake is presented in what follows to investigate the way longitudinal vorticity is distributed in the near wake. The plane is located at half of the length of the near wake, $X^* = L^*/2$ (i.e. $X^* = 0.5$ and $X^* = 0.45$ for $R_{10}S_0$ and $R_{10}S_{10}$) and it is reported in the right side of *figure 3.30*. A concentrated region of vorticity for $R_{10}S_0$ associated to the longitudinal vortex is still remarked. For the rounded case, the streamwise mean vorticity is distributed over a wider area of the near wake and the opposite vorticity area is still present ($Y^* \approx 0.3$ and $Z^* \approx 0.75$). The core of the C-pillar vortex is located around $Y^* \approx 0.8$ and $Z^* \approx 1$ for $R_{10}S_0$, while it is lower and farther from the side for the rounded case, around $Y^* \approx 0.7$ and $Z^* \approx 0.9$.

Figure 3.31(a) reports the streamwise velocity U^* at $X^* = L^*/4$. The C-pillar vortex shows a small loose of data in its core due to the centrifugal force that ejected the oil drops, resulting in a poor particle density [53]. It has been chosen to present the results with this default in order to avoid any spatial filtering of the data. Close to $Y^* = 0$, the streamwise velocity near the wall is higher for $R_{10}S_0$ with respect to $R_{10}S_{10}$ due to the downwash velocity induced by the C-pillar vortices. As shown in *figure 3.23*, the loss of the induced velocity due to the rounded edge, resulted in an increase of pressure over the slanted surface close to the symmetry plane for $R_{10}S_{10}$. The spanwise velocity in *figure 3.31(b)*, evidences for the sharp side two opposite areas associated to the rotation of the vortex, while for $R_{10}S_{10}$ an intense traversal velocity towards the centerline is remarked. The rotation of the vortex can be noticed as well in *figure 3.31(c)* thanks to the alternate sign of the normal velocity. The induced velocity by the C-pillar vortices is also visible in the centerline, where the normal velocity is more intense for $R_{10}S_0$ than $R_{10}S_{10}$.

The contours of Γ_2 criterion, computed using V^* and W^* velocity components, report the rotational behavior of the flow. 2-D lines tangent in each point at the vector (V^*, W^*) are also drawn in *figure 3.31(d)*. Of course, these lines are not meant to be mean streamlines. At $X^* = L^*/4$, contours of Γ_2 underline the side pillar vortices for both rear ends (*figure 3.31(d)*). The change of direction of the “streamlines” at $Z^* \approx 0.8$, localized the position of the shear layer. The criterion also bring to evidence the area of opposite vorticity for $R_{10}S_{10}$ around $Y^* \approx 0.4$ and $Z^* \approx 0.9$. Other areas of coherent rotation are revealed by the Γ_2 criterion around $Z^* \approx 0.6$ for both models, but they do not seem related to any characteristic structures of the near wake and they are not consistent with the “2D streamlines”.

At $X^* = L^*/2$, a different organization of the near wake flow should be highlighted (*figure 3.32*). The horizontal shear layer downstream the slanted surface separation is transported downward when rounded edges are present. The topology of the mean near wake flow of the recirculation bubble is thus changed. When comparing the transverse velocities (V^*) in the horizontal shear layer region

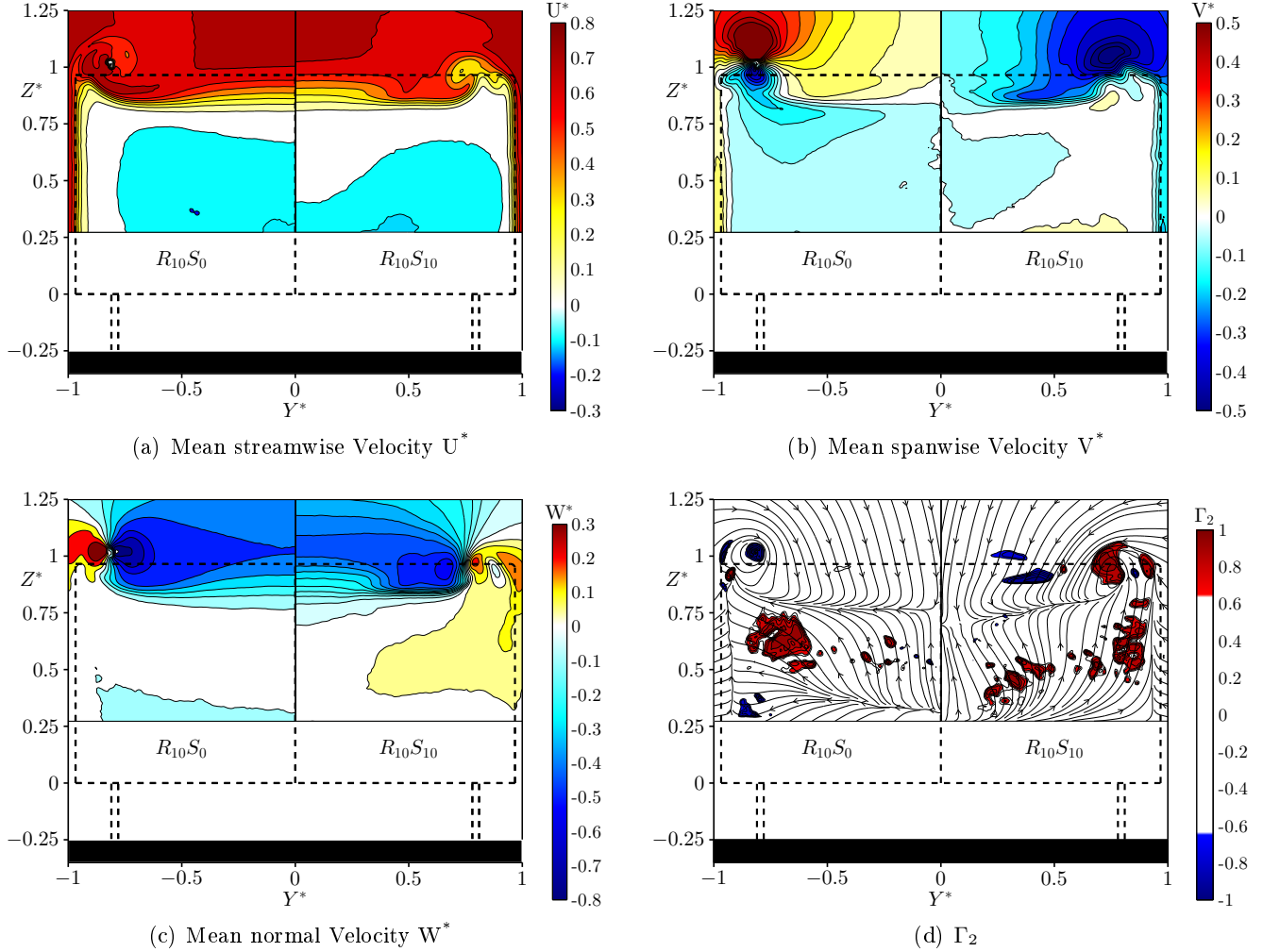


Figure 3.31: Plane at $X^* = L^*/4$. The dashed lines represent the geometry of the model.

downstream of the slanted surface, the inward motion is clear for $R_{10}S_{10}$ while significant inward V^* values are just localized around the vortex core for $R_{10}S_0$. For the rounded case, *figure 3.32(c)* shows that this mean inward motion before separation results in a strong downwash effect (negative W^*) in the core region of the wake.

As a general reminder, for rear end with a slanted angle, a pressure gradient is induced between the side of the model and the rear end [26]. As a consequence, the flow along the side is drawn towards the center. The sharp side pillars forces the lateral flow to separate, generating longitudinal vortices. One could therefore suggest that, for $R_{10}S_0$, the sharp lateral edges "shield" the wake separation region at the base and enables a "two-dimensional" separation, "2D" meaning that the mean streamlines at separation are more parallel to the orientation of the flow over the window, while longitudinal vorticity is concentrated in the C-pillar vortices. On the contrary, for rounded edges, the flow is drawn in from the sides, towards the center over the slanted surface. The separation at the base is then notably 3D for $R_{10}S_{10}$, associated with high spanwise and vertical velocity components.

For rounded rear ends, the three dimensional property of the near wake structure therefore results in more pronounced streamline curvatures and lower pressure on the base when compared with a similar model featuring sharp lateral edges. Note that the downward deviation of the mean streamline separating from the slanted surface is particularly manifest when looking at the orientation of the streamlines in the plane of symmetry in *figure 3.27*.

Contours of Γ_2 in *figure 3.32(d)* clearly show the overall rotation of $R_{10}S_{10}$ wake around the longitudinal axis. For $R_{10}S_0$, a concentrated region of Γ_2 corresponds to the C-pillar vortex. For $R_{10}S_{10}$, the criterion reveals a zone of coherent rotation around the pillar vortex and a large zone in the center bottom region of the wake. The high spanwise and vertical velocities associated to the transversal flow therefore results in a large scale rotation of the flow in the near wake that will be discussed more quantitatively in what follows (see *figure 3.35* and associated comments).

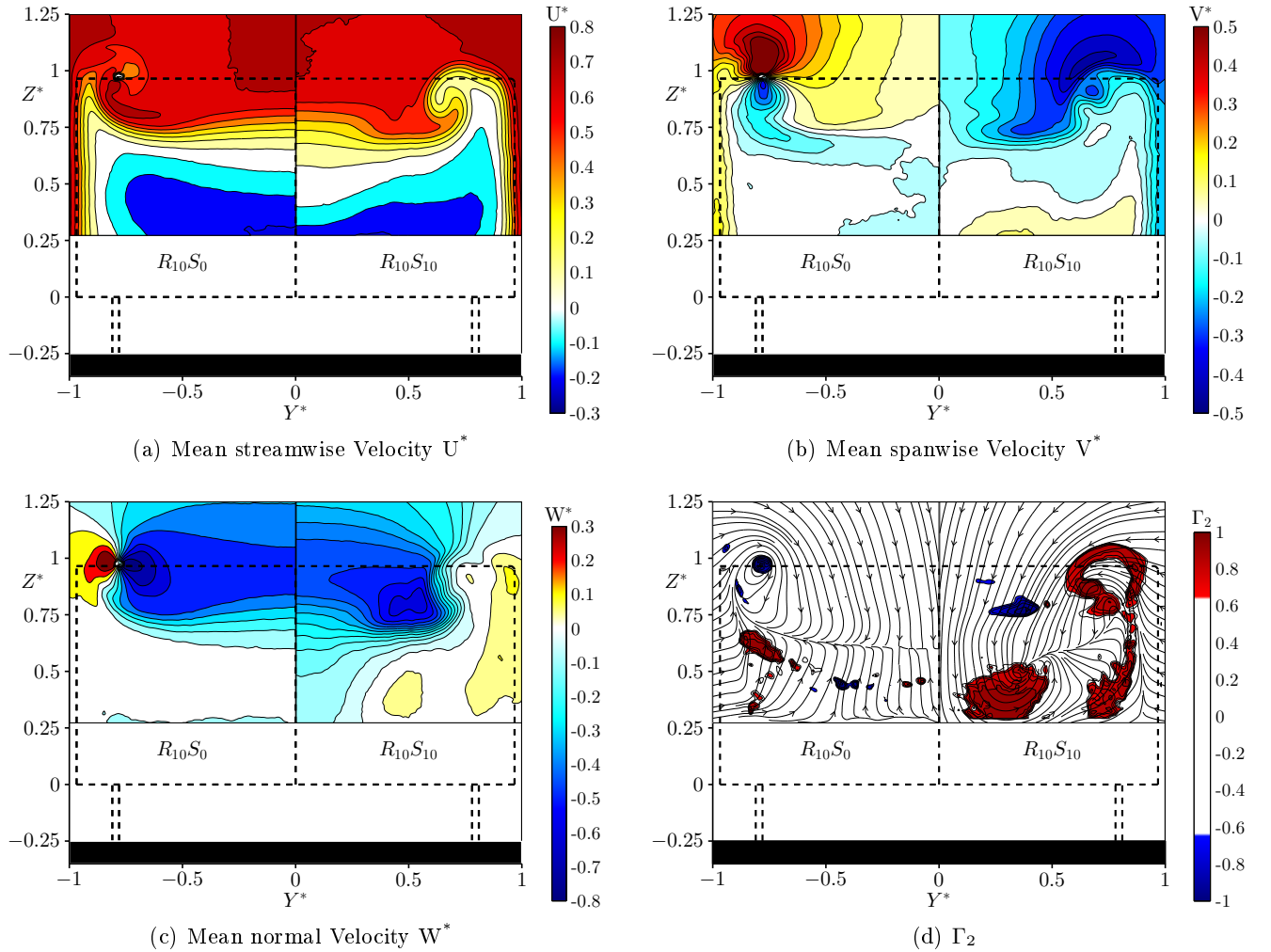


Figure 3.32: Plane at $X^* = L^*/2$. The dashed lines represent the geometry of the model.

The downwash effect is also especially clear when looking at *figure 3.33*, which compares the turbulent kinetic energy at $X^* = L^*/4$ and $X^* = L^*/2$. The 3D shear layers and the wake recirculating

region (see the region of negative U^* in *figure 3.32(a)*) are the location of a large fluctuating level. Close to the vertical base, at $X^* = L^*/4$, no differences are noticed, the maximum value of the turbulent kinetic energy is located inside the shear layer. At $X^* = L^*/2$ the "potential" outer flow, characterized by a low level of turbulent kinetic energy, penetrates downward in the near wake of the $R_{10}S_{10}$ model. As a consequence, the fluctuating kinetic energy is much lower in this region, as shown in the zone around $Y^* \in [0; 0.2]$ and $Z^* \in [0.3; 0.75]$. High levels of fluctuations in the low part of the plane are associated to the upper recirculation structure in the near wake. Left side of *figure 3.34* reports the turbulent stress terms at $X^* = L^*/2$ for both models. The fluctuations related to the streamwise velocity are negligible for both models except into the vortex core. High levels of spanwise fluctuations are present just in $R_{10}S_0$ close to the vortex core. Finally, the main fluctuations, responsible then for the overall value of the turbulent kinetic energy around the main shear layer, are the ones related to the normal velocity and are located in the shear layer region. Regarding the "potential outer flow" injected in the near wake by the downwash imposed by the rounded edge, it is remarked in all the terms of the turbulent stress. In fact, for $R_{10}S_0$, around around $Y^* \in [0; 0.2]$ and $Z^* \in [0.3; 0.75]$ an area of zero fluctuations is easily detectable. The shear stress terms are reported in right side of *figure 3.34*. Differences are present around the vortex core between the two models in all the terms whereas outside the vortex core only for $\overline{uw^*}$ and $\overline{vw^*}$ some differences are highlighted.

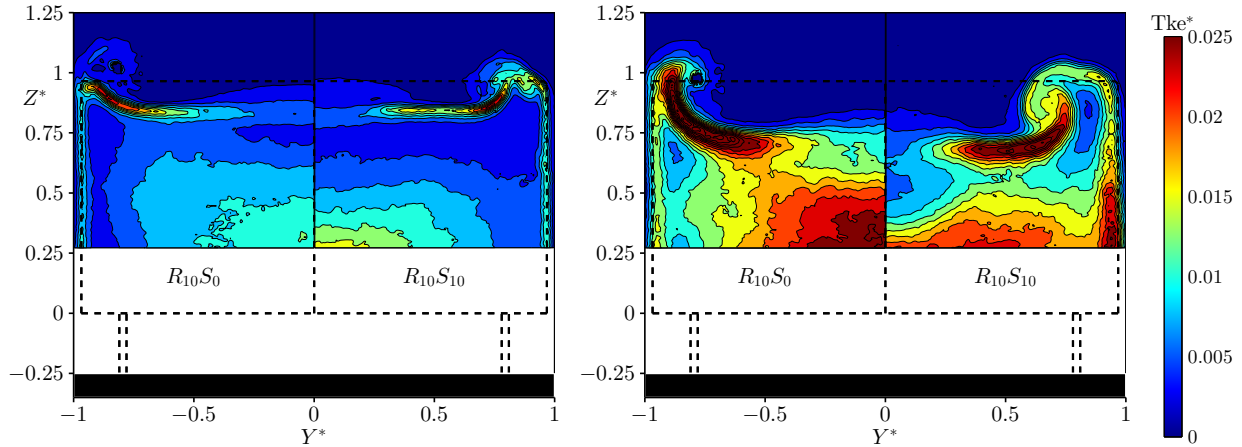


Figure 3.33: Turbulent kinetic energy Tke^* , left plane at $X^* = L^*/4$, right plane at $X^* = L^*/2$. The dashed lines represent the geometry of the model..

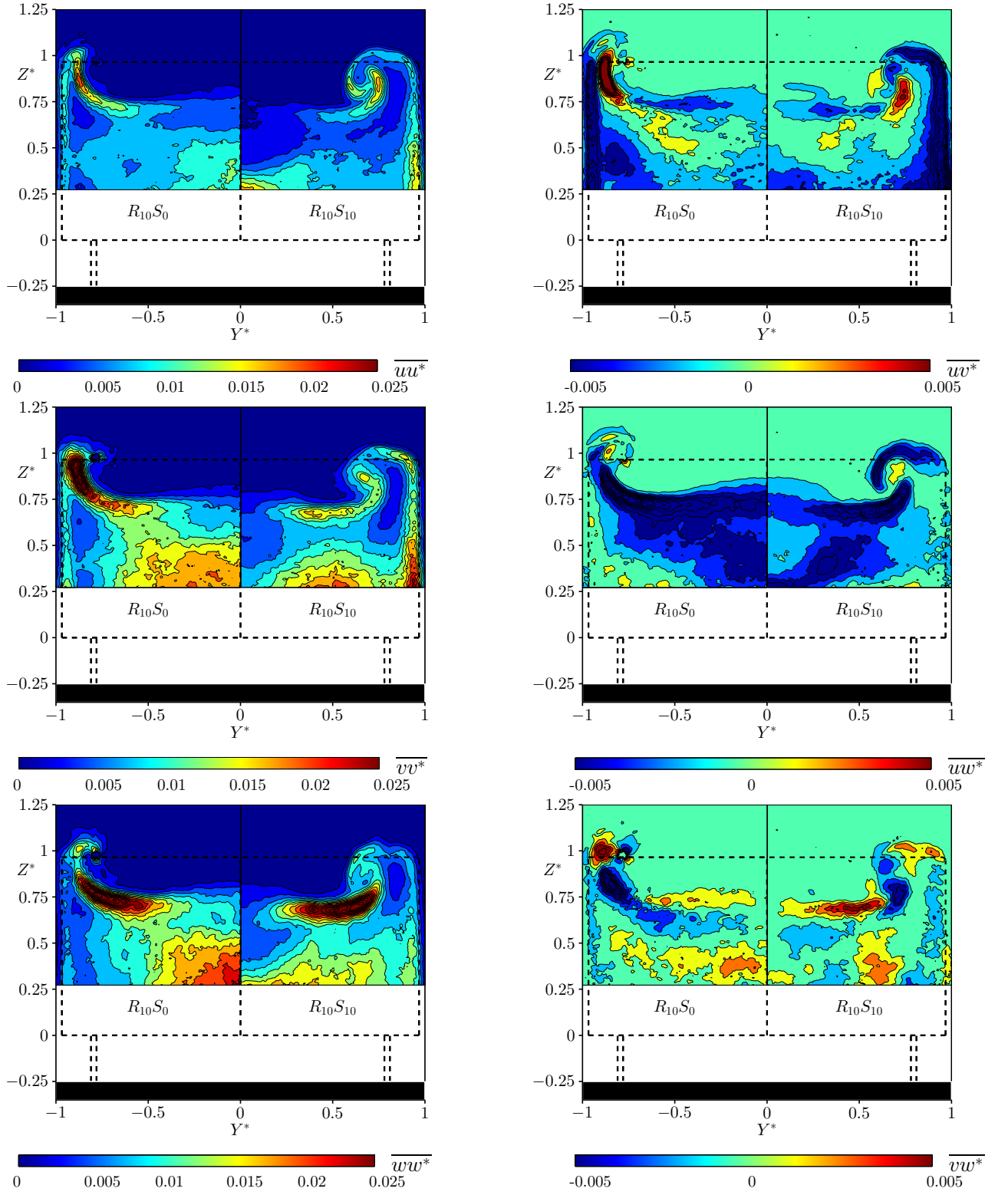


Figure 3.34: Turbulent stress terms. Plane at $X^* = L^*/2$. The dashed lines represent the geometry of the model.

Analysis of the 3D near wake

Along three-dimensional geometries, 3D vorticity is generated at the wall along the curved surface, transported, tilted and stretched in the 3D boundary layer region. In what follows, it is proposed to discuss some integral properties of the longitudinal vorticity field along the near wake of the body. One specificity and limitation of the data presented is that, contrary to the recent study of Venning et al. [62], the detailed Stereo-PIV database only concerns velocity planes measured near the rear vertical surface. This region spans approximately over half of the mean recirculating bubble (see *figures 3.21(a)* and *3.27*) where the mean recirculating flux is significant. Moreover, the model used here being four times as large as the body of Venning et al. [62], the field of view of each plane does not include the full height of the wake. The under-hood flow and the bottom region of the wake are not captured. The following discussion must therefore be considered as qualitative. It was however checked that all conclusions discussed here are consistent with the results from the numerical simulations including a wider area.

The longitudinal evolution of the mean circulation $\Gamma^* = \int_{S^*} \Omega_x^* dS$ and the flux of mean longitudinal vorticity $F_x^* = \int_{S^*} U^* \Omega_x^* dS$ are plotted in *figure 3.35(a)* for both $R_{10}S_0$ and $R_{10}S_{10}$. As circulation is the integral of the longitudinal vorticity, it is natural to consider the balance of Ω_x as a constitutive structural element of the wake. Numerical results are reported as well in *figure 3.35*. These results are divided in two figures: one corresponds to the same area of the experimental data (*figure 3.35(b)*) and the second reports the evolution of Γ^* until $X^* = 3$ for a larger area compared with the experimental data, i.e. $Y^* \in [0, 1]$, $Z^* \in [-0.25, 1.5]$ (*figure 3.35(c)*).

First, it is noticed that F_x^* is in the order of 0.13 for $R_{10}S_{10}$ and 0.25 for $R_{10}S_0$ at $X^* = L^*/2$. F_x^* is a non-dimensional quantity, in which the scaling quantity is ξU_0^2 . The scaling length ξ is equal to 201mm. The length l of the perimeter of the model vertical base is about $l \approx 5.8\xi$. In the ideal case of a 2D boundary layer of thickness δ and external velocity U_0 separating at a sharp edge, the absolute value of the flux of vorticity per unit span reads simply as $|F_\perp| = \int_0^\delta U \frac{\partial U}{\partial n} dn = \frac{U_0^2}{2}$ where n is the direction perpendicular to the wall and $-\frac{\partial U}{\partial n} = \Omega_\perp$ denotes the only non-zero component of the vorticity vector [138]. By integration of the absolute value of the vorticity flux along the perimeter of the vertical base, an order of magnitude of the total longitudinal mean flux of vertical and transversal mean vorticity shed at the base of the body is therefore $F_{YZ} \approx \frac{U_0^2 l}{2}$. Comparing this order of magnitude with $2F_X$ (F_X concerns approximately half of the wake surface), it is obtained $2F_X/F_{YZ} \approx 4\xi F_X^*/l \approx 2F_X^*/3$ that is to say $2F_X/F_{YZ} \approx 0.08$ for $R_{10}S_{10}$ and $2F_X/F_{YZ} \approx 0.16$ for $R_{10}S_0$. It is therefore shown that the flux of organized longitudinal vorticity downstream the base is only a small portion of the base total flux. However, this experiment shows that it has a significant global incidence on the pressure distribution and drag of the body.

The second observation is that F_X^* is nearly constant for $R_{10}S_{10}$ and increases moderately for $R_{10}S_0$ (a 25% increase over the measurement region). Integrating the longitudinal vorticity equation in a control volume bounded by two measurement planes at X^* and $X^* + \Delta X^*$, the longitudinal evolution of F_X^* is due to the flux of Ω_x^* across the lateral boundaries and to the integral of the source terms in the control volume (viscous diffusion can be neglected at this Reynolds number; turbulent transport

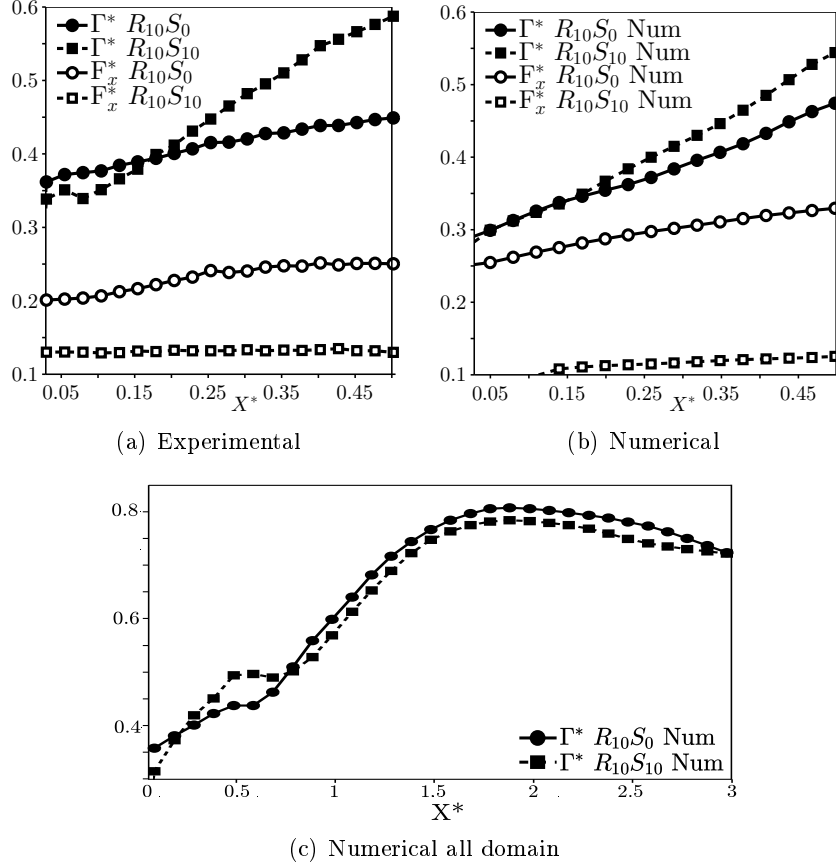


Figure 3.35: Longitudinal evolution of the mean circulation and the flux of mean longitudinal vorticity in the near wake.

was not evaluated but should be zero along the plane of symmetry and negligible if the boundaries of the control volume are out of the wake, which is not the case here for the base). The source terms correspond to the average of the stretching of longitudinal vorticity $\Omega_x \frac{\partial U}{\partial x}$ and of the tilting of lateral and vertical vorticity $\Omega_y \frac{\partial U}{\partial y} + \Omega_z \frac{\partial U}{\partial z}$ (Tennekes and Lumley [139], Chassaing [140]). In the present case, it was checked that the non-dimensional lateral and vertical fluxes are significantly smaller than the longitudinal flux of vorticity (smaller than 5% of F_x^*). Figure 3.35(a) shows that the net effect of the source terms over the measurement volume is small for $R_{10}S_0$ and negligible for $R_{10}S_{10}$. From an integral point of view, the longitudinal mean transport of mean longitudinal vorticity seems therefore to be the dominant term in the near wake.

The third observation relative to figure 3.35(a) is that, despite the constancy of the flux, the integral of the vorticity over the measurement domain, Γ^* , increases significantly. The rate of increase is notably greater for $R_{10}S_{10}$ than for $R_{10}S_0$, about 3 times as much for the former as for the latter. To simply understand this observation, it was chosen to divide the total domain in two fixed parts (see sketch in 3.36). This partition is quite arbitrary, but is sufficient for the discussion. Region "1" includes the C-pillar vortex and covers 1/4 of the field of measurements: $Y^* \in [0.44, 0.89]$, $Z^* \in [0.75, 1.25]$. Region "2" is the remaining area. Γ^*1 (resp. Γ^*2) represents the circulation associated with region "1" (resp. "2"). Naturally it is computed also $\Gamma^* = \Gamma^*1 + \Gamma^*2$. Figure 3.36 displays

this decomposition at $X^* = L^*/2$. It is clear that circulation Γ^*1 in the region including the vortex is larger for $R_{10}S_0$ than for $R_{10}S_{10}$. This is related to the higher circulation gathered in the C-pillar vortex. However, while Γ^*2 is less than 5% of the total value of Γ^* for $R_{10}S_0$, it is about 50% of the total circulation for $R_{10}S_{10}$. The 3D wake generated by rounded C-pillar therefore significantly differs from the sharp pillar configuration in that the longitudinal vorticity is transported in the core of the wake in a more distributed way. This is consistent with *figure 3.30* in which this observation was already made. The fact that the flux F_X^* is a constant is surprising but does not contradict this observation, because a significant part of the vorticity distributed in region "2" is associated to a reversal flow. For the rounded case, this upstream transport of longitudinal vorticity very close to the base of the body is responsible for low pressure regions and more drag. The experimental behavior of F_X^* and Γ^* is well predicted by the numerical simulation in $X^* \in [0, 0.5]$ (*figure 3.35(b)*). It is interesting to notice that after the closure of the recirculation bubble, $X^* \approx 1$, the mean longitudinal vorticity experienced an important growth for both models (*figure 3.35(c)*). The mean circulation after the saddle point results to be higher for $R_{10}S_0$ than $R_{10}S_{10}$. At this point, the flow field is dominated by a global rotation around the spanwise axis. The residual intensity due to the C-pillar vortex could be responsible for this high value. This is consistent also with the fact that $R_{10}S_0$ has a higher lift than $R_{10}S_{10}$.

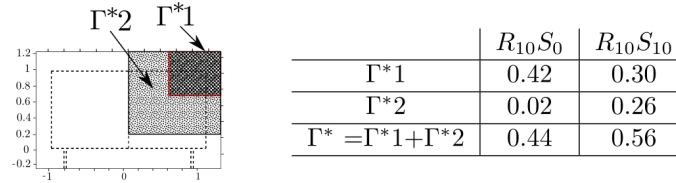


Figure 3.36: Zone of calculation and values of circulation at $X^* = L^*/2$. The dashed lines represent the geometry of the model.

It is noteworthy that the concept of induced drag can be applied to streamlined body to express the drag related to lift by a wake survey [141]. For blunt body, characterized by strong contribution of pressure drag to the total drag, the induced drag evaluation by wake analysis seems to not be accurate. In fact, the wake of blunt body, such the Ahmed body, is characterized by large scale rotation in the near wake that do not contribute directly to the overall lift. It results moreover that, as reported in *figure 3.35*, the presence of an opposite behavior of the wake circulation with regard to the position in the wake. Howell and Le Good [142] reported that the vortex drag factor is strongly dependent on model width and is also a function of the body bluntness [142]. The strong tridimensional behavior of the near wake coupled with the important pressure lost due to the bluntness of the body, should impose caution in the use of the use of wake survey to estimate the body aerodynamics performances. In the work of Greiner it can be found an interesting summary of calculated drag errors among many authors according to the choice of the wake plane location [101].

3.2.3 Schematic representation of the wake

In order to synthesize the previous analysis, a conceptual model of the flow structure around the modified Ahmed models is proposed in *figure 3.38*. The idea is to resume in a “simple” draw the main modifications induced by afterbody rounding. At first, the numerical mean streamlines are reported in *figure 3.37* to help the reader to better visualize the flow organization in the near wake and its modification due to side pillar rounding. It can be stated again that the separation at the sharp edges shields the wake separation at the base and enable a “two-dimensional” separation while it is notably 3D for the rounded model. It results that a significant portion of the longitudinal vorticity shed at the base recirculates in the near wake for rounded C-pillars and is responsible for the large amount of circulation measured in this region.

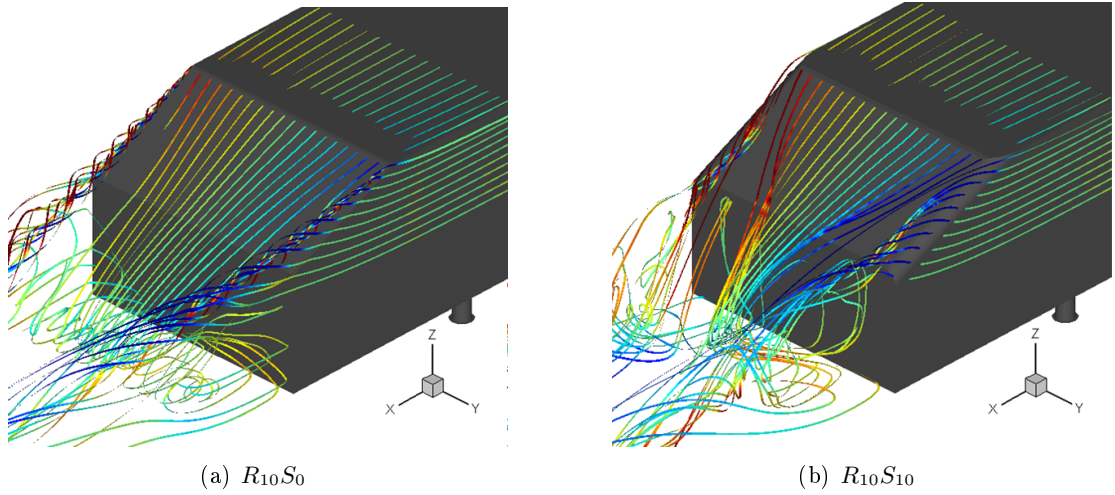


Figure 3.37: Mean numerical streamlines.

In *figure 3.38(a)* and *3.38 (c)* the characteristic near wake structures are drawn. Over the rear window, the differences between the models are related to the delayed origin of the C-pillar vortex and the consequent edge overcoming by the flow coming from the side for $R_{10}S_{10}$ (red lines in *figure 3.38(c and d)*). On the contrary, the sharp edge gathers all the flow coming from the side inside the pillar vortex (blue lines in *figure 3.38(a and b)*). The counter-rotating structures in the near wake are drawn closer to the base for $R_{10}S_{10}$ due to the downwash effect of the side flow that tends to move them closer compared to $R_{10}S_0$. For $R_{10}S_0$, a streamline coming from the upper structure towards the C-pillar vortex is reported following the work of Venning et al. [62]. Even though the interaction between the upper structure and the C-pillar vortex would need deeper investigation, especially on the tilting of the spanwise vorticity in streamwise vorticity, it seems a reasonable solution to assume an interaction between these structures. This interaction was also underlined qualitatively in the water tunnel visualizations by [68]. For $R_{10}S_0$, the bending of the lower structure along the normal axis of the near wake is drawn in agreement with what proposed by Krajnović et al. [71]. It means that, the lower rotating structure, approaching the edge of the model, is tilted towards the normal axis due to the interaction with the side shear layer. On the contrary this behavior was not observed

for $R_{10}S_{10}$. It seems that the downwash in the near wake limits the normal bending of the lower structure forcing it to be tilted directly in the streamwise direction.

The cross-flow streamlines extracted from a plane at $X^* = 1.5$, show how the far wake is characterized for both model by a dominant rotation around the X axis (figure 3.38(b and d)). The center of this coherent movement is around the C-pillar vortex for $R_{10}S_0$. The rounded edge, promoting a strong downwash in the near wake, modifies the location of the longitudinal rotation center. In fact, if “d” is the center distance to the symmetry plane and “h” the height respect to the floor, both quantities for $R_{10}S_{10}$ are smaller than the ones related to $R_{10}S_0$. It is interesting to notice that the large scale rotation around the x axis, is a global flow characteristic generated by the pressure difference over the body. The rear slant imposes a pressure gradient that induces the flow from the side to overcome the edge and generate a large scale rotation around x-axis in the wake, no matter the side edge radius. It characterized then the wakes of both models. A sharp edge radius imposes the overcoming flow to separate generating C-pillar vortices. These vortices gather most of the flow resulting in a “axis” for the longitudinal large scale rotation. The displaced origin of the C-pillar vortices due to side rounding and its consequences on the rear slant flow, induces the large scale rotation to be closer to the rear surface generating then a modification of the global flow characteristic rotation.

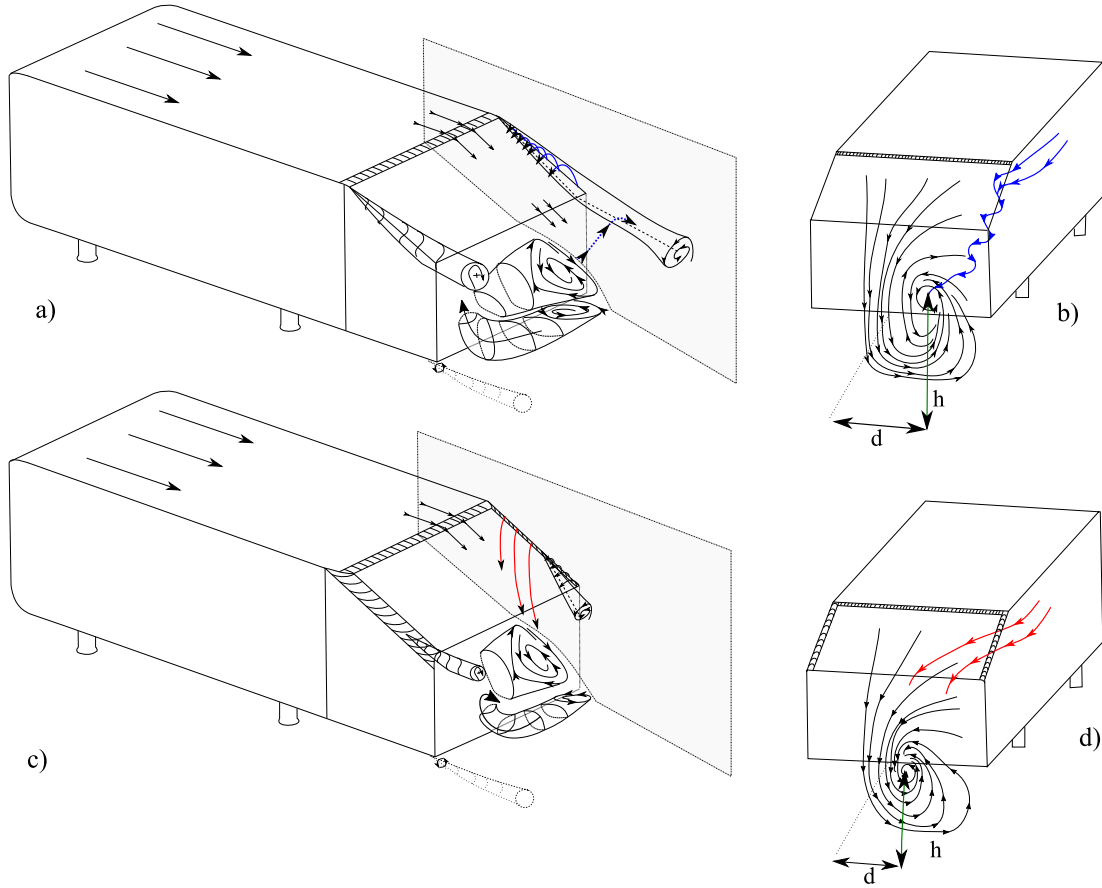


Figure 3.38: Schematic model of the flow structure around $R_{10}S_0$ (a,b) and $R_{10}S_{10}$ (c, d)

3.3 Towards a realistic model

The Ahmed body has proven to be an interesting choice to study the effect of afterbody rounding on the aerodynamics forces. The experimental data allowed to qualify and quantify the changing of the near wake due to the shape modification. But, what was understood with the Ahmed body, has to be confirmed now over realistic model featuring a true forebody and bigger afterbody edge radii. Such important radii are the more ad more used by the stylist departments and represents a real challenge for the vehicle aerodynamics. That's what will be presented in the next section. A stylistic model, issued from the direct collaboration with the PSA style department, will be tested to study drag and crosswind sensitivity over rounded fastback vehicle.

Regarding the value of the side radius, it was shown that sharp side pillar forces the separation and the consequent generation of the pillar vortex. It was underlines as well that with a small side rounding, $R_{10}S_{10}$, the C-pillar vortex origin was displaced and its intensity reduced. But this is an intermediate situation between the presence of the C-pillar vortex and its total disappearance and it will be taken into account in the choice of the realist model radii. To give an example of its total disappearance, one can refer to the water visualizations performed in the framework of the 2nd year project of Romano and Romani [68].

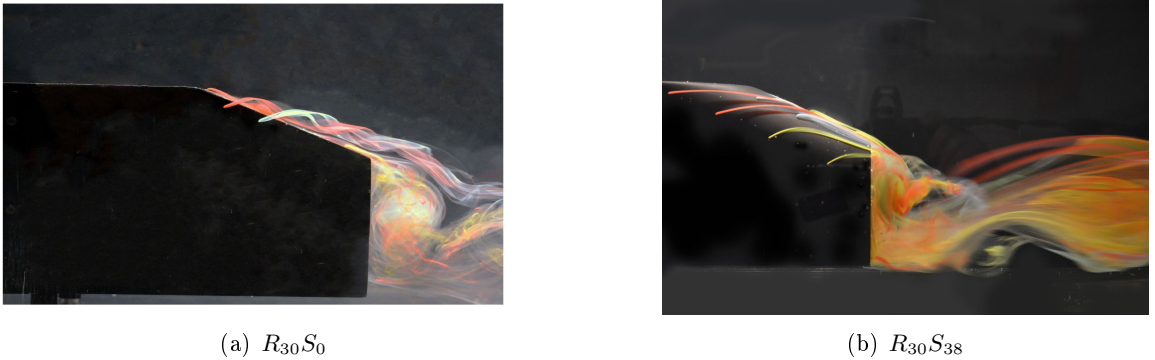


Figure 3.39: Water tunnel visualizations. [68]

The photos reported in *figures 3.39* are qualitative visualizations of the flow organization around the side pillars. In this study, the value of the rounded model side radius was 38%, so quite more important than in the Ahmed model cases previously described. Now, the rounded edge lets all the flow to overcome the side pillar, the C-pillar vortex has completely disappeared. Water channel visualizations underlined the side flow organization (*figure 3.39*). All the color filaments from the side of the rounded model are injected directly in the near wake (*figure 3.39(b)*) while for the sharp side model they are gathered inside the C-pillar vortex (*figure 3.39(a)*).

Another qualitative visualization of the effects of strong pillar radius is reported in *figure 3.40*. This model, similar to the Windsor model, was tested, numerically and experimentally, by the students during ENSMA projects. For this configuration, the C-pillar vortex is completely eliminated and

the longitudinal rotation of the flow it is so close to the model that its pressure foot-print is clearly noticeable over the model base. The streamlines are colored by the pressure coefficient. The longitudinal rotation is intense and should not be confused with the C-pillar vortex.

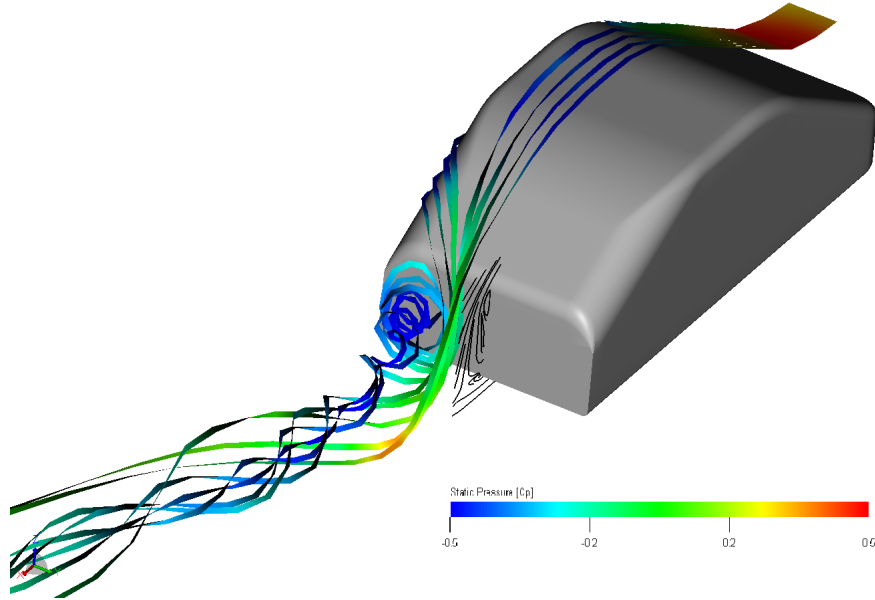


Figure 3.40: Numerical *PowerFlow* streamlines over a simplified vehicle model with important side pillars radius

Chapter 4

Effects of progressive afterbody rounding on the realistic shape vehicle

This chapter is confidential until 07 September 2019.

Part of this chapter has been published in "Aerodynamic performances of rounded fastback vehicle".
Proceedings of the Institution of Mechanical Engineers, Part D: Journal of Automobile Engineering
(Article 2 of appendix C)

Chapter 5

Conclusion and outlook

5.1 General synthesis

For the last decades car manufacturers have been facing the challenging task of reducing fuel consumption and CO₂ emissions. In response to that, optimization processes have been applied to generate new vehicle shapes minimizing the aerodynamic drag. Since the obtained optimal shapes have no brand differentiating details, stylists are nowadays trying to give back a brand signature by proposing "non-conventional" shapes characterized by important rear pillars rounding.

The present PhD work experimentally quantified the influence of such afterbody rounding on the aerodynamic loads and on the flow field development over fastback vehicle models.

Wind tunnel experiments were performed using 1:4 scaled models with the use of a 6 axes aerodynamic balance, wall pressure measurements, oil flow visualizations and Particle Image Velocimetry (2D-2C and 2D-3C). Numerical simulations were computed with *PowerFLOW*, the Lattice Boltzmann methods Exa solver, to help selecting the experimental Ahmed models and to complete the understanding of the flow field modifications due to afterbody rounding for both the Ahmed model and the realistic model called "Crosshatch". Three different scaled models were used, their complexity evolved gradually towards a realistic vehicle shape. Experimental tests were performed as well on a full scale vehicle over a Citroën C5.

At first, the well-known Ahmed body was used to investigate the change of pressure distribution due to end of the roof and side pillars rounding. Rounding the roof/backlight intersection was shown to reduce drag up to 16%. Surprisingly, additional rear curvature associated with side pillars rounding did not further modify the drag. However, the zero net effect was found to result from opposite drag effects on the slanted and vertical surfaces hiding local modifications in the flow field. The tridimensional organization and vorticity transport in the near wake were analyzed and connected to the observed local increase in base pressure drag.

The analyzes of the side rounding over the Ahmed body were published in Rossitto et al. [128].

In a second step, the complexity of the experimental model used was increased by using a realistic fastback simplified vehicle with rounded side pillars. The curvature radius completely eliminated the longitudinal vortices and drastically changed the flow organization of the near wake. Comparison with sharp edges showed again how the impact on drag is minimal despite an important lift

reduction. These results were reported in the *Appendix 1*. The similarity of the flow field behavior between the Ahmed body and the realistic model was presented in Rossitto et al. [143].

To further increase the fidelity of the model, especially in what concerns the cabin rear habitability, a third model was realized in partnership with the style department of PSA. Four different side radii were tested. Crosswind sensitivity was also investigated by means of yaw angle variation. It was shown that the rear ends with rounded edges deteriorate the lateral aerodynamics resulting in an increase of rear lift and yawing moment.

The use of passive devices (variable rounding pillars, spoilers and diffuser) was proposed and tested to improve the vehicle aerodynamics reducing the negative effects induced by side pillar rounding. These results are submitted for publication in [144]

The understanding of the afterbody rounding effects was shown to be valid despite the increasing complexity of the models. Finally, full scale test confirmed the trends observed over the scaled models.

5.2 Perspectives

This work provides some guidelines to improve vehicles design and flow control strategies by revealing candidate zones for drag and lift reduction as well as for yawing moment reduction.

It was highlighted the interesting mechanism of compensation between positive and negative effects for drag reduction due to afterbody rounding at zero yaw angle over the slanted surface and the base. A solution could be found in a right choice of the ratio between the base and the slanted surface, for a fix side radius, to be able to manage the desired drag balance. This ratio will be dependent of course on the slant angle.

In the past literature the C-pillar vortices were (and always be) considered as negative effect for drag and rear lift. Nevertheless, the positive effects of gathering the side flow avoiding strong downwash in the near wake has never be mentioned to the best of the author knowledge. To have an optimal near wake flow, the two counter-rotating structures have to be as much farther from the vertical base, corresponding to the case when the counter-rotating structures have almost the same size and position. Unfortunately, this is the case where the C-pillar vortices are presents and generate drag and lift increase over the rear slant.

A strategy that could permit to keep sharp rear pillars while reducing the C-pillar vortices intensity is to reduce the traversal gradient across the edge. Han and Kim [145] propose to align the sharp edges to follow the external streamlines and therefore reduce pressure gradients in the transverse direction. This concept was proven to reduce drag over a simplified vehicle shape when the rear deck and the rear fender was realigned to avoid vortex formation.

The evolution of the vehicle style is towards vehicle with rounded side pillars. At zero yaw angle the use of a small spoiler at the end of the rear slant could therefore improve the near wake flow organization (i.e. elimination of the downwash) resulting in optimal aerodynamic performances for such pillars geometry.

Unfortunately, the rounded side pillars deteriorate the lateral aerodynamics. Variable side pillars radius was proven to be a good intuition in what concerns the improving of the aerodynamic per-

formances. This strategy underlined the need of different optimal side radius according to the environmental condition. The best solution for aerodynamic improvement of a fastback rear end, will be then to have rounded rear pillars at zero yaw angle (coupled with a rear spoiler at the end of the roof) whereas, at high angle of yaw, sharp side pillars to reduce rear lift and yawing moment. A self adaptive pillar radius could be imagined for future vehicles. Equipped with pressure sensors, the future vehicle will be able to understand in real time the direction of the wind impacting the vehicle [146]. The future side pillars should be able to automatically adjust their radius to become sharp to improve the lateral stability and to come back to the rounded configuration once the wind approaching the vehicle will be again parallel to the motion.

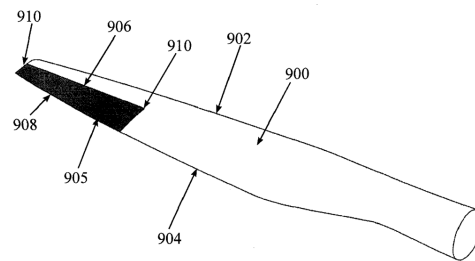


Figure 5.1: Details of patent EP 2423104A1

Many patents can be mentioned from different car manufactures to underline the high interest regarding variable vehicle shape. Historically, self adaptive passive surfaces are actually well known in aeronautics to improve the wing performances [147]. The idea is to have a mobile surface (reported in black in *figure 5.1*) that is deployed actively or passively according to the pressure acting over the wing.

This concept, as report in left side of *figure 5.2*, was successfully applied over NASCAR vehicles to reduce lift off during spinning at high speed [148].

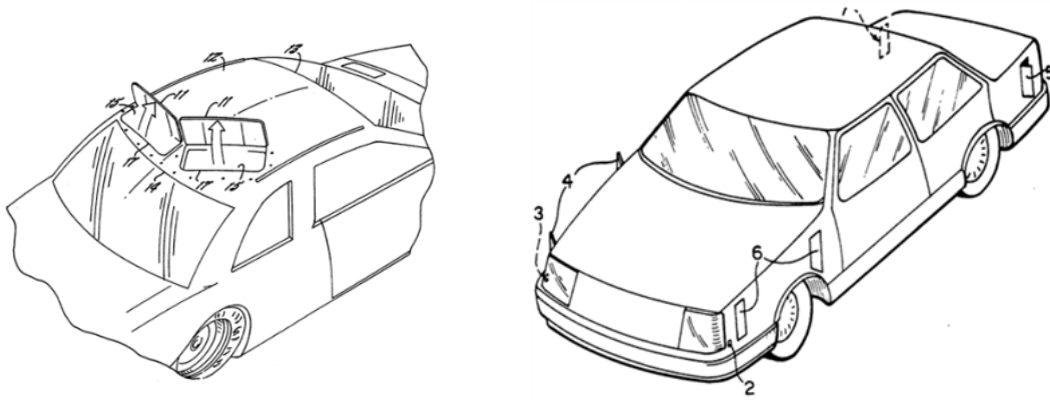


Figure 5.2: Details of patents. Left: US5374098, right: IT8767106

Regarding the use of active surface, [149] propose a system of active deflectors over the vehicle body to improve the vehicle performance in crosswind. These deflectors are open to reduce the yawing moment and they are placed on the lower sides of the vehicles (right side of *figure 5.2*).

Instead of using “additional surfaces”, [150] proposes to change the overall shape of the vehicles thanks to the use of internal actuators (left side of *figure 5.3*). The exterior surfaces must be made in flexible materials. This concept can be applied “to create” spoilers or lateral deflectors when needed. A direct application of flexible surface to the C-pillar can be found in [151] as reported in right side of *figure 5.3*. A system of flexible surface is inflated according to the driving condition to alter the shape of the vehicle C-pillars.

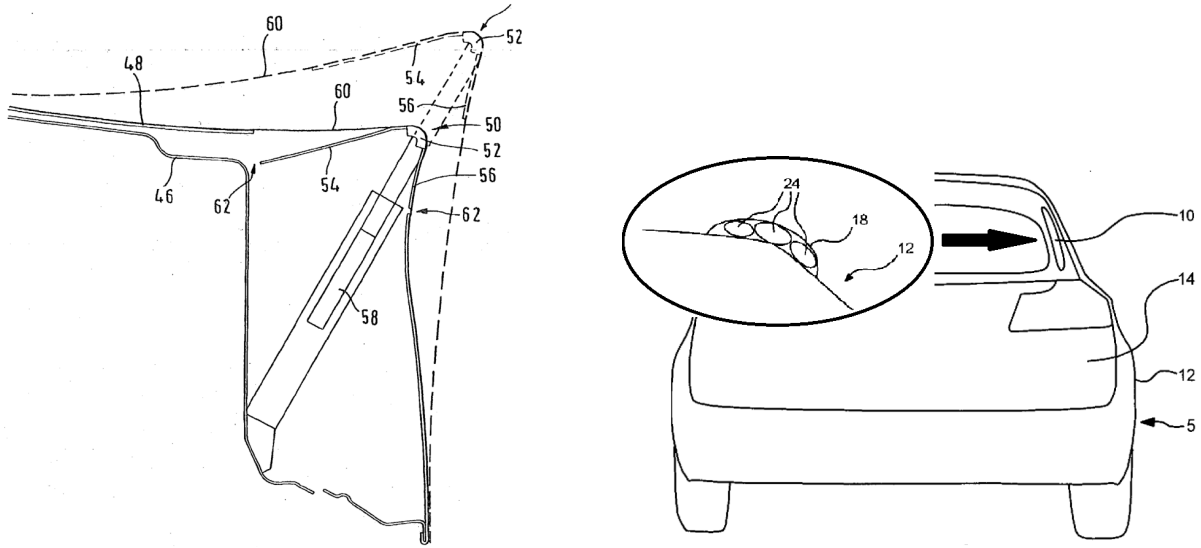


Figure 5.3: Details of patents. Left: US 2004/0130182 A1, right: DE102011121909A1

The aerodynamic performances of the vehicle C-pillars can be modified also by the use of cylinders inside the pillars as proposed in the patent of [152] and reported in *figure 5.4*. The rotation of the cylinders is used here to control the flow overcoming the edge and to prevent the origin the C-pillar vortices.

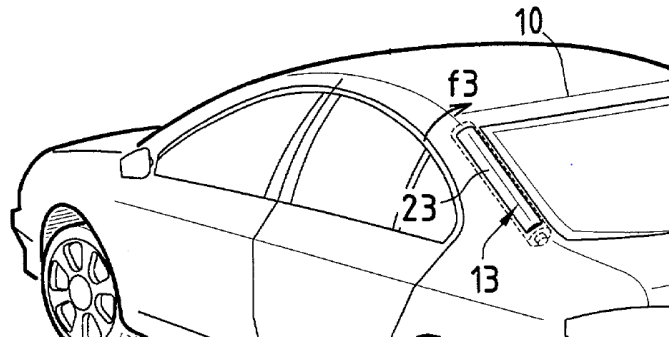


Figure 5.4: Details of patent FR 2854858

An interesting alternative solution to optimize the aerodynamic of the side rear pillars was patented in 2016 by Aston Martin in [153] (*figure 5.5*). The side pillars of the new DB11 model feature an important radius. To avoid the flow to overcome the pillars, the flow is blown directly at the beginning of the pillars and, by means of an internal duct, is injected at the end of the roof creating a “virtual spoiler” [153]. This solution seems to improve all the driving conditions of the vehicle acting directly on the elimination of the C-pillar vortices.

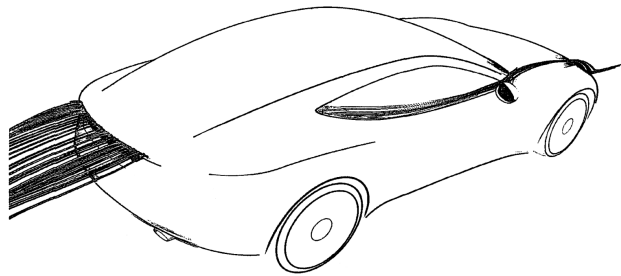


Figure 5.5: Details of patent WO201659402A2

As reported in the introduction of this PhD works, the reduction of fuel consumption has become a main objective for the automotive industry since 1973. Most of the patents reported above have less than 20 years.

Research should lead the new ideas of flow control bringing more comprehension of the physics flow field around the vehicles.

The attention should be focused on the global flow modifications induced by passive or active control. Too many times strategies of local flow control have been studied and analyzed with only a local view of the effects on the flow field.

In this work was highlighted that both the local and the global flow modifications are important to evaluate the vehicles aerodynamics. Moreover the coupling between the near and far wake is not yet completely understood.

The new forms of flow control should also take into account that the structures of the near wake have a proper dynamics that drive and modify the entire wake. Beyond classical wake survey analysis to study the entire wake properties, it has also been shown that the understanding of the vorticity dynamics is very important to describe the global wake structures dynamics. This methodology should be applied widely to understand the development of complex 3D wakes.

Appendix A

Wind tunnel test over a scaled simplified Citroën C4

In this Appendix the experimental results over the scaled Citroën C4 are reported. Those test were performed between the Ahmed model and the Crosshatch. They permitted to verify the physical comprehension achieved of the effects of afterbody rounding over a model featuring a realistic forebody. The Crosshatch was chosen after those results to go further in the investigation over a “style model” to complete the study with crosswind sensitivity and passive flow control.

Table A.1 reports the variation of the drag and lift coefficients for the rounded rear end compared with the sharp one, (the value of drag and lift are not reported because they are meaningless since this model is a unique prototype). As an order of magnitude, the drag coefficient of the sharp rear end is 35% less than the reference Ahmed body. The rounded configuration exhibits a slight increase in drag. As for the Ahmed body, this hides major local flow modifications. On the contrary, lift is strongly reduced, which demonstrates the influence of the rounded edge on the C-pillar.

| | ΔC_d | ΔC_l |
|----------------|--------------|--------------|
| <i>Sharp</i> | - | - |
| <i>Rounded</i> | +1.5% | -8.5% |

Table A.1: Variation of aerodynamic coefficients relative to the sharp case.

When comparing with the Ahmed body presented in *Chapter 3*, similar oil flow visualization interpretations were made for the realistic model in *figure A.1*. The sharp configuration, reported on the left side of the picture, clearly demonstrates the presence of a C-pillar vortex. For the rounded configuration, the large curvature does not even generate a delayed C-pillar vortex; all the flow that comes from the side of the model, in fact, enters the rear window region through an inward transverse attached flow.

Figure A.2 highlights the pressure wall measurements over the rear ends. Due to the complexity of the side surface of the model, as for example a realistic gap between the window and the side

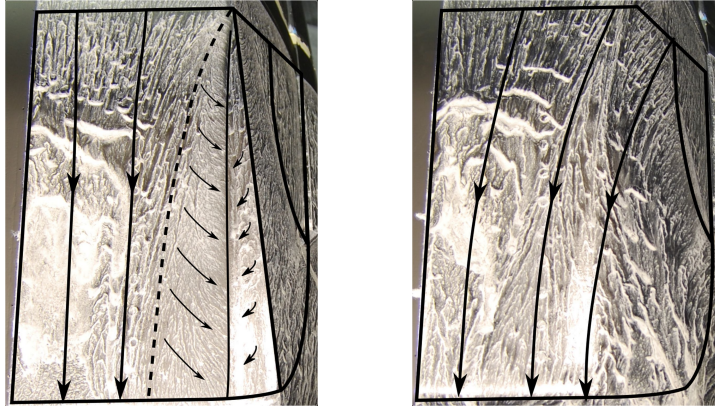


Figure A.1: Oil visualization. Left: Sharp rear end. Right: Rounded rear end. Dashed line is the attachment line of the primary vortex, solid line is the separation line of the secondary vortex. Long arrows indicate the overall direction of the flow off the surface.

surface of the model, the C-pillar vortex pressure footprint is less intense than the modified Ahmed body, but still present in the sharp case. The pressure distributions on the side of the rounded edge rear end confirm the absence of the C-pillar vortex. As with the modified Ahmed body, the vertical surface displays a lower pressure coefficient than for the sharp case *tab A.2*. For the Ahmed body, the loss of pressure on the vertical surface compensates for the gain over the rear window when a rounded edge is present. This is not the case for the realistic model, where the net balance between the loss and the gain is not zero ($\Delta C_d = +1.5\%$, see *table A.1*). This underlines the generic nature of the positive and negative effects over the two zones of the rear end, but points out that every model has its own ratio between the vertical surface and the rear window, which influences drag balance [131].

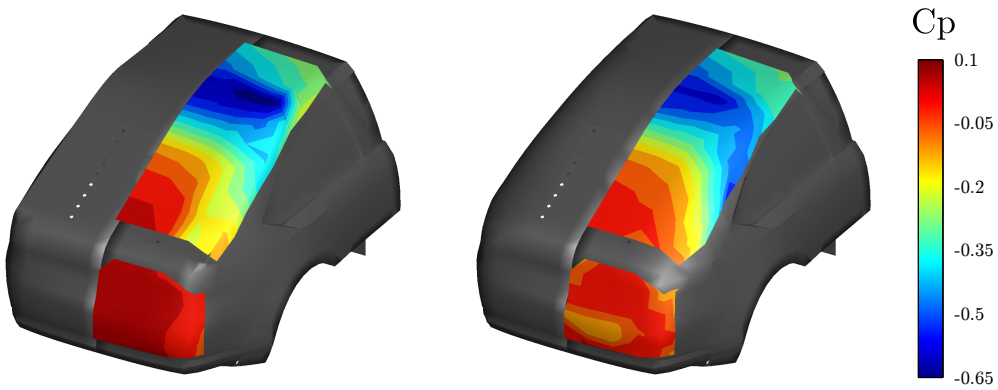


Figure A.2: Wall pressure coefficient C_p : Left Sharp, Right Rounded.

| | Rear window ΔC_p | Vertical surface ΔC_p |
|----------------|--------------------------|-------------------------------|
| <i>Sharp</i> | - | - |
| <i>Rounded</i> | +10% | -300% |

Table A.2: Variation of spatially averaged mean C_p over the rear window and vertical surface relative to the sharp case.

PIV was also performed in the symmetry plane of the model *figure A.3*. It is noticed that C-pillar rounding induces important modifications in the near wake. When rounding the C-pillar the length of the separated region is strongly reduced and not any counter rotating structures are noticed anymore. As described in *Chapter 3 and 4*, the flow overcoming the edge results in an important downwash as reported in *figure A.4*.

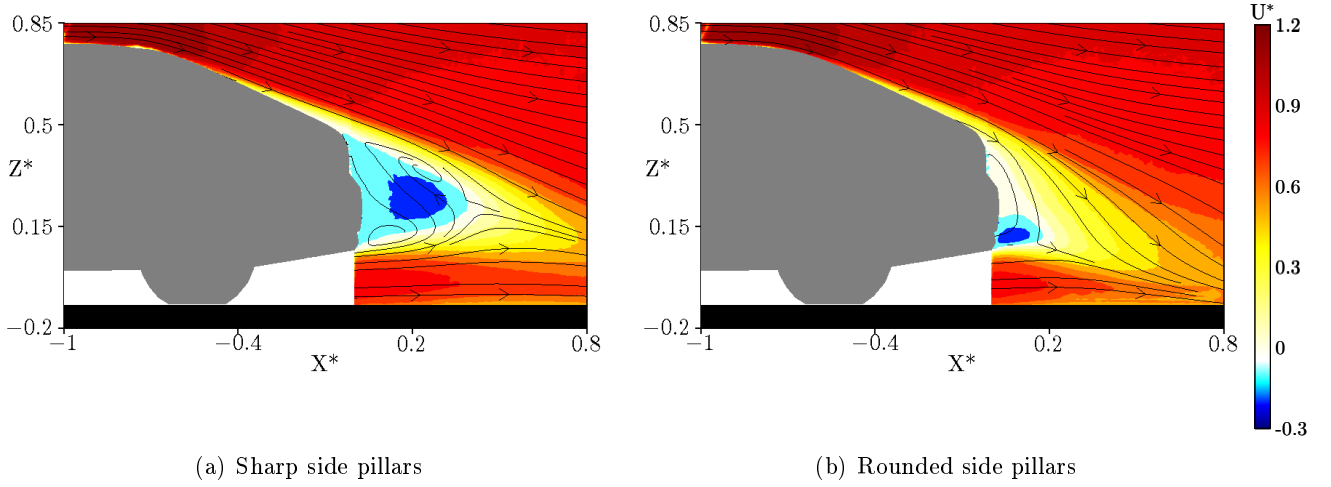


Figure A.3: Streamwise Velocity U^* at $Y^*=0$.

YZ Stereo-PIV planes are reported in *figure A.5* at $X^*=0.07$. *Figure A.5(a)* evidences the presence of the C-pillar vortex in the sharp case due its characteristic streamwise velocity contours, no sign of C-pillar vortex is visible on the right side of the picture for the rounded model. Around $Y^* \approx \pm 0.2$ and $Z^* \approx 0.6$ in both models the so called A-pillars is visible. The spanwise velocity is reported in *figure A.5(b)*. While for the sharp rear end there are two opposite regions of localized transverse velocity due to the C-pillar vortex, for the rounded edge model, only an intense region of lateral flow that comes from the side (and is injected in the near wake) is present. The resulting downwash is clearly visible in the right side of *figure A.5(c)*. Contours of Γ_2 in *figure A.5(d)* illustrate the global streamwise rotation of the flow, expected to induce a low pressure region over the vertical base of the vehicle.

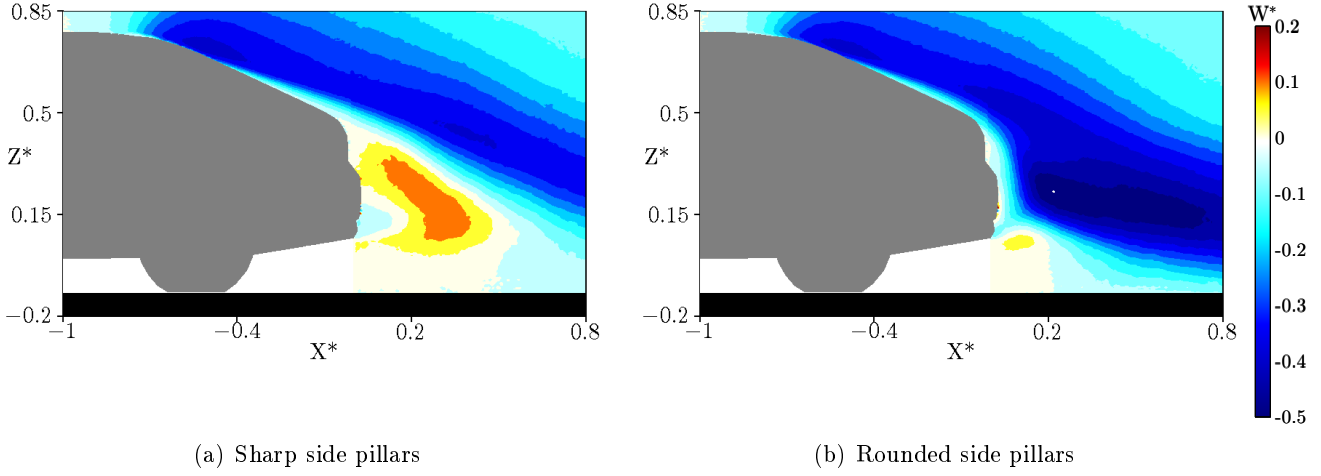


Figure A.4: Normal Velocity W^* at $Y^* = 0$.

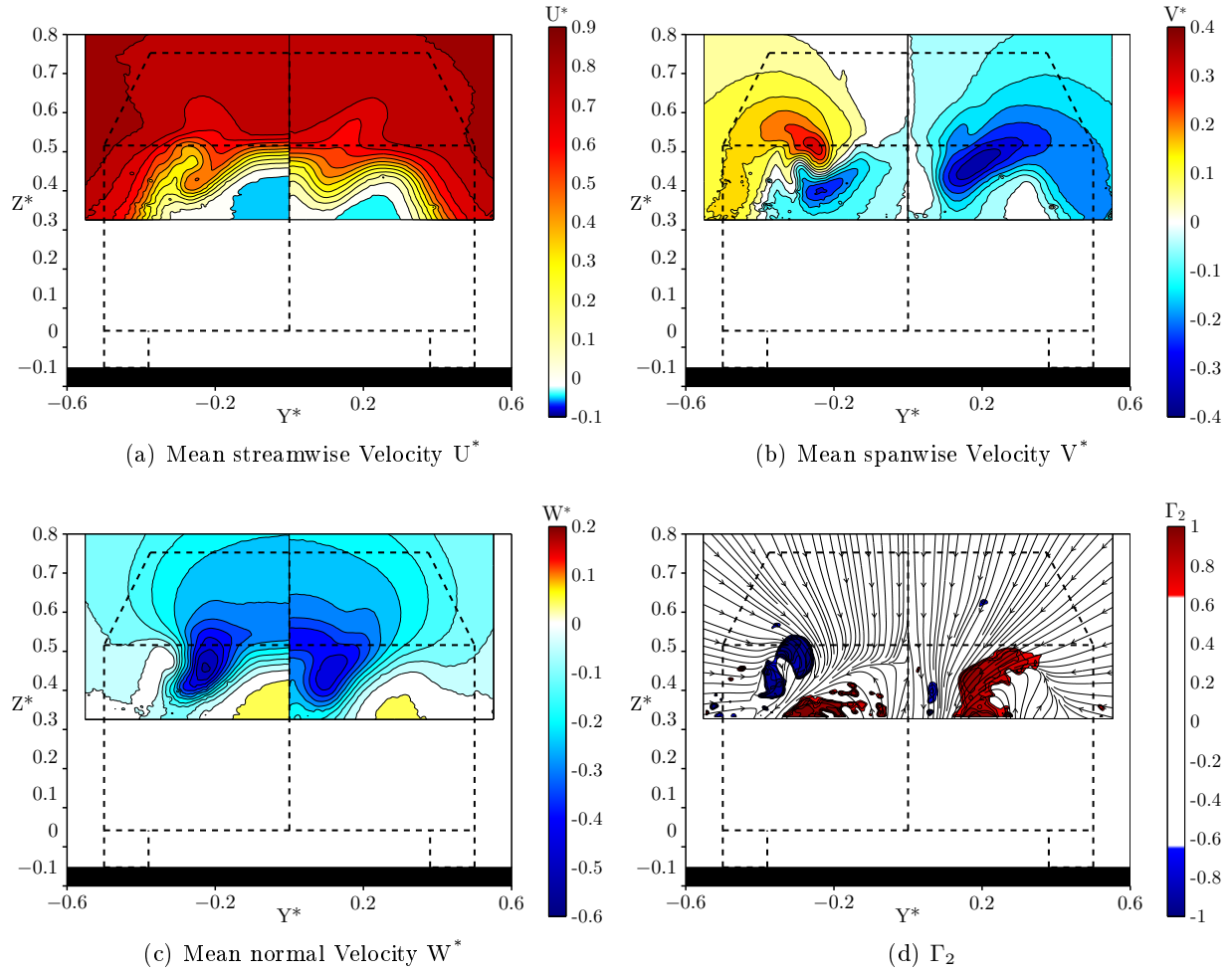


Figure A.5: Plane at $X^* = 0.07$. The dashed lines represent the geometry of the model.

Appendix B

Full scale wind tunnel test over a Citroën C5

This chapter is confidential until 07 September 2019.

Bibliography

- [1] Kevin A Baumert, Timothy Herzog, and Jonathan Pershing. *Navigating the numbers: Greenhouse gas data and international climate policy*. World Resources Inst, 2005.
- [2] Robert J Nicholls. Case study on sea-level rise impacts. In *OECD Workshop on the Benefits of Climate Policy: Improving Information for Policy Makers. Dokument ENV/EPOC/GSP (2003)*, 2003.
- [3] Derek S Arndt, Molly O Baringer, Michael R Johnson, LV Alexander, HJ Diamond, RL Fogt, JM Levy, J Richter-Menge, PW Thorne, LA Vincent, et al. State of the climate in 2009. *Bulletin of the American Meteorological Society*, 91(7), 2010.
- [4] Nell Greenfieldboyce. Study: 634 million people at risk from rising seas. 2007.
- [5] European Commission. Reducing co₂ emission from passenger cars. http://ec.europa.eu/clima/policies/transport/index_en.htm, 2010.
- [6] Monitoring co₂ emissions from passenger cars and vans in 2013. Technical report, EEA Technical report, 2014.
- [7] Europe 2014: Sales results insights. Technical report, NON-OFFICIAL site for Fiat Chrysler Automobiles world wide trends, market research and data analysis, 2014.
- [8] Philippe Ricard. Echec des européens en vue de réduire la pollution automobile. *Le Monde*, 2013.
- [9] Jean-Jacques Mevel. Co₂ des voitures : Berlin défend ses grosses cylindrées et marque des points. *Le Figaro*, 2013.
- [10] Laurent Elena. Aérodynamique automobile. *Mécanique & industries*, 2(3):199–210, 2001.
- [11] F. Muyl, V. Herbert, and L. Dumas. Réduction des émissions de co₂: optimisation de la traînée aérodynamique automobile par algorithmes hybrides, 2003.
- [12] Cedric Leclerc. *Reduction de la traînée d'un véhicule automobile simplifié à l'aide du contrôle actif par jet synthétique*. PhD thesis, L'Institut National Polytechnique de toulouse, 2008.
- [13] Yvonnick Gazeau. L'importance de l'aérodynamique pour l'automobile. *web auto*.
- [14] Y Wang, Y Xin, Zh Gu, Sh Wang, Y Deng, and X Yang. Numerical and experimental investigations on the aerodynamic characteristic of three typical passenger vehicles. *Journal of Applied Fluid Mechanics*, 7(4):659–671, 2014.
- [15] Lennert Sterken. Analysis of the base wake on passenger vehicles. *Chalmers University of Technology*, 2013.
- [16] Wolf-Heinrich Hucho. *Aerodynamics of Road Vehicles*. SAE international, fourth edition, 1998.
- [17] Wolfgang Mayer and Gerhard Wickern. The new audi a6/a7 family-aerodynamic development of different body types on one platform. *SAE International Journal of Passenger Cars-Mechanical Systems*, 4(1):197–206, 2011.
- [18] Robert Palin, Vincent Johnston, Shaun Johnson, Andrew D'Hooge, Bradley Duncan, and Joaquin Ivan Gargoloff. The aerodynamic development of the tesla model s-part 1: Overview. Technical report, SAE Technical Paper, 2012.

- [19] Mark Bannister. Drag and dirt deposition mechanisms of external rear view mirrors and techniques used for optimisation. Technical report, SAE Technical Paper, 2000.
- [20] Alexey Vdovin. Investigation of aerodynamic resistance of rotating wheels on passenger cars. *Chalmers University of Technology*, 2013.
- [21] Andrew D’Hooge, Robert B Palin, S Johnson, Bradley Duncan, and Joaquin Ivan Gargoloff. The aerodynamic development of the tesla model s-part 2: Wheel design optimization. Technical report, SAE Technical Paper, 2012.
- [22] Hitoshi Fukuda, Kazuo Yanagimoto, Hiroshi China, and Kunio Nakagawa. Improvement of vehicle aerodynamics by wake control. *JSAE review*, 16(2):151–155, 1995.
- [23] Joseph Katz. *Race Car Aerodynamics: Designing for Speed (Engineering and Performance)*. Bentley Publishers, 1995.
- [24] Wolf-Heinrich Hucho and Gino Sovran. Aerodynamics of road vehicles. *Annual review of fluid mechanics*, 25(1):485–537, 1993.
- [25] Geoffrey M Le Good and Kevin P Garry. On the use of reference models in automotive aerodynamics. Technical report, SAE Technical Paper, 2004.
- [26] SR Ahmed, G Ramm, and G Faitin. Some salient features of the time-averaged ground vehicle wake. Technical report, Society of Automotive Engineers, Inc., Warrendale, PA, 1984.
- [27] PW Bearman. Some observations on road vehicle wakes. Technical report, Society of Automotive Engineers, Inc., Warrendale, PA, 1984.
- [28] M. Onorato, AF Costelli, and A. Garrone. Drag measurement through wake analysis. Technical report, Society of Automotive Engineers, Inc., Warrendale, PA, 1984.
- [29] JE Hackett and A Sugavanam. Evaluation of a complete wake integral for the drag of a car-like shape. Technical report, SAE Technical Paper, 1984.
- [30] Gino Sovran. The effect of ambient wind on a road vehicle’s aerodynamic work requirement and fuel consumption. Technical report, Society of Automotive Engineers, Inc., Warrendale, PA, 1984.
- [31] Frank T Buckley and William S Sekscienski. Comparisons of effectiveness of commercially available devices for the reduction of aerodynamic drag on tractor-trailers. Technical report, SAE Technical Paper, 1975.
- [32] R Buchheim, K-R Deutenbach, and H-J Lückoff. Necessity and premises for reducing the aerodynamic drag of future passenger cars. Technical report, SAE Technical Paper, 1981.
- [33] Two small steps toward the low-drag car. *New Scientist*, 95(1324), 1982.
- [34] Saab history. <http://www.saabhistory.com/>.
- [35] Sandersonm Paul. Why do all new cars look alike?, March 2012.
- [36] Oceane Redon. Le design doit traduire des valeurs. *Strategies : Marketing Communication Medias*, (1783), 2014.
- [37] Diese frau ist der albtraum der auto-designer. *Die Welt*, 2016.
- [38] JC Hu, Y Zhou, and C Dalton. Effects of the corner radius on the near wake of a square prism. *Experiments in Fluids*, 40(1):106–118, 2006.
- [39] PW Bearman, JMR Graham, ED Obasaju, and GM Drossopoulos. The influence of corner radius on the forces experienced by cylindrical bluff bodies in oscillatory flow. *Applied Ocean Research*, 6(2):83–89, 1984.
- [40] Shiki Okamoto and Naoto Uemura. Effect of rounding side-corners on aerodynamic forces and turbulent wake of a cube placed on a ground plane. *Experiments in Fluids*, 11(1):58–64, 1991.

-
- [41] Tetsuro Tamura and Tetsuya Miyagi. The effect of turbulence on aerodynamic forces on a square cylinder with various corner shapes. *Journal of Wind Engineering and Industrial Aerodynamics*, 83(1):135–145, 1999.
 - [42] Guido Buresti, Roberto Fedeli, and Andrea Ferraresi. Influence of afterbody rounding on the pressure drag of an axisymmetrical bluff body. *Journal of Wind Engineering and Industrial Aerodynamics*, 69:179–188, 1997.
 - [43] Alessandro Mariotti and Guido Buresti. Experimental investigation on the influence of boundary layer thickness on the base pressure and near-wake flow features of an axisymmetric blunt-based body. *Experiments in fluids*, 54(11):1–16, 2013.
 - [44] Dietrich J Hummel. The international vortex flow experiment 2 (vfe-2): background, objectives and organization. *Aerospace Science and Technology*, 24(1):1–9, 2013.
 - [45] James M Luckring. Initial experiments and analysis of blunt-edge vortex flows for vfe-2 configurations at nasa langley, usa. *Aerospace Science and Technology*, 24(1):10–21, 2013.
 - [46] Shabudin Mat, IS Ishak, Tholudin Mat Lazim, Shuhaimi Mansor, Mazuriah Said, Abdul Basid Abdul Rahman, Ahmad Shukeri Mohd Kamaludim, and Romain Brossay. Development of delta wing aerodynamics research in universiti teknologi malaysia low speed wind tunnel. *Advances in Mechanical Engineering*, 6:434892, 2014.
 - [47] R Buchheim, B Leie, and HJ Lückoff. Der neue audi 100—ein beispiel für konsequente aerodynamische personenwagen-entwicklung. *ATZ*, 85:419–425, 1983.
 - [48] Alfons M Gilhaus and Volker E Renn. Drag and driving-stability-related aerodynamic forces and their interdependence—results of measurements on 3/8-scale basic car shapes. Technical report, SAE Technical Paper, 1986.
 - [49] JP Howell. C466/036 shape features which influence crosswind sensitivity. 9(1):43–43, 1993.
 - [50] Adrien Thacker, S Aubrun, A Leroy, and Philippe Devinant. Effects of suppressing the 3d separation on the rear slant on the flow structures around an ahmed body. *Journal of Wind Engineering and Industrial Aerodynamics*, 107:237–243, 2012.
 - [51] John P Davis. *Wind tunnel investigations of road vehicle wakes*. PhD thesis, Imperial College London (University of London), 1982.
 - [52] Joshua Fuller and Martin A Passmore. The importance of rear pillar geometry on fastback wake structures. *Journal of Wind Engineering and Industrial Aerodynamics*, 125:111–120, 2014.
 - [53] Jermann Cyril. *Eclatement tourbillonnaire dans le sillage turbulent d’un véhicule générique*. PhD thesis, Aix-marseille université, 2005.
 - [54] Gregory Pujals. *Perturbations optimales dans les écoulements de paroi turbulents et application au contrôle de décollement*. PhD thesis, Palaiseau, Ecole polytechnique, 2009.
 - [55] Jean-François Beaudoin. *Contrôle actif d’écoulement en aérodynamique automobile*. PhD thesis, Paris, ENMP, 2004.
 - [56] D. Barros. *Wake and Drag Manipulation of a Bluff Body Using Fluidic Forcing*. PhD thesis, Chasseneuil-du-Poitou, Ecole nationale supérieure de mécanique et d’aérotechnique, 2015.
 - [57] Mathieu Grandemange. *Analysis and control of three-dimensional turbulent wakes: from axisymmetric bodies to road vehicles*. PhD thesis, Palaiseau, Ecole polytechnique, 2013.
 - [58] Pierric Joseph. *Application du contrôle par jets pulsés à un corps non profilé*. PhD thesis, Université Pierre et Marie Curie-Paris VI, 2012.
 - [59] Eric Serre, Matthieu Minguez, Richard Pasquetti, Emmanuel Guilmineau, Gan Bo Deng, Michael Kornhaas, Michael Schäfer, Jochen Fröhlich, Christof Hinterberger, and Wolfgang Rodi. On simulating the turbulent flow around the ahmed body: A french–german collaborative evaluation of les and des. *Computers & Fluids*, 78:10–23, 2013.

- [60] Emmanuel Guilmineau, GanBo Deng, and Jeroen Wackers. Numerical simulation with a des approach for automotive flows. *Journal of Fluids and Structures*, 27(5):807–816, 2011.
- [61] Emmanuel Guilmineau. Computational study of flow around a simplified car body. *Journal of wind engineering and industrial aerodynamics*, 96(6):1207–1217, 2008.
- [62] J Venning, D Lo Jacono, D Burton, M Thompson, and J Sheridan. The effect of aspect ratio on the wake of the ahmed body. *Experiments in Fluids*, 56(6):1–11, 2015.
- [63] S Balachandar, R Mittal, and FM Najjar. Properties of the mean recirculation region in the wakes of two-dimensional bluff bodies. *Journal of Fluid Mechanics*, 351:167–199, 1997.
- [64] Alessandro Mariotti, Guido Buresti, and Maria Vittoria Salvetti. On the influence of boundary layer thickness on the base drag and on the near-wake flow of an axisymmetric blunt-based body. 2012.
- [65] Vladimir Parezanović and Olivier Cadot. Experimental sensitivity analysis of the global properties of a two-dimensional turbulent wake. *Journal of Fluid Mechanics*, 693:115–149, 2012.
- [66] Sinisa Krajnović, D Barros, T Ruiz, J Borée, and B Noack. Control of a three-dimensional blunt body wake using low and high frequency pulsed jets. *International Journal of Flow Control*, 6(1):61–74, 2014.
- [67] Patrick Gilliéron and Francis Chometon. Modelling of stationary three-dimensional separated air flows around an ahmed reference model. In *ESAIM: Proceedings*, volume 7, pages 173–182. EDP Sciences, 1999.
- [68] Romano and Romani. 2nd year project. *2015, Supaero Graduate Program, ISAE*, 2015.
- [69] A Spohn and P Gilliéron. Flow separations generated by a simplified geometry of an automotive vehicle, iutam symp. *Unsteady Separated Flows*, 2002.
- [70] G Vio, S Watkins, P Mousley, J Watmuff, and S Prasad. Flow structures in the near-wake of the ahmed model. *Journal of fluids and structures*, 20(5):673–695, 2005.
- [71] Sinisa Krajnović and Lars Davidson. Flow around a simplified car, part 2: understanding the flow. *Journal of Fluids Engineering*, 127(5):919–928, 2005.
- [72] M Minguez, R Pasquetti, and E Serre. High-order large-eddy simulation of flow over the "ahmed body" car model. *Physics of Fluids (1994-present)*, 20(9):095101, 2008.
- [73] David B Sims-Williams and Bradley D Duncan. The ahmed model unsteady wake: Experimental and computational analyses. *SAE transactions*, 112(6):1385–1396, 2003.
- [74] Bradley D Duncan, Raja Sengupta, Swapan Mallick, Rick Shock, and DB Sims-Williams. Numerical simulation and spectral analysis of pressure fluctuations in vehicle aerodynamic noise generation. Technical report, SAE Technical Paper, 2002.
- [75] H. Lienhart, C. Stoots, and S. Becker. Flow and turbulence structures in the wake of a simplified car model (ahmed model). 2007.
- [76] Adrien Thacker, Sandrine Aubrun, Annie Leroy, and Philippe Devinant. Experimental characterization of flow unsteadiness in the centerline plane of an ahmed body rear slant. *Experiments in fluids*, 54(3):1–16, 2013.
- [77] XW Wang, Y Zhou, YF Pin, and TL Chan. Turbulent near wake of an ahmed vehicle model. *Experiments in fluids*, 54(4):1–19, 2013.
- [78] JF Beaudoin and JL Aider. Drag and lift reduction of a 3d bluff body using flaps. *Experiments in fluids*, 44(4):491–501, 2008.
- [79] Grégoire Fourrié, Laurent Keirsbulck, Larbi Labraga, and Patrick Gilliéron. Bluff-body drag reduction using a deflector. *Experiments in Fluids*, 50(2):385–395, 2011.
- [80] Wang Hanfeng, Zhou Yu, Zou Chao, and He Xuhui. Aerodynamic drag reduction of an ahmed body based on deflectors. *Journal of Wind Engineering and Industrial Aerodynamics*, 148:34–44, 2016.

-
- [81] J.L. Aider, J.F. Beaudoin, and J.E. Wesfreid. Drag and lift reduction of a 3d bluff-body using active vortex generators. *Experiments in fluids*, 48(5):771–789, 2010.
 - [82] G Pujals, S Depardon, and Carlo Cossu. Drag reduction of a 3d bluff body using coherent streamwise streaks. *Experiments in fluids*, 49(5):1085–1094, 2010.
 - [83] Patrick Gilliéron and Azeddine Kourta. Aerodynamic drag reduction by vertical splitter plates. *Experiments in fluids*, 48(1):1–16, 2010.
 - [84] Pierrick Joseph, Xavier Amandolèse, and Jean-Luc Aider. Drag reduction on the 25 slant angle ahmed reference body using pulsed jets. *Experiments in fluids*, 52(5):1169–1185, 2012.
 - [85] Sandrine Aubrun, Jonathan McNally, Farrukh Alvi, and Azeddine Kourta. Separation flow control on a generic ground vehicle using steady microjet arrays. *Experiments in fluids*, 51(5):1177–1187, 2011.
 - [86] Mathieu Rouméas, Patrick Gilliéron, and Azeddine Kourta. Separated flows around the rear window of a simplified car geometry. *Journal of Fluids Engineering*, 130(2):021101, 2008.
 - [87] Matthew Metka and James W Gregory. Drag reduction on the 25-deg ahmed model using fluidic oscillators. *Journal of Fluids Engineering*, 137(5):051108, 2015.
 - [88] Charles-Henri Bruneau, Emmanuel Creusé, Delphine Depeyras, Patrick Gilliéron, and Iraj Mortazavi. Active procedures to control the flow past the ahmed body with a 25 rear window. *International Journal of Aerodynamics*, 1(3-4):299–317, 2011.
 - [89] Benjamin Lehugeur, Patrick Gilliéron, and Tanja Ivanić. Contribution de l’éclatement tourbillonnaire à la réduction de la traînée des véhicules automobiles: approche numérique. *Comptes Rendus Mécanique*, 334(6):368–372, 2006.
 - [90] Bingfu Zhang. *The flow structure around an Ahmed vehicle model and its active control*. PhD thesis, The Hong Kong Polytechnic University, 2014.
 - [91] Haecheon Choi, Jungil Lee, and Hyungmin Park. Aerodynamics of heavy vehicles. *Annual Review of Fluid Mechanics*, 46:441–468, 2014.
 - [92] Jean-Luc Aider, JJ Lasserre, JF Beaudoin, Vincent Herbert, and J.E. Wesfreid. Contrôle d’écoulement en aérodynamique automobile. *Congrès Français de Mécanique*, 2009.
 - [93] Jean-Luc Aider, Pierrick Joseph, Tony Ruiz, Philippe Gilotte, Yoann Eulalie, Christophe Edouard, and Xavier Amandolèse. Active flow control using pulsed micro-jets on a full-scale production car. *International Journal of Flow Control*, 6(1):1–20, 2014.
 - [94] R Strachan, K Knowles, and N Lawson. Comparisons between cfd and experimental results for a simplified car model in wall proximity. In *2nd international symposium on integrating CFD and experiments in aerodynamics*, 2005.
 - [95] GS West and CJ Apelt. The effects of tunnel blockage and aspect ratio on the mean flow past a circular cylinder with reynolds numbers between 10 4 and 10 5. *Journal of Fluid Mechanics*, 114:361–377, 1982.
 - [96] Mathieu Grandemange, Axel Mary, Marc Gohlke, and Olivier Cadot. Effect on drag of the flow orientation at the base separation of a simplified blunt road vehicle. *Experiments in fluids*, 54(5):1–10, 2013.
 - [97] Marc Gohlke, Jean-François Beaudoin, Muriel Amielh, and Fabien Anselmet. Experimental analysis of flow structures and forces on a 3d-bluff-body in constant cross-wind. *Experiments in Fluids*, 43(4):579–594, 2007.
 - [98] A-Tech Instruments Ltd. 8400 scanner digitizer interface pressure scanner specifications. <http://www.a-tech.ca/series.php?tab=6>.
 - [99] Douglas C Montgomery and George C Runger. *Applied statistics and probability for engineers*. John Wiley & Sons, 2010.
 - [100] LH Benedict and RD Gould. Towards better uncertainty estimates for turbulence statistics. *Experiments in fluids*, 22(2):129–136, 1996.

- [101] Christopher Mark Greiner. *Unsteady hot-wire and hot-film wake measurements of automobile-like bluff bodies*. PhD thesis, Massachusetts Institute of Technology, 1989.
- [102] Von Karman Institute lecture. Particle image velocimetry. 2012.
- [103] Dominique Anne-Archard, Daniel Du Colombier, Henri-Claude Boisson, and Vincent Herbert. Analyse des enduits de visualisation pariétale utilisés en aérodynamique. 2006.
- [104] Mathieu Roumeas, Patrick Gilliéron, and Azeddine Kourta. Analysis and control of the near-wake flow over a square-back geometry. *Computers & Fluids*, 38(1):60–70, 2009.
- [105] Exa. Powerflow best practices. *Basic training courses*, 2015.
- [106] Ehab Fares. Unsteady flow simulation of the ahmed reference body using a lattice boltzmann approach. *Computers & fluids*, 35(8):940–950, 2006.
- [107] H Lienhart, C Stoots, and S Becker. Flow and turbulence structures in the wake of a simplified car model (ahmed modell). In *New Results in Numerical and Experimental Fluid Mechanics III*, pages 323–330. Springer, 2002.
- [108] W Regulski and J Szumbariski. Numerical simulation of confined flows past obstacles—the comparative study of lattice boltzmann and spectral element methods. *Archives of Mechanics*, 64(4):423–456, 2012.
- [109] Julian CR Hunt, AA Wray, and Parviz Moin. Eddies, streams, and convergence zones in turbulent flows. In *Studying Turbulence Using Numerical Simulation Databases, 2*, volume 1, pages 193–208, 1988.
- [110] MS Chong, A Eo Perry, and BJ Cantwell. A general classification of three-dimensional flow fields. *Physics of Fluids A: Fluid Dynamics (1989-1993)*, 2(5):765–777, 1990.
- [111] Jinhee Jeong and Fazle Hussain. On the identification of a vortex. *Journal of fluid mechanics*, 285:69–94, 1995.
- [112] Laurent Graftieaux, Marc Michard, and Nathalie Grosjean. Combining piv, pod and vortex identification algorithms for the study of unsteady turbulent swirling flows. *Measurement Science and Technology*, 12(9):1422, 2001.
- [113] Kaouther Ismail. Techniques d’identification des structures cohérentes dans un écoulement 2d. *Laboratoire d’Etudes des Systèmes Thermiques et Energétique*, 2006.
- [114] Amine Koched, Michel Pavageau, and Fethi Aloui. Détection expérimentale de structures tourbillonnaires au sein d’un jet plan confiné en impact. 2011.
- [115] Alexandre Nazarians. Study of the influence of a bluff body rear-end geometry on its aerodynamics. *PSA Internal Report*, 2015.
- [116] Edzard Mercker and Jochen Wiedemann. Comparison of different ground simulation techniques for use in automotive wind tunnels. Technical report, SAE Technical Paper, 1990.
- [117] Vincent Vidal. Vérification de la couche limite du faux plancher maquette. *PSA Internal Report*, 2013.
- [118] Siniša Krajnović and Lars Davidson. Influence of floor motions in wind tunnels on the aerodynamics of road vehicles. *Journal of wind engineering and industrial aerodynamics*, 93(9):677–696, 2005.
- [119] KR Cooper. Bluff-body aerodynamics as applied to vehicles. *Journal of Wind Engineering and Industrial Aerodynamics*, 49(1):1–21, 1993.
- [120] RK Strachan, K Knowles, and NJ Lawson. The vortex structure behind an ahmed reference model in the presence of a moving ground plane. *Experiments in fluids*, 42(5):659–669, 2007.
- [121] Jeff Howell and Derek Hickman. The influence of ground simulation on the aerodynamics of a simple car model. *SAE*, 1997.
- [122] GW Carr. A comparison of the ground-plane-suction and moving-belt ground-representation techniques. Technical report, SAE Technical Paper, 1988.

-
- [123] Cameron Tropea, Alexander L Yarin, and John F Foss. *Springer handbook of experimental fluid mechanics*, volume 1. Springer Science & Business Media, 2007.
- [124] RP Hoxey, AM Reynolds, GM Richardson, AP Robertson, and JL Short. Observations of reynolds number sensitivity in the separated flow region on a bluff body. *Journal of Wind Engineering and Industrial Aerodynamics*, 73(3):231–249, 1998.
- [125] Kevin R Cooper. The effect of front-edge rounding and rear-edge shaping on the aerodynamic drag of bluff vehicles in ground proximity. Technical report, SAE Technical Paper, 1985.
- [126] S Courtine and A Spohn. Dynamics of separation bubbles formed on rounded edges. In *12th International Symposium on Applications of Laser Techniques to Fluid Mechanics. Lisbon, Portugal*. Citeseer, 2004.
- [127] S Depardon, JJ Lasserre, LE Brizzi, and J Borée. 1/4 scale vehiclewake pattern analysis using near-wall piv. Technical report, SAE Technical Paper, 2006.
- [128] Giacomo Rossitto, Christophe Sicot, Valérie Ferrand, Jacques Borée, and Fabien Harambat. Influence of afterbody rounding on the pressure distribution over a fastback vehicle. *Experiments in Fluids*, 57(3):1–12, 2016.
- [129] EC Maskell. A theory of the blockage effects on bluff bodies and stalled wings in a closed wind tunnel. Technical report, DTIC Document, 1963.
- [130] James Keogh, Tracie Barber, Sammy Diasinos, and Doig Graham. The aerodynamic effects on a cornering ahmed body. *Journal of Wind Engineering and Industrial Aerodynamics*, 154:34–46, 2016.
- [131] Jeff Howell and Geoff Le Good. The effect of backlight aspect ratio on vortex and base drag for a simple car-like shape. *SAE*, 2008.
- [132] C Hinterberger, M Garcia-Villalba, and W Rodi. Large eddy simulation of flow around the ahmed body. In *The Aerodynamics of Heavy Vehicles: Trucks, Buses, and Trains*, pages 77–87. Springer, 2004.
- [133] James Venning, D Lo Jacono, David Burton, M Thompson, and John Sheridan. The effect of aspect ratio on the wake of the ahmed body. *Experiments in Fluids*, 56(6):1–11, 2015.
- [134] T Morel. The effect of base slant on the flow pattern and drag of three-dimensional bodies with blunt ends. In *Aerodynamic Drag Mechanisms of Bluff Bodies and Road Vehicles*, pages 191–226. Springer, 1978.
- [135] Matthew Corallo, John Sheridan, and MC Thompson. Effect of aspect ratio on the near-wake flow structure of an ahmed body. *Journal of Wind Engineering and Industrial Aerodynamics*, 147:95–103, 2015.
- [136] C. Jermann, G. Pujals, P. Meliga, E. Serre, and F. Gallaire. Characterization of the streamwise vortices and near-wake dynamics in the turbulent flow around the 25 degrés ahmed body based on spiv. In *Contrôle des décollements: Separated flow control and aerodynamic performance improvements*, 2013.
- [137] Gaignard and Lagny. 3rd year project. *2016, Supaero Graduate Program, ISAE*, 2015.
- [138] DJ Maull. Mechanisms of two and three-dimensional base drag. In *Aerodynamic Drag Mechanisms of Bluff Bodies and Road Vehicles*, pages 137–159. Springer, 1978.
- [139] Hendrik Tennekes and John Leask Lumley. *A first course in turbulence*. MIT press, 1972.
- [140] Patrick Chassaing. *Turbulence en mécanique des fluides: analyse du phénomène dans une perspective de sa modélisation à l’usage de l’ingénieur*. 1990.
- [141] Ilan Kroo. Drag due to lift: concepts for prediction and reduction. *Annual Review of Fluid Mechanics*, 33(1):587–617, 2001.
- [142] Jeff Howell and Geoff Le Good. Vortex drag for a simple bluff body at incidence in ground proximity. Technical report, SAE Technical Paper, 2005.

- [143] Giacomo Rossitto, Christophe Sicot, Valérie Ferrand, Jacques Borée, and Fabien Harambat. Wake structure and drag of vehicles with rounded rear edges. In *50th International Conference on Applied Aerodynamics. 3AF*, 2015.
- [144] Giacomo Rossitto, Christophe Sicot, Valérie Ferrand, Jacques Borée, and Fabien Harambat. Aerodynamic performances of rounded fastback vehicle. *SUBMITTED TO Proceedings of the Institution of Mechanical Engineers, Part D: Journal of Automobile Engineering*, 2016.
- [145] Taeyoung Han and Youngtae Kim. Aerodynamic shape improvement based on surface pressure gradients in the stream-wise and the transverse directions. Technical report, SAE Technical Paper, 2010.
- [146] PSA, 2004. FR 2844599.
- [147] Cornerstone Research Group, 2012. EP 2423104A1.
- [148] NASCAR, 1994. US 5 374 098.
- [149] FIAT, 1987. IT 8767106.
- [150] BMW, 2004. US 2004/0130182 A1.
- [151] GM, 2011. DE102011121909A1.
- [152] PSA, 2003. FR 2854858.
- [153] Brad Duncan. Aston martin’s aeroblade revolutionizes automotive downforce aerodynamics. *www.ecnmag.com*, 2016.

Appendix C

Articles

Article 1

Rossitto et al. "Influence of afterbody rounding on the pressure distribution over a fastback vehicle." *Experiments in Fluids* 57.3 (2016): 1-12.

Influence of afterbody rounding on the pressure distribution over a fastback vehicle

Giacomo Rossitto^{1,2}  · Christophe Sicot² · Valérie Ferrand³ · Jacques Borée² · Fabien Harambat¹

Received: 20 July 2015 / Revised: 4 January 2016 / Accepted: 7 January 2016
© Springer-Verlag Berlin Heidelberg 2016

Abstract Experimental analyzes were performed to understand the drag evolution and the flow field modifications resulting from afterbody rounding on the Ahmed body, a simplified vehicle model with 25 degrees rear slant. Curvature effects were investigated using balance measurements, flow visualizations, wall pressure, and particle image velocimetry measurements. The rear end of the original well-known Ahmed body has sharp connections between the roof and the rear window as well as squared rear pillars. Similarly to previous studies, rounding the roof/backlight intersection was shown to reduce drag up to 16 %. Surprisingly, additional rear curvature associated with side pillar rounding did not further modify the drag. However, the zero net effect was found to result from opposite drag effects on the slanted and vertical surfaces and to hide strong local modifications on the flow field. The tridimensional organization and vorticity transport in the near wake were analyzed and connected to the observed local increase in the pressure drag on the base. Finally, these results were shown to be generic for a realistic rounded-end car shape.

1 Introduction

Facing strict rules for exhaust gases imposed by the European Community at the 2020 horizon (95 g/km of CO₂), car manufacturers have to further reduce fuel consumption and CO₂ emissions. This purpose can be achieved by improving engine efficiency and by reducing energy losses. In this context, significant effort is being put into drag reduction, by means of shape optimization. Rounding the rear part of the vehicle appears to be an interesting solution, but a compromise has to be found between style and aerodynamic efficiency. Most of the fundamental aerodynamic analyzes have been carried out on simplified car models featuring sharp edges at the rear (Ahmed et al. 1984; Davis 1982; Howell and Hickman 1997). Only recently have very few papers addressed the question of rear edge curvature and aerodynamic performances. Thacker et al. (2012) showed that rounding the edge between the roof and the rear slant on the Ahmed body results in a 10 % drag reduction. Authors attributed this reduction to the fully attached flow over the backlight and the downstream motion of the structures developing in the near wake.

Fuller et al. (2014) analyzed the benefits of rounding the rear pillar geometry on the Davis (1982) model. They observed that rounded edges generated a different wake structure dominated by an interaction between the longitudinal vortices and the separated region, resulting in a drag reduction of 11 %.

Based on the literature review, it appears that rounding afterbodies sizably affected aerodynamic loads and flow fields, but systematic investigation into the effects of changing radiuses of upper and side backlight edges was not reported. The present study addresses this question by rounding alternatively and then, simultaneously, the roof and lateral edges of the backlight of an Ahmed model.

✉ Giacomo Rossitto
giacomo.rossitto@ensma.fr

¹ PSA Peugeot Citroën, 2 Route de Gisy,
78943 Velizy-Villacoublay, France

² Institut Pprime, UPR-3346 CNRS, ENSMA, Université de
Poitiers, Poitiers, France

³ Institut Supérieur de l'Aéronautique et de l'Espace
(ISAE-SUPAERO), Université de Toulouse, Toulouse, France

Particular attention was given to understanding how the modified flow on the backlight interacts with the near wake and promotes drag changes.

Three models were used with different afterbody curvatures. To fully characterize the flow pattern on the afterbody and the near wake, wall pressure measurements on the slanted and base surfaces were completed by skin friction line visualizations and stereo-PIV velocity fields.

The description of the experimental setup in Sect. 2 is followed by the comparative analysis of the drag force developing on the three tested configurations. The role of pillar rounding in flow behavior and drag generation is then discussed in Sect. 4. Finally, main conclusions and perspectives of the study are presented. A further study, briefly outlined in “Appendix”, generalizes the results obtained through exploring flow features on a more realistic car body.

2 Experimental setup

All the tests were conducted in the PSA Peugeot Citroën wind tunnel of La Ferté Vidame (France). This Eiffel wind tunnel is 52 m long and has a test section which is 2 m high, 5.2 m wide, and 6 m long. The maximum speed is 53 m/s. The wind tunnel blockage ratio was 1.4 %. The model was placed on an elevated surface as high as approximately half the length of the model, Beaudoin and Aider (2008). The nomenclatures of flow and the geometrical features are reported in Fig. 1. The schematic of the model, the relevant dimensions, and the coordinate system are reported in Fig. 2, [see Ahmed et al. (1984) for a complete description of the body]. The reference length, $\xi = 201$ mm, is the

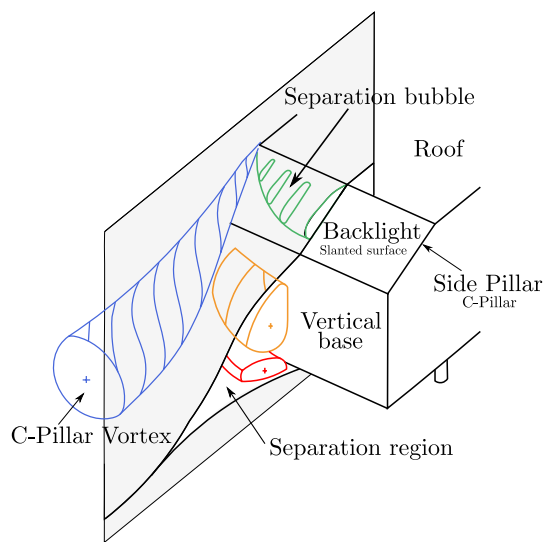


Fig. 1 Nomenclature of flow and geometrical features

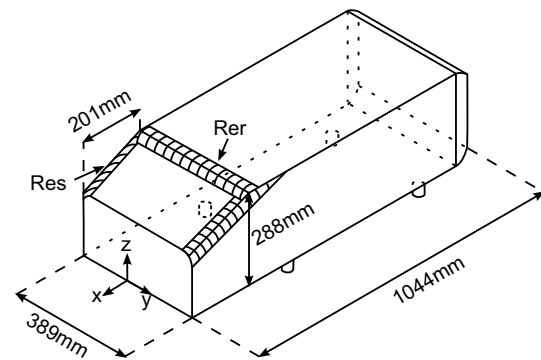


Fig. 2 Ahmed body and location of the rounded edges. *Rer* stands for rounded edge at the end of the roof and *Res* for rounded edge on the side

length of the horizontal projection of the model's rear window. Normalized lengths are noted as starred values. The origin of the Cartesian coordinate system is on the symmetry plane. $X^* \in [-1, 0]$ is the region over the rear slant and $X^* \geq 0$ the near wake. The locations of the rounded edges are reported in Fig. 2: *Rer* stands for the upper edge of the backlight, at the roof junction, and *Res* for the side edges. The models are then called $R_\alpha S_\beta$, where *R* stands for *Roof* and *S* for *Side*. α and β represent the values of the radii. The radius of curvature of the afterbody is expressed as a percentage of the reference length. The reference case with sharp edges (i.e. no curvature) is referred as $R_0 S_0$. The second model with a rounded edge of 10 % between the roof and the rear window is referred $R_{10} S_0$. Finally, the model with 10 % curvature both on the upper and side edge of the backlight is noted $R_{10} S_{10}$. An initial numerical study was conducted to select the roof curvature radius *Rer*, Rositto et al. (2014). It is interesting to notice that drag and lift values obtained with $R_5 S_0$ were very similar to the $R_{40} S_0$ ones. Once the backlight separation bubble is suppressed, further increase in roof edge radius has no effect on aerodynamic loads. 10 % was chosen as the reference roof edge radius, and the same pillar radius was selected for the $R_{10} S_{10}$ model. At this Reynolds number, it was shown that this moderate rounding induces strong local modifications of the flow. However, as in Fuller and Passmore (2014), it was found that separation of the flow along the side and over the rounded C-pillars still occurred. For higher ratios of rounding ($R_{10} S_{>20}$ according to the preliminary numerical study), the side radius is large enough to prevent side flow separation, this case will be briefly described in the “Appendix” for a more realistic model. $R_{10} S_{10}$ is therefore an intermediate configuration between the sharp side $R_{10} S_0$ and high side radius (typically $Res > 20$ %). It was chosen to concentrate on this configuration.

The free stream velocity U_0 was set at 40 m/s, yielding a Reynolds number based on the length of the model of 2.6

10^6 . All velocities are normalized with U_0 and are noted as starred values. To evaluate the aerodynamic coefficients, a six-component balance was used. The drag and lift coefficients were calculated as follows:

$$C_{d,l} = \frac{F_{d,l}}{\frac{1}{2}\rho U_0^2 S}$$

where F is the force measured by the balance, ρ is the density of the air, and S is the frontal surface area of the model. The precision of the balance was 0.001 for the drag coefficient C_d , and 0.002 for the lift coefficient C_l . The static wall pressure coefficient at one point i was computed from the expression:

$$C_P(i) = \frac{P(i) - P_0}{\frac{1}{2}\rho U_0^2}$$

where $P(i)$ is the static pressure of point (i) , P_0 the static pressure measured upstream of the model. The left-hand side of the models was equipped with 115 pressure probes connected to a SCANdaq 8000 acquisition system. The acquisition rate was 40 Hz for 3000 samples, thus giving 75 s of time recording.

Furthermore, PIV measurements were acquired in the wake of the Ahmed body. The laser sheet was set by a 2×120 mJ Nd:Yag Quantum Big Sky Laser. The Dantec Flowsense 4M mkII (2024 pixels \times 2024 pixels) equipped with 105-mm lenses generated 462 mm \times 462 mm fields of view. 2D PIV was performed on xz planes: $Y^* = 0$, $Y^* = 0.49$ and $Y^* = 0.97$. Twenty-six zy planes were recorded using the stereo-PIV techniques to obtain the three velocity components of the flow field: six planes over the rear window, $X^* \in [-1, 0]$ with a non-uniform spacing between them and 20 planes in the near wake, $X^* \in [0, 0.5]$ every $\Delta X^* = 0.025$. Post-processing was performed with a final interrogation window of 16×16 pixels, after an initial window of 32×32 pixels, with an overlap of 50 % in the horizontal and vertical directions. Grid spacing was then 1.82 mm. Eight hundred images were recorded with a 7 Hz trigger rate. With this setting, the 95 % confidence limit represents approximately ± 3 % of the mean velocity.

Stereo-PIV data were also analyzed by using the Γ_2 criterion. This vortex identification algorithm allows the identification of regions of dominant rotation in a flow with an integral and normalized criterion. It was introduced by Graftieaux et al. (2001) in order to identify vortices for unsteady turbulent flows. The Γ_2 criterion, taking into account the average convection velocity in the domain S , is a Galilean invariant. Γ_2 is defined by the relation:

$$\Gamma_2 = \frac{1}{S} \iint_S \frac{[\mathbf{PM} \wedge (\mathbf{U}_M - \mathbf{U}_P)] \cdot \mathbf{e}_x}{\|\mathbf{PM}\| \cdot \|\mathbf{U}_M - \mathbf{U}_P\|} dS$$

$$\mathbf{U}_P = \frac{1}{S} \iint_S \mathbf{U} dS$$

where S is a two-dimensional area surrounding P and M points in S . A dominant rotation is then defined for $\frac{2}{\pi} \leq |\Gamma_2| \leq 1$. In what follows, the domain S was chosen to include 24 PIV velocity vectors surrounding P .

3 Global analysis of the drag force

In this section, the aerodynamic drag and lift of the three tested configurations are presented and analyzed in terms of pressure distribution and global flow structure in the near wake.

3.1 Aerodynamic coefficients

Measurements of drag and lift coefficients are summarized in Table 1 for the three tested configurations R_0S_0 (reference case), $R_{10}S_0$ and $R_{10}S_{10}$. The analysis is based on the relative variation with respect to the reference case. For the reference case, the measured C_d coefficient is found to be higher than the one presented by Ahmed et al. (1984) ($C_d = 0.285$ at 60 m/s); nevertheless, this value is consistent with other studies such as Conan et al. (2011) and Joseph et al. (2012). The recirculation length on the rear window appears to be very sensitive to the quality of the upper sharp edge, Joseph (2012). Differences in bubble lengths could explain deviations on the drag coefficient between similar studies. This is not a hindrance for this work because the purpose is the relative comparison between the three tested models.

When rounding the backlight upper edge ($R_{10}S_0$ model), a subsequent 16 % drag reduction is observed. With a 40 % roof curvature radius, Thacker et al. (2012) measured a comparable reduction, i.e. 10 %. Explanations on the origin of the drag reduction will be developed in the following sections. The addition of rear curvature with rounded pillars does not induce any changes in the overall drag: The $R_{10}S_{10}$ model shows the same drag coefficient as the $R_{10}S_0$

Table 1 Aerodynamic coefficients and their variation with respect to the reference case R_0S_0

| | C_d | C_l | ΔC_d | ΔC_l |
|----------------|-------|-------|--------------|--------------|
| R_0S_0 | 0.356 | 0.311 | — | — |
| $R_{10}S_0$ | 0.297 | 0.333 | −16 % | +7 % |
| $R_{10}S_{10}$ | 0.298 | 0.254 | −16 % | −18 % |

one. This point will be shown to result from strong local opposite effects on the slanted and vertical surfaces.

Regarding lift coefficient, the $R_{10}S_0$ case shows a moderate increase when compared to the sharp edge configuration. This increase is caused by flow acceleration around the rounded upper edge. It can be noticed that in automotive aerodynamics, increasing lift is detrimental in terms of stability and braking distance, Katz (1995). A strong reduction in lift is observed for the case $R_{10}S_{10}$. It will be hereunder shown that the global evolution of the pressure recovery over the slanted surface and the reduction in the intensity of the longitudinal vortices are responsible for this positive effect.

3.2 Interpretation of static wall pressure distribution and velocity fields in the plane of symmetry

3.2.1 R_0S_0 configuration

For the reference configuration R_0S_0 , Ahmed et al. (1984) identified three main sources of pressure drag generated along the slanted surface and in the near wake of the body. Due to the sharp edge between the roof and the backlight, the flow experiences separation–reattachment, thereby forming a separated bubble along the slanted surface. The length of the recirculation zone was found here to cover 75 % of the rear window, which is consistent with the available literature, Joseph (2012).

The second drag source is associated with the highly energetic longitudinal vortex, the so-called C-pillar vortex, developing along the rear side pillars. Its presence leads to a strong localized low pressure on the side of the rear slant, shown on the right side in Fig. 3.

The third major source of drag is associated with the separated region in the near wake (left side of Fig. 3) leading to the low-pressure distribution along the vertical base (right side of Fig. 3). It is useful to define here a variable L^* as the length of the mean recirculation region identified by the saddle point in the streamlines of the near wake. Precisely, $L^* = 0.89$ for R_0S_0 (see Fig. 3). L^* will be used in Sect. 4 as a characteristic length for the crossflow analysis.

3.2.2 $R_{10}S_0$ configuration

When rounding the upper edge of the slanted surface, noticeable changes are observed in the flow field. No separation occurs at the junction between the roof and the rear slant. A low-pressure area around the rounded edge is generated, followed by a pressure recovery over the rear slant (Fig. 4). The flow remains fully attached until it separates at the end of the rear window. On the side of the model, the C-pillar vortex is still present, as illustrated in Fig. 4 by the concentrated streamwise vorticity. The low-pressure

footprint of the longitudinal vortex does not exhibit any significant differences compared with the reference case. The time-averaged streamlines in the plane of symmetry of the near wake show a counter-rotating system more symmetrical than the R_0S_0 configuration. Moreover, those structures, related to low static pressure, are shifted further downstream, thus increasing the mean recirculation bubble by 12 % ($L^* = 1$) over the reference sharp case. To help interpreting the origin of lift and drag alteration for the rounded Ahmed bodies, the static pressure coefficient has been integrated separately over the slanted surface and the vertical base. Table 2 reports the percentage change in the pressure coefficient for the $R_{10}S_0$ and $R_{10}S_{10}$ models compared to R_0S_0 . Although the lack of pressure probes along the rounded pillars makes those results an estimation, it appears clearly that the downstream motion of the wake structures leads to an increase in base pressure of up to 28 % for the $R_{10}S_0$ configuration.

3.2.3 $R_{10}S_{10}$ configuration

One important observation made during this study, discussed in more detail in Sect. 4, is that the rounding of the C-pillar displaces the origin of the longitudinal vortex toward the base of the body along the C-pillar. This effect is also described for flows over delta wings featuring blunt and rounded leading edges, see Luckring (2013). In this case, the origin of the longitudinal vortices is displaced downstream along the leading edge. For the $R_{10}S_{10}$ configuration, the streamwise vorticity related to the vortex is less concentrated and weaker when compared with the $R_{10}S_0$ configuration (Figs. 4, 5). The associated low-pressure footprint is also weaker and more localized at the bottom of the C-pillar. The pressure recovery on the slanted surface appears much more effective for $R_{10}S_{10}$ than for the other configurations (Figs. 3, 4, 5; Table 2). This point can justify the 18 % lift reduction reported in Table 1. Despite the reduction in the C-pillar vortex and the better pressure recovery on the slanted surface, no drag reduction was observed for the $R_{10}S_{10}$ case when compared with the $R_{10}S_0$ configuration (Table 1). The C_p distribution on the vertical base (Fig. 5) and the corresponding average surface value (Table 2) indicate a clear decrease in pressure on the base (−32 % compared with $R_{10}S_0$). $L^* = 0.9$ for this configuration. In terms of drag generation, the unfavorable effect on the base balances exactly the positive effect on the slanted surface. Note that this zero net balance is of course specific to the shape of the rear end and, in particular, to the ratio between the base height and the vertical projection of the rear window, Howell and Good (2008).

Figure 6 shows the evolution of C_p along the symmetry plane for the three models more quantitatively. At the

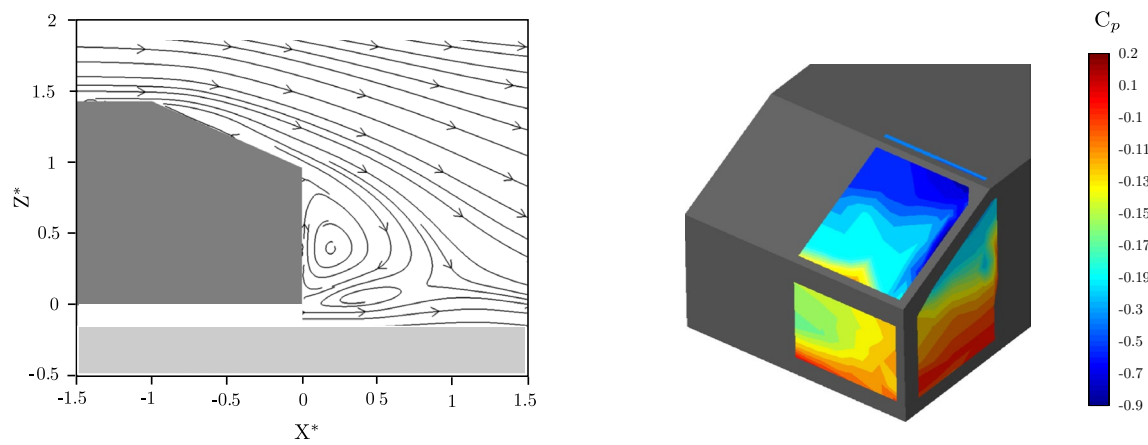


Fig. 3 R_0S_0 Left time-averaged streamlines at $Y^* = 0$. Right wall pressure coefficient C_p on the right half

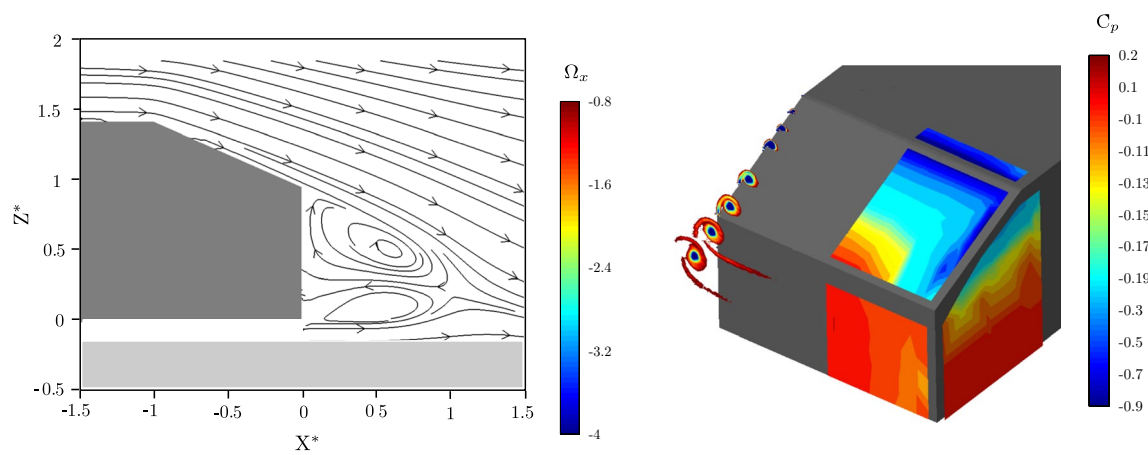


Fig. 4 $R_{10}S_0$ Left time-averaged streamlines at $Y^* = 0$. Right streamwise vorticity Ω_x on the left half and wall pressure coefficient C_p on the right half

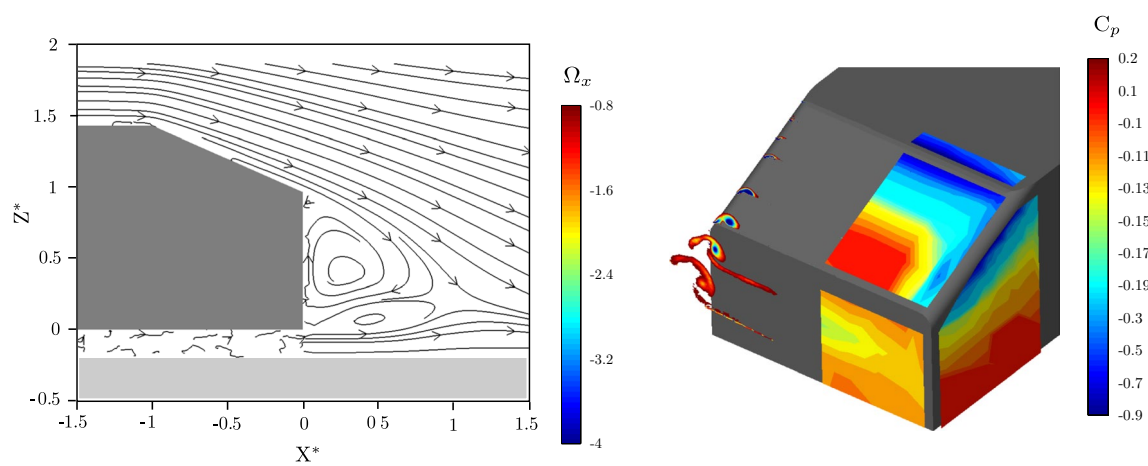
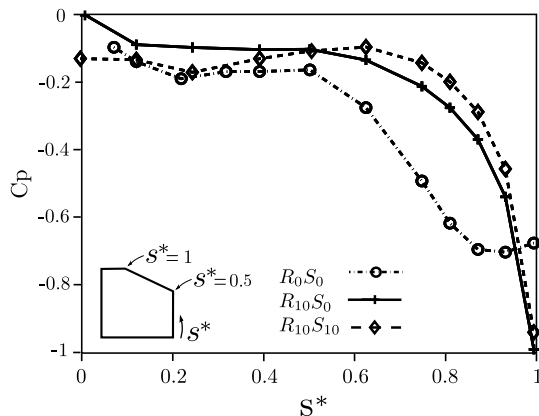
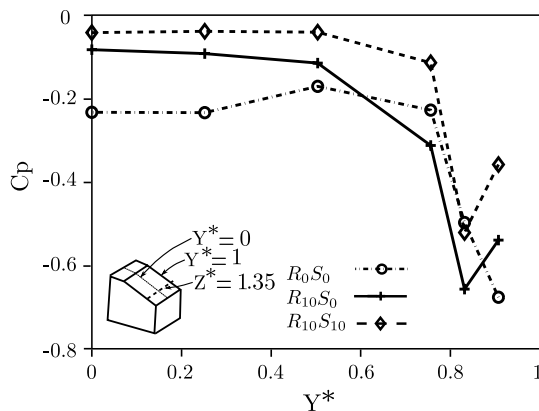


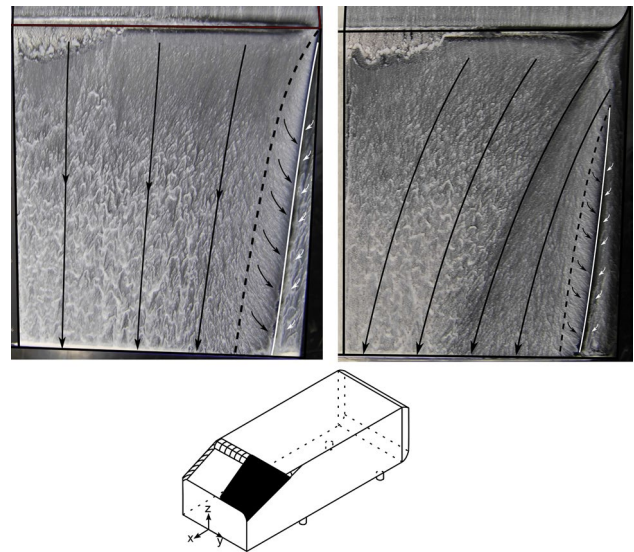
Fig. 5 $R_{10}S_{10}$ Left time-averaged streamlines at $Y^* = 0$. Right streamwise vorticity Ω_x on the left half and wall pressure coefficient C_p on the right half

Table 2 Variation in spatially averaged mean C_p over the rear window and vertical surface relative to the reference case R_0S_0

| | Rear window ΔC_p | Vertical surface ΔC_p |
|----------------|--------------------------|-------------------------------|
| R_0S_0 | — | — |
| $R_{10}S_0$ | +10 % | +28 % |
| $R_{10}S_{10}$ | +31 % | +5 % |

**Fig. 6** Pressure distribution in the symmetry plane ($Y^* = 0$) for all models**Fig. 7** Pressure distribution at constant $Z^* = 1.35$ for all models

first probe along the slanted surface, $s^* = 1$, the low C_p for $R_{10}S_0$ and $R_{10}S_{10}$ is due to the acceleration over the rounded edge on the roof. The sharp edge at the end of the roof generates a separation region, constant C_p up to $s^* = 0.85$, for the reference case. On the contrary, the pressure coefficient of the models with a rounded edge on the top exhibits a pressure recovery all over the rear window. The pressure recovery is even larger for the $R_{10}S_{10}$ model compared with $R_{10}S_0$. However, the decrease in C_p along the vertical surface is noticeable for the $R_{10}S_{10}$, showing that the flow dynamics in the 3D wake downstream of the

**Fig. 8** Oil flow visualization: Left $R_{10}S_0$. Right $R_{10}S_{10}$. Dashed black line is the attachment line of the primary vortex, and solid white line is the separation line of the secondary vortex. Bottom Position of the paint visualization

rounded configuration results in a low-pressure footprint associated to drag penalty, as discussed previously.

Figure 7 reports the spanwise evolution of C_p for $Z^* = 1.35$, (this location corresponds to $s^* = 0.6$ in Fig. 6). Model $R_{10}S_{10}$ has clearly a higher C_p value, more uniform along the transverse direction with respect to $R_{10}S_0$. As stated by Fuller and Passmore (2014), the higher central downwash speed induced by the stronger trailing vortices for the $R_{10}S_0$ case is expected to contribute to the lower C_p values in comparison with $R_{10}S_{10}$ case. A weaker C-pillar vortex for $R_{10}S_{10}$ should also be responsible for the more uniform C_p distribution across the backlight observed in Fig. 7. The low intensity of the C-pillar vortex pressure footprint for $R_{10}S_{10}$ is also observed at $Y^* = 0.9$.

4 On the effect of pillar rounding on the near wake development

Oil flow visualizations were performed to investigate the skin friction lines for both the $R_{10}S_0$ and $R_{10}S_{10}$ models, white and black lines were superimposed to the pictures to emphasize the main structures in Fig. 8. On the side of the model, the dashed black line represents the attachment line of the primary vortex and the solid white line the separation line of the secondary vortex [see Krajnović and Davidson (2005) for a complete description of the topology of the pillar vortex]. Closer to the center region, skin friction lines cannot be interpreted directly and long black arrows

indicate the overall direction of the flow off the surface. The footprint of the C-pillar vortex is wider for the $R_{10}S_0$ case, and moreover, it is observed that the origin of the vortex is shifted downstream for $R_{10}S_{10}$. On the upper part of

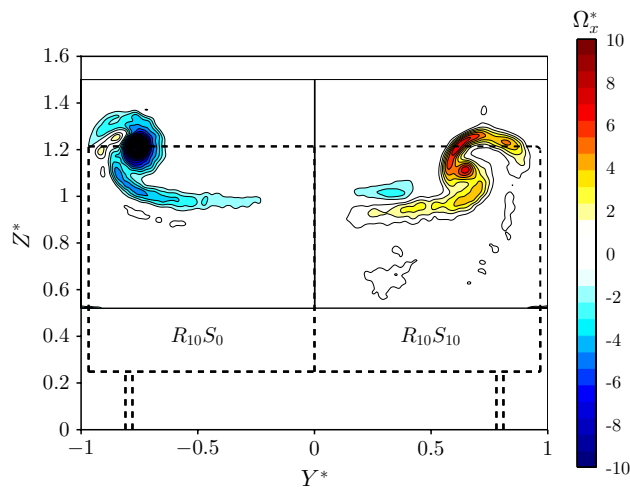


Fig. 9 Mean streamwise vorticity $\Omega_x^* = \frac{\Omega_x \xi}{U_0}$, plane at $X^* = L^*/2$. The dashed lines represent the geometry of the model

the rounded pillar, $R_{10}S_{10}$, some attached flow penetrates toward the center line. That flow comes from the side of the model and does not roll up directly in the C-pillar vortex as in the sharp case, but penetrates directly over the rear window. The analysis of the oil flow visualization brings to evidence the different topology of the skin friction lines over the rear window, due to the geometrical differences in the side rear pillars of the models.

Contours of the mean streamwise vorticity in the plane $X^* = L^*/2$ are proposed in Fig. 9. Small values of streamwise vorticity are not displayed, so as to focus the attention on the vortical structures generated from the side pillars. A concentrated region of vorticity is observed for $R_{10}S_0$ and corresponds to the longitudinal vortex. For the rounded case, the streamwise mean vorticity is distributed over a wider area of the near wake. A small region of negative vorticity is also observed for $Y^* \approx 0.4$ and $Z^* \approx 1$. A closer look at the oil visualization in Fig. 8 and to V^* in Fig. 10b shows that this occurs in the zone of confluence between the flow over the top of the body and the lateral flow drawn from the side. In that region, a clear change in sign of the gradient $\frac{\partial V^*}{\partial z}$ is observed, and this contributes to the change in sign of the streamwise vorticity.

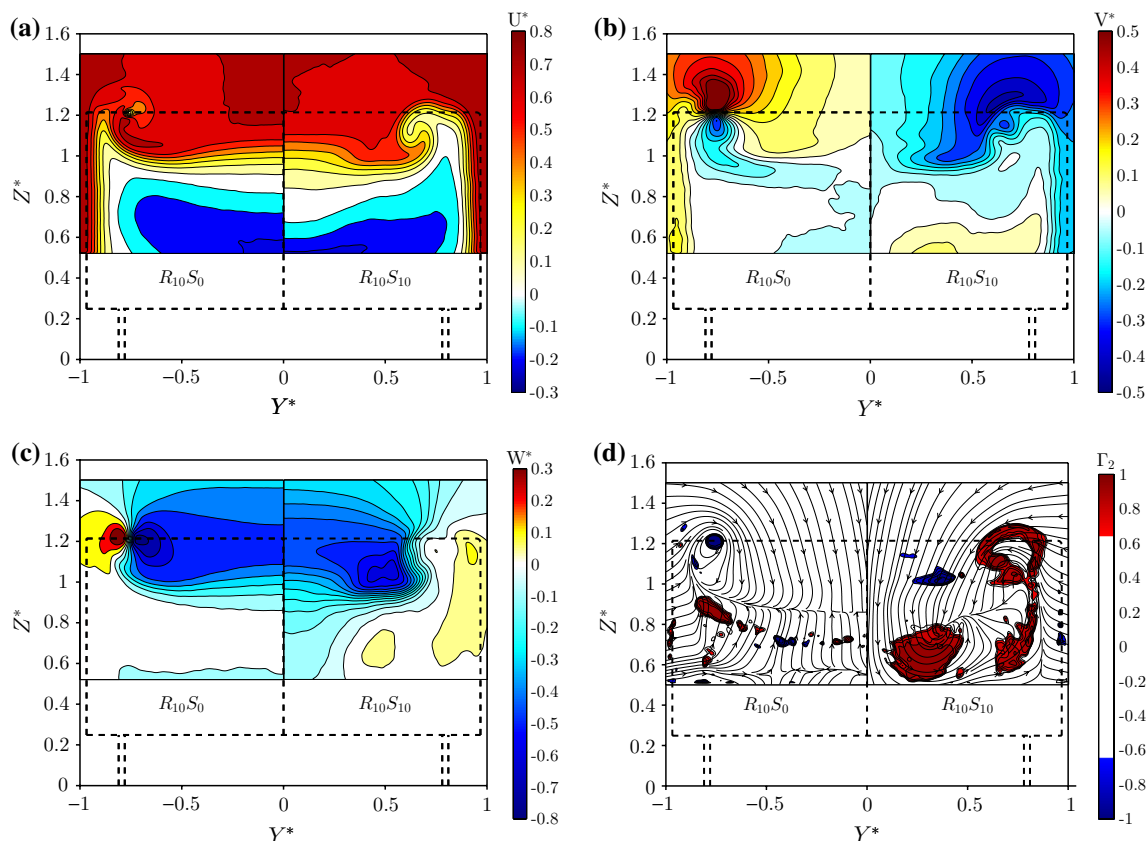


Fig. 10 Plane at $X^* = L^*/2$. The dashed lines represent the geometry of the model, (a) mean streamwise velocity U^* , (b) mean spanwise velocity V^* , (c) mean normal velocity W^* , (d) Γ_2

Figure 10 shows the three components of the mean velocity field at $X^* = L^*/2$. Each picture is divided into two: the left side represents $R_{10}S_0$ and the right side $R_{10}S_{10}$. The data are all recorded for $Y^* \in [0; 1]$, so the data visualization related to $R_{10}S_0$ is a mirror symmetry.

The different organization of the near wake flow should be noticed. In particular, the horizontal shear layer downstream separation is transported downward when rounded edges are present. The topology of the mean near wake flow and of the recirculation bubble is thus changed. When comparing the transverse velocities (V^*) in the horizontal shear layer region downstream of the slanted surface, the inward motion is clear for $R_{10}S_{10}$ while significant inward V^* values are just present around the vortex core for $R_{10}S_0$. For the rounded case, Fig. 10c shows that this mean inward motion before separation results in a strong downwash effect (negative W^*) in the core region of the wake.

For rear end with a slanted angle, a pressure gradient is induced between the side of the model and the rear end, Ahmed et al. (1984). As a consequence, the flow along the side is drawn in toward the center. The sharp side pillar forces the lateral flow to separate, generating a longitudinal vortex. One could therefore suggest that, for $R_{10}S_0$, the sharp lateral edges “shield” the wake separation region at the base and enable a “two-dimensional” separation, “2D” meaning that the mean streamlines at separation are more parallel to the orientation of the flow over the window, while longitudinal vorticity is concentrated in the C-pillar vortices. On the contrary, for rounded edges, the flow is drawn in from the sides, toward the center over the slanted surface. The separation at the base is then notably 3D for $R_{10}S_{10}$, associated with high spanwise and vertical velocity components.

The contours of Γ_2 , computed using V^* and W^* velocity components, report the rotational behavior of the flow. Two-dimensional lines tangent at each point to the vector (V^*, W^*) are also drawn in Fig 10d. Of course, these lines are not meant to be mean streamlines. They are drawn here because they clearly show the overall rotation of the $R_{10}S_{10}$ wake around the longitudinal axis. For $R_{10}S_0$, a concentrated region of Γ_2 corresponds to the C-pillar vortex. For $R_{10}S_{10}$, the criterion reveals a zone of coherent rotation around the pillar vortex and a large zone in the center bottom region of the wake. The high spanwise and vertical velocity associated with the transversal flow therefore results in a global rotation of the flow in the near wake that will be discussed more quantitatively in what follows (see Fig. 12 and associated comments). The downwash effect is also particularly clear when looking at Fig. 11, which compares the turbulent kinetic energy at $X^* = L^*/2$. The 3D shear layers and the wake recirculating region (see the region of negative U^* in Fig. 10a)

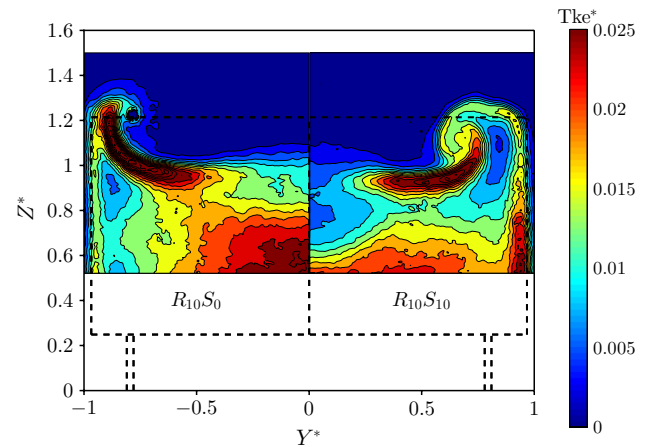


Fig. 11 Turbulent kinetic energy Tke^* , plane at $X^* = L^*/2$. The dashed lines represent the geometry of the model

are the location of a large fluctuating level. For $R_{10}S_{10}$, the “potential” outer flow, characterized by a low level of turbulent kinetic energy, penetrates downward in the near wake. As a consequence, the fluctuating kinetic energy is much lower in this region, as shown in the zone around $Y^* \in [0; 0.2]$ and $Z^* \in [0.6; 1]$. For rounded rear ends, the three-dimensional property of the near wake structure therefore results in more pronounced streamline curvatures and lower pressure on the base when compared with a similar model featuring sharp lateral edges. Note that the downward deviation of the mean streamlines separating from the slanted surface is particularly manifest when looking at the orientation of the streamlines in the plane of symmetry in Fig. 5.

Along three-dimensional geometries, 3D vorticity is generated at the wall along the curved surface, transported, tilted, and stretched in the 3D boundary layer region. In what follows, it is proposed to discuss some integral properties of the longitudinal vorticity field along the near wake of the body. One specificity and limitation of the data presented is that, contrary to the recent study of Venning et al. (2015), the detailed stereo-PIV database only concerns velocity planes measured near the rear vertical surface. This region spans approximately over half of the mean recirculating bubble (see Figs. 4, 5) where the mean recirculating flux is significant. Moreover, the model used here being four times as large as the body of Venning et al., the field of view of each plane does not include the full height of the wake. In particular, the under-hood flow and the bottom region of the wake are not captured. The following discussion must therefore be considered as qualitative. It was however checked that all conclusions discussed here are consistent with the results from all numerical simulations performed by Rossitto et al. (2014).

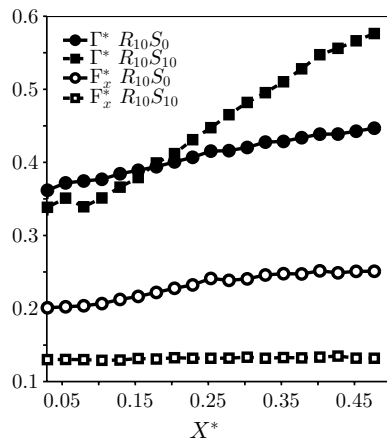


Fig. 12 Longitudinal evolution of the mean circulation and the flux of mean longitudinal vorticity in the near wake

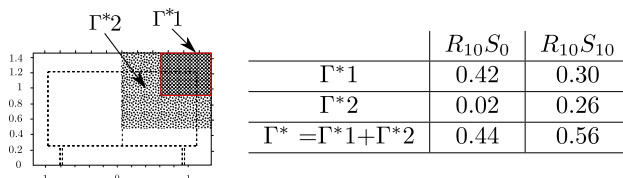


Fig. 13 Zone of calculation and values of circulation at $X^* = L^*/2$. The dashed lines represent the geometry of the model

The longitudinal evolution of the mean circulation $\Gamma^* = \int_{S^*} \Omega_x^* dS$ and the flux of mean longitudinal vorticity $F_x^* = \int_{S^*} U^* \Omega_x^* dS$ are plotted in Fig. 12 for both configurations. As circulation is the integral of the longitudinal vorticity, it is natural to consider the balance of Ω_x as a constitutive element of the structuration of the wake.

First, it is noticed that F_x^* is in the order of 0.13 for $R_{10}S_{10}$ and 0.25 for $R_{10}S_0$ at $X^* = L^*/2$. F_x^* is a non-dimensional quantity, in which the scaling quantity is ξU_0^2 . The scaling length ξ , defined in Fig. 2, is equal to 201 mm. The length l of the perimeter of the vertical base of the model is about $l \approx 5.8\xi$. In the ideal case of a 2D boundary layer of thickness δ and external velocity U_0 separating at a sharp edge, the absolute value of the flux of vorticity per unit span reads simply as $|F_\perp| = \int_0^\delta U \frac{\partial U}{\partial n} dn = \frac{U_0^2}{2}$ where n is the direction perpendicular to the wall and $-\frac{\partial U}{\partial n} = \Omega_\perp$ denotes the only nonzero component of the vorticity vector. By integration of the absolute value of the vorticity flux along the perimeter of the vertical base, an order of magnitude of the total longitudinal mean flux of vertical and transversal mean vorticity shed at the base of the body is therefore $F_{YZ} \approx \frac{U_0^2 l}{2}$. Comparing this order of magnitude with $2F_X$ (F_X concerns approximately half of the wake surface), we obtain $2F_X/F_{YZ} \approx 4\xi F_X^*/l \approx 2F_X^*/3$ that is to

say $2F_X/F_{YZ} \approx 0.08$ for $R_{10}S_{10}$ and $2F_X/F_{YZ} \approx 0.16$ for $R_{10}S_0$. It is therefore shown that the flux of organized longitudinal vorticity is only a small portion of the base flux. However, this experiment shows that it has a significant global incidence on the pressure distribution and drag of the body.

The second observation is that F_x^* is quasi-constant for $R_{10}S_{10}$ and increases moderately for $R_{10}S_0$ (a 25 % increase over the measurement region). Integrating the longitudinal vorticity equation in a control volume bounded by two measurement planes at X^* and $X^* + \Delta X^*$, the longitudinal evolution of F_x^* is due to the flux of Ω_x^* across the lateral boundaries and to the integral of the source terms in the control volume (viscous diffusion can be neglected at this Reynolds number; turbulent transport was not evaluated but should be zero along the plane of symmetry and negligible if the boundaries of the control volume are out of the wake, which is not the case here for the base). The source terms correspond to the average of the stretching of longitudinal vorticity $\Omega_x^* \frac{\partial U}{\partial x}$ and of the tilting of lateral and vertical vorticity $\Omega_y^* \frac{\partial U}{\partial y} + \Omega_z^* \frac{\partial U}{\partial z}$ (Tennekes and Lumley 1972; Chassaing 1990). In the present case, it was checked that the non-dimensional lateral and vertical fluxes are significantly smaller than the longitudinal flux of vorticity (smaller than 5 % of F_x^*). Figure 12 shows that the net effect of the source terms over the measurement volume is small for $R_{10}S_0$ and negligible for $R_{10}S_{10}$. From an integral point of view, the longitudinal mean transport of mean longitudinal vorticity seems therefore to be the dominant term in the near wake.

The third observation relative to Fig. 12 is that, despite the constancy of the flux, the integral of the vorticity over the measurement domain, circulation Γ^* , increases significantly. The rate of increase is notably greater for $R_{10}S_{10}$ than for $R_{10}S_0$, about three times as much for the former as for the latter. To understand simply this observation, it was chosen to divide the total domain in two fixed parts (see sketch in Fig. 13). This partition is quite arbitrary, but is sufficient for the discussion. Region 1 includes the C-pillar vortex and covers 1/4 of the field of measurements: $Y^* \in [0.44, 0.89]$, $Z^* \in [1, 1.5]$. Region “2” is the remaining area. Γ^*1 (respectively Γ^*2) represents the circulation associated with region 1 (respectively 2). Naturally, we have $\Gamma^* = \Gamma^*1 + \Gamma^*2$. Figure 13 displays this decomposition at $X^* = L^*/2$. It is clear that circulation Γ^*1 in the region including the vortex is larger for $R_{10}S_0$ than for $R_{10}S_{10}$. This is related to the higher circulation gathered in the C-pillar vortex. However, while Γ^*2 is less than 5 % of the total value of Γ^* for $R_{10}S_0$, it is about 50 % of the total circulation for $R_{10}S_{10}$. The 3D wake generated by rounded C-pillar therefore significantly differs from the sharp pillar configuration in

that the longitudinal vorticity is transported in the core of the wake in a more distributed way. This is consistent with Fig. 9 in which this observation was already made. The fact that the flux F_X^* is a constant is surprising but does not contradict this observation, because a significant part of the vorticity distributed in region 2 is associated with a reversal flow. For the rounded case, this upstream transport of longitudinal vorticity very close to the base of the body is responsible for low-pressure regions and more drag. It will be shown in the “Appendix” that this effect is amplified if rounding of the back pillar is more pronounced.

5 Conclusions

Analysis has been performed to gain understanding in the effect of afterbody rounding on the generation of aerodynamic forces on a blunt body. Simplified vehicle models with a 25 degrees rear slant presenting different upper and side edge curvatures have been investigated. Similarly to previous studies, rounding the upper edge was shown to reduce drag up to 16 %, linked to the separation suppression on the slanted surface and the lengthening of the separation region close to the vertical base. For this particular geometry, surprisingly, additional rear curvature associated with pillar rounding did not further improve the drag. However, the zero net effect was found to result from opposite behaviors of the flow on the slanted and vertical surfaces and to hide strong local modifications of the flow field. When rounding the side edge, the C-pillar vortex becomes weaker and a better pressure recovery is observed on the slanted surface. Both of these effects are favorable to the reduction in lift and drag. Furthermore, for this rounded configuration, the lateral flow not only feeds the C-pillar vortex but part of it penetrates the slanted surface toward the center line. This mean inward motion before separation has been found to promote a strong downwash in the core region of the wake. The resulting three-dimensional near wake exhibits a more pronounced streamline curvature and a lower pressure on the base when compared with a similar model with sharp lateral edges. It is suggested that the upstream transport of mean streamwise vorticity next to the vertical base is responsible for low-pressure regions. In terms of drag, this unfavorable pressure distribution on the base counterbalances the gain obtained in the slanted surface for this particular geometry. Additional experimental tests, reported in the “Appendix” were performed to understand the effect of rounding the side pillars of a realistic model. Similarly to the Ahmed model, the flow field past the rear end is strongly modified despite a small variation in drag.

Acknowledgments The authors are thankful to L. Mies who took care of the production process of the models and to Y. Goraguer, the wind tunnel manager, for his precious help during the experiments. We acknowledge A. Glad for reviewing the English of the paper. This work has been performed in the framework of the “OpenLab Fluidics” @Poitiers.

Appendix

The present work pointed out that a small edge radius on the side of a simplified car model modifies the flux and the orientation of the mean vorticity vector. One should not forget that realistic cars tend to have large radii of curvature. This justifies the need to test the effect of a large radius of curvature over a realistic car shape to prove that the $R_{10}S_{10}$ rear end of the Ahmed model is an intermediate configuration where C-pillar vortices are delayed but still present in a weaker way. The aim of this complementary test was to increase the physical understanding of the phenomena and prove that what was understood thanks to the Ahmed body rounding can be exploited for more realistic models.

The chosen model and its relevant dimensions are exhibited in Fig. 14. Two different rear ends were tested: one with a sharp lateral radius and one with an edge radius corresponding to 40 % of the span of the vehicle. Both rear ends have a rounded edge at the end of the roof to avoid flow separation over the rear window.

Table 3 reports the variation in the drag and lift coefficients for the rounded rear end compared with the sharp one, (the value of drag and lift is not reported because they are meaningless since this model is a unique prototype). As an order of magnitude, the drag coefficient

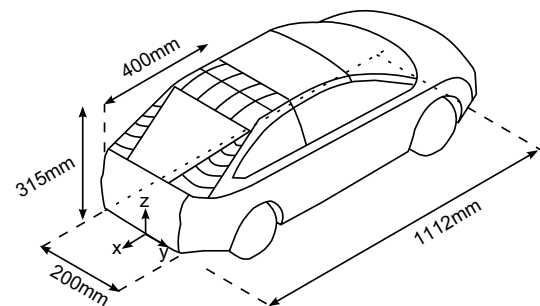


Fig. 14 Realistic model and location of the rounded edges

Table 3 Variation in aerodynamic coefficients relative to the sharp case

| | ΔC_d | ΔC_l |
|---------|--------------|--------------|
| Sharp | – | – |
| Rounded | +1.5 % | –8.5 % |

of the sharp rear end is 35 % less than the reference Ahmed body. The rounded configuration exhibits a slight increase in drag. As for the Ahmed body, this hides major local flow modifications. On the contrary, lift is strongly reduced, which demonstrates the influence of the rounded edge on the C-pillar.

When comparing with Fig. 8, similar oil flow visualization interpretations were made for the realistic model in Fig. 15. The sharp configuration, reported on the left side of the picture, clearly demonstrates the presence of a C-pillar vortex. For the rounded configuration, the large curvature does not even generate a delayed C-pillar vortex; all the flow that comes from the side of the model, in fact, enters the rear window region through an inward transverse attached flow.

Figure 16 highlights the pressure wall measurements over the rear ends. Due to the complexity of the side surface of the model, as for example a realistic gap between the window and the side surface of the model, the C-pillar vortex pressure footprint is less intense than the modified Ahmed body, but still present in the sharp case. The pressure distributions on the side of the rounded edge rear end confirm the absence of the C-pillar vortex. As with the modified Ahmed body, the

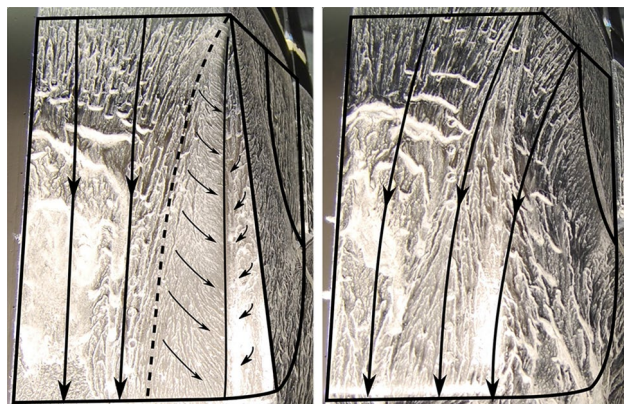


Fig. 15 Oil visualization. *Left* sharp rear end. *Right* rounded rear end. *Dashed line* is the attachment line of the primary vortex, and *solid line* is the separation line of the secondary vortex. *Long arrows* indicate the overall direction of the flow off the surface

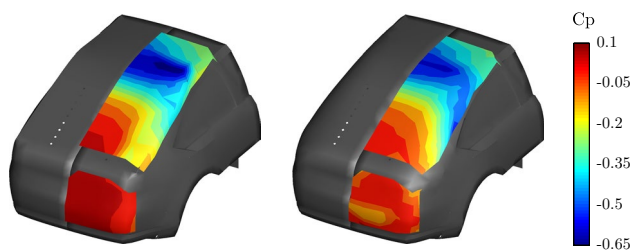


Fig. 16 Wall pressure coefficient C_p : left sharp, right rounded

Table 4 Variation in spatially averaged mean C_p over the rear window and vertical surface relative to the sharp case

| | Rear window ΔC_p | Vertical surface ΔC_p |
|---------|--------------------------|-------------------------------|
| Sharp | — | — |
| Rounded | +10 % | −300 % |

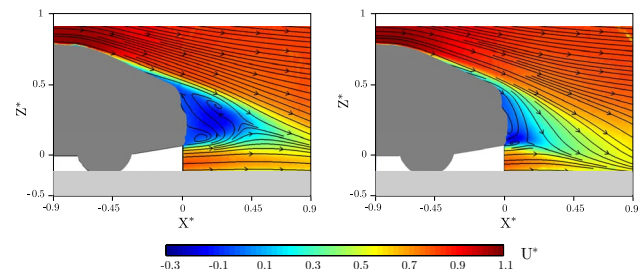


Fig. 17 Streamwise velocity U^* at $Y^* = 0$. *Left* sharp rear end. *Right* rounded rear end

vertical surface displays a lower pressure coefficient than for the sharp case, Table 4. For the Ahmed body, the loss of pressure on the vertical surface compensates for the gain over the rear window when a rounded edge is present. This is not the case for the realistic model, where the net balance between the loss and the gain is not zero ($\Delta C_d = +1.5$ %, see Table 3). This underlines the generic nature of the positive and negative effects over the two zones of the rear end, but points out that every model has its own ratio between the vertical surface and the rear window, which influences drag balance, Howell and Good (2008).

PIV was also performed in the symmetry plane of the model Fig. 17. It is noticed that the rounding of the C-pillar induces strong effects in the near wake close to the vertical surface. When rounding the C-pillar, the length of the separated region is strongly reduced and no “spanwise” large-scale rotation is detected in the symmetry plane. In fact, the separated zone is now a fully 3D flow. To understand this modification of topology in the near wake, YZ stereo-PIV planes are reported in Fig. 18 at $X^* = 0.07$.

Figure 18a evidences the presence of the C-pillar vortex in the sharp case due to its characteristic streamwise velocity contours, no sign of the vortex is visible on the right side of the picture. On the top of the separated region, the vortex generated from the front of the vehicles, the so-called A-pillars, is visible for both models. The spanwise velocity is reported in Fig. 18b. While for the sharp rear end there are two opposite regions of localized transverse velocity due to the C-pillar vortex, for the rounded rear only an intense region of lateral flow that comes from the side (and is injected in the near wake) is present. The resulting downwash is visible in the right

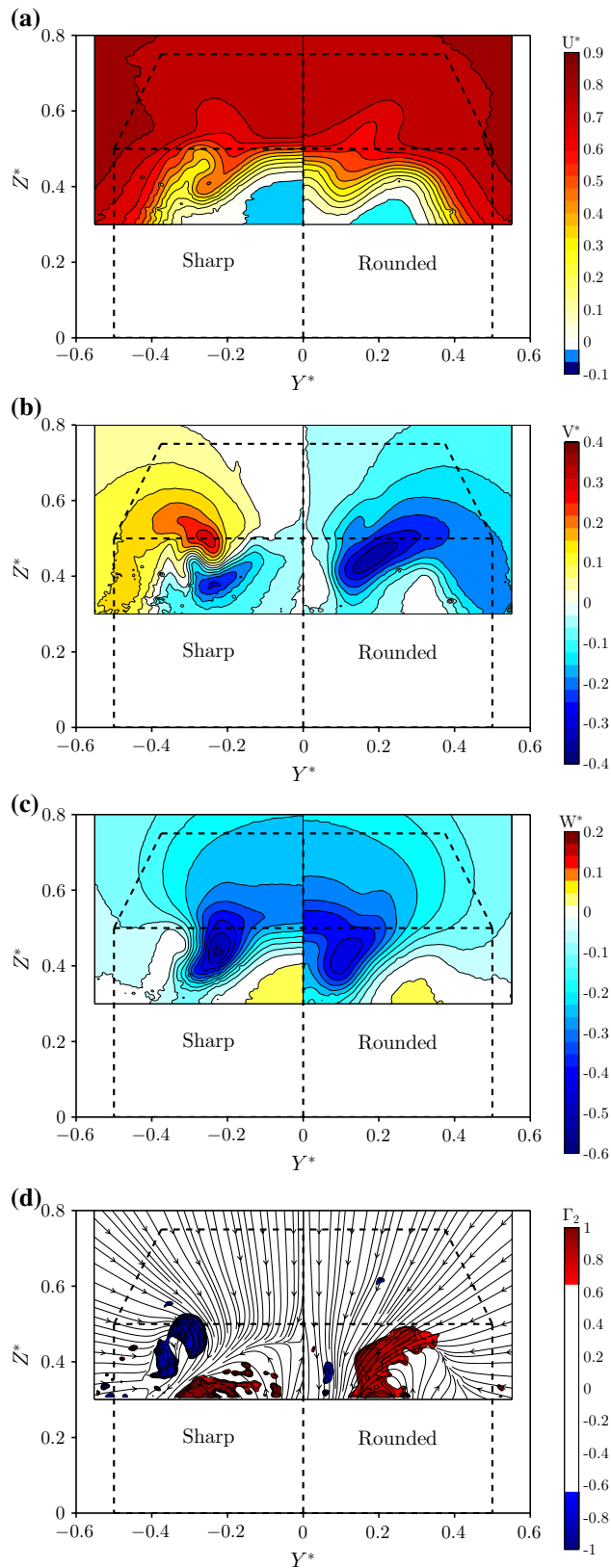


Fig. 18 Plane at $X^* = 0.07$. The *dashed lines* represent the geometry of the model, **(a)** mean streamwise velocity U^* , **(b)** mean spanwise velocity V^* , **(c)** mean normal velocity W^* , **(d)** Γ_2

side of Fig. 18c. Contours of Γ_2 in Fig. 18d illustrate the global streamwise rotation of the flow, expected to induce a low-pressure region over the vertical base of the vehicle.

References

- Ahmed S, Ramm G, Faltin G (1984) Some salient features of the time-averaged ground vehicle wake. Technical report, Society of Automotive Engineers Inc, Warrendale, PA
- Beaudoin J, Aider J (2008) Drag and lift reduction of a 3D bluff body using flaps. *Exp Fluids* 44(4):491–501
- Chassaing P (1990) Turbulence en mécanique des fluides: analyse du phénomène dans une perspective de sa modélisation à l'usage de l'ingénieur
- Conan B, Anthoine J, Planquart P (2011) Experimental aerodynamic study of a car-type bluff body. *Exp Fluids* 50(5):1273–1284
- Davis JP (1982) Wind tunnel investigations of road vehicle wakes. Ph.D thesis, Imperial College London (University of London)
- Fuller J, Passmore MA (2014) The importance of rear pillar geometry on fastback wake structures. *J Wind Eng Ind Aerodyn* 125:111–120
- Graftieaux L, Michard M, Grosjean N (2001) Combining PIV, POD and vortex identification algorithms for the study of unsteady turbulent swirling flows. *Meas Sci Technol* 12(9):1422
- Howell J, Good GL (2008) The effect of backlight aspect ratio on vortex and base drag for a simple car-like shape. SAE
- Howell J, Hickman D (1997) The influence of ground simulation on the aerodynamics of a simple car model. SAE
- Joseph P (2012) Application du contrôle par jets pulsés à un corps non profilé. Ph.D thesis, Université Pierre et Marie Curie-Paris VI
- Joseph P, Amandolèse X, Aider JL (2012) Drag reduction on the 25 slant angle ahmed reference body using pulsed jets. *Exp Fluids* 52(5):1169–1185
- Katz J (1995) Race car aerodynamics: designing for speed (engineering and performance). Bentley Publishers, Cambridge
- Krajnović S, Davidson L (2005) Flow around a simplified car, part 2: understanding the flow. *J Fluids Eng* 127(5):919–928
- Luckring JM (2013) Initial experiments and analysis of blunt-edge vortex flows for VFE-2 configurations at NASA Langley, USA. *Aerosp Sci Technol* 24(1):10–21
- Rossitto G, Sicot C, Ferrand V, Borée J, Harambat F (2014) Influence of the afterbody rounding on the pressure forces of the Ahmed body. In: First international conference in numerical and experimental aerodynamics of road vehicles and trains. *Aerovehicles I*
- Rossitto G, Sicot C, Ferrand V, Borée J, Harambat F (2015) Wake structure and drag of vehicles with rounded rear edges. In: 50th international conference on applied aerodynamics. 3AF
- Tennekes H, Lumley JL (1972) A first course in turbulence. MIT Press, Cambridge
- Thacker A, Aubrun S, Leroy A, Devinant P (2012) Effects of suppressing the 3d separation on the rear slant on the flow structures around an ahmed body. *J Wind Eng Ind Aerodyn* 107:237–243
- Venning J, Jacono DL, Burton D, Thompson M, Sheridan J (2015) The effect of aspect ratio on the wake of the ahmed body. *Exp Fluids* 56(6):1–11

Article 2

Rossitto et al. "Aerodynamic performances of rounded fastback vehicle." Proceedings of the Institution of Mechanical Engineers, Part D: Journal of Automobile Engineering.

Aerodynamic performances of rounded fastback vehicle

Journal Title
XX(X):1–10
© The Author(s) 2016
Reprints and permission:
sagepub.co.uk/journalsPermissions.nav
DOI: 10.1177/ToBeAssigned
www.sagepub.com/



Giacomo Rossitto^{1,2}, Christophe Sicot², Valérie Ferrand³, Jacques Borée² and Fabien Harambat¹

Abstract

Experimental and numerical analyzes were performed to investigate the aerodynamic performances of a realistic vehicle with different afterbody rounding. Afterbody rounding resulted to reduce drag and lift at zero yaw angle, while the crosswind performances were degraded. Rounding the side pillars generated moderate changes in drag and important lift reductions. The minor effect on the drag force was found to result from opposite drag effects on the slanted and vertical surfaces. The vorticity distribution in the near wake was also analyzed to understand the flow field modifications due to afterbody rounding. Crosswind sensitivity was investigated to complete the analysis of the aerodynamic performances of rounded edges models. Additional tests were conducted with geometry modifications as spoilers and underbody diffuser.

Keywords

Rounded edges, Drag, Vorticity, Wake analysis, Crosswind, Spoilers, Underbody Diffuser.

Introduction

For the last decades car manufacturers have been facing the challenging task of reducing fuel consumption and CO₂ emissions. In response to that, optimization algorithms have been applied to generate new vehicle shapes minimizing the aerodynamic drag. Since the obtained optimum shapes has no brand differentiating details, stylists are nowadays trying to give back a brand signature by proposing "non-conventional" shapes. In that framework, important rear pillars rounding becomes a differentiation strategy. The current study suggests to qualify the influence of such afterbody rounding on the flow field and on drag development over a fastback vehicle.

Very few papers have addressed the question of rear edges curvature in aerodynamic vehicle performances. One of the first works was presented by Gilhaus et al. [1] and Howell [2]. Thanks to balance measurements, it was found that rounded pillars reduced drag and rear lift but yawing moment had a pronounced increase. Only recently, advanced techniques were used to achieve better understanding of the afterbody rounding. Thacker et al. [3] showed that rounding the edge between the roof and the rear slant of the Ahmed body results in a 10% drag reduction. Authors attributed this reduction to the fully attached flow over the backlight and the downstream shift of the rotating structures developing in the near wake. Fuller et al. [4] analyzed the benefits of rounding the rear side pillars on the Davis model. They observed that rounded edges generate a different wake structure dominated by the interaction between the longitudinal vortices and the separated region. The rounded edges model resulted in drag and lift reduction of 11% and 25% respectively. The impact of afterbody rounding was mentioned also during the development of the Tesla Model S by Palin et al. [5]. Important curved side pillars were

avoided to reduce highly dynamic wake, which caused large variation in base pressure.

From the literature review, it appears that rounding afterbodies affects considerably aerodynamic loads and flow development, but systematic investigation into the effects of changing radii of side backlight edges was not reported. In complement to the recent study proposed by the same authors in [6] over a simplified car model (Ahmed body), the present study addresses this question on a realistic car model equipped with various rear pillars curvatures. Special care is taken to understand how the modified flow on the backlight interacts with the near wake and promotes drag and lift changes.

Four rear ends were analyzed combining PIV to balance and surface pressure measurements to fully characterize the flow structures and the associated aerodynamic forces. The zero yaw case was first explored before focusing on crosswind effects. Complementary numerical simulations were systematically applied to complete the experimental data and help physical analysis. Geometry modifications, by means of spoilers and underbody diffuser, were investigated to understand their sensitivity to side edges rounding.

¹ PSA Groupe, Velizy-Villacoublay, France.

² Institut Pprime, UPR-3346 CNRS, ENSMA, Université de Poitiers, France

³ Institut Supérieur de l'Aéronautique et de l'Espace (ISAE-SUPAERO), Université de Toulouse, France.

Corresponding author:

Giacomo Rossitto

Email: giacomo.rossitto@ensma.fr

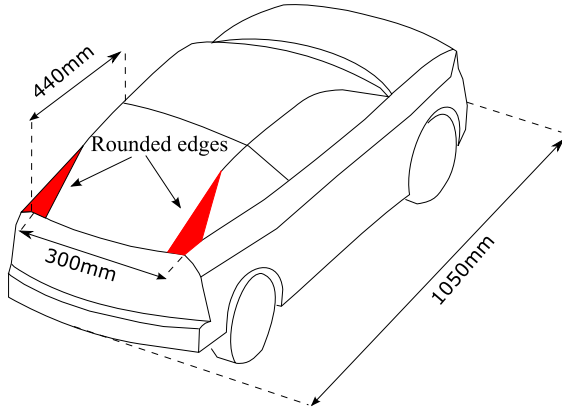


Figure 1. Fastback vehicle model and location of the rounded edges

Experimental and numerical set-up

The model and its relevant dimensions are reported in *figure 1*. Four rear ends are tested, they differ by their side pillars curvature. The curvature radius is given as a percentage of the model span, i.e. 300mm. The model equipped with sharp pillars having 0% radius is referred as S_0 and it is considered as the reference case. The others models are S_8 , S_{20} and S_{40} . All the rear ends have the same curvature at the end of the roof to avoid flow separation. The corresponding radius is chosen to maximize the room for the rear passengers for a fixed backlight angle of 23 degrees. The model features a realistic non symmetric underbody with an exhaust line. It does not have open front air intake. The horizontal projection of the slanted surface, $\xi = 440\text{mm}$, will be used as reference length. Starred spatial coordinates are normalized by the reference length.

The experimental results reported in this work were obtained from tests conducted in the PSA Groupe wind tunnel of La Ferté Vidame. The Eiffel wind tunnel is 52 meters long and has a test section 2 meters high, 5.2 meters large and 6 meters long. It has a maximum free stream velocity of 53 m/s. The wind tunnel blockage ratio was 1.4%. The wind tunnel experiments are conducted with fixed ground and the model is placed over a false floor. All the data were obtained at 40m/s which gives a Reynolds number based on the length of the model of $2.6\text{e}6$. Starred velocities are normalized by the free stream velocity. A six components balance was used to measure the aerodynamic forces acting on the model. The drag and lift coefficients were calculated as follows:

$$C_{d,l} = \frac{F_{d,l}}{\frac{1}{2}\rho U_0^2 S}$$

where F is the force measured by the balance, ρ the density of the air, and S the frontal surface area of the model. The precision of the balance was 0.001 for the drag coefficient C_d and 0.002 for the lift coefficient C_l .

Static surface pressure was recorded by 40 pressure probes over the vertical surface of the rear end. Thirty-five probes were located on the driver side and the rest were located on the passenger side to check the symmetry of the static

surface pressure over the vertical base. Even though the non-symmetric underbody should induced asymmetry in the flow, the comparison between the pressure probes, not reported here for brevity, resulted in negligible differences. Those probes were connected to a SCANDaq 8000 acquisition system. The acquisition rate was 40 Hz for 3000 samples giving 75s of time recording. The static surface pressure coefficient at one point i was computed from the expression:

$$C_P(i) = \frac{P(i) - P_0}{\frac{1}{2}\rho U_0^2}$$

where $P(i)$ is the static pressure of point (i) , P_0 the static pressure measured upstream of the model. The static accuracy of the system is $\pm 13\text{Pa}$, i.e. $0.015 C_p$.

Furthermore, PIV measurements were performed in the wake of the model. The laser sheet was set by a 2*120mJ Nd:Yag Quantum Big Sky Laser. The Dantec Flowsense 4M mkII camera (2024pixel*2024 pixels) equipped with 105 mm lenses generated 462mm*462mm fields of view. 2D PIV was performed on the symmetry (x,z) plane $Y^*=0$. For all the PIV measurements, post-processing was performed with a final interrogation window of 16*16 pixels, after an initial window of 32*32 pixels, with an overlap of 50% in horizontal and vertical directions. The grid spacing was 1.82mm. A SNR filter was applied to remove vectors with $\text{SNR} < 1.2$. 900 images were recorded with a 7Hz trigger rate. With this setting, the 95% confidence limit represents approximately $\pm 3\%$ of the mean velocity [7].

The numerical simulations presented in this work were computed with the commercial code *PowerFLOW*® (version 5.0c) based on lattice Boltzmann model. Applications of lattice Boltzmann method to vehicles aerodynamics can be found in [8] and [9]. The simulation setting is reported in *table 1*. The model size for the numerical simulations corresponds to a real vehicle scale. At Reynolds $1.04\text{e}7$, 324000 time-steps were computed (3 seconds of real time). Local variable refinement regions VRs were defined to locally allow coarsening the grid by a factor of 2 starting from the *Minimum Level of VR* [8]. The minimum value of VR (*table 1*) corresponds approximately to 300 wall units. The computational grid consisted of 1.2 million volume elements and 0.6 million surface elements. The computational domain was chosen according to PSA methodology. The model is positioned 17.5L from the domain inlet and the total length of the computational domain is 35L (L is the model length). In the following, temporally averaged velocity and pressure fields will be shown. These averages are computed over approximately 25 convective time scales L/U_0 where U_0 is the external velocity.

This setting allowed good agreements between numerical and experimental results, as it is possible to examine in *figure 3* that reports a comparison of mean streamwise velocity profiles.

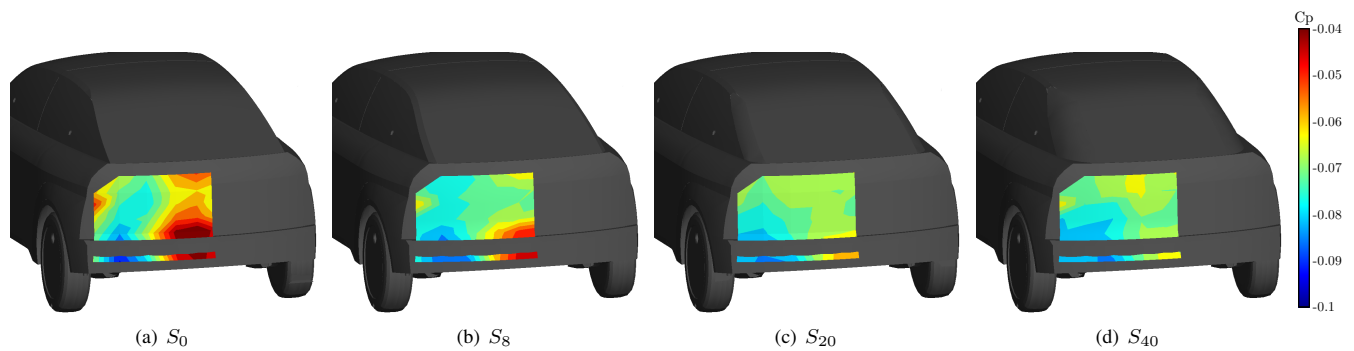


Figure 2. Experimental surface pressure coefficient distribution over the vehicle base.

Table 1. Numerical *PowerFLOW*® setting

| | |
|-----------------------|-------------------------------|
| Physical Time Scaling | 1 timestep = $9.308e - 06sec$ |
| Minimum Level of VR | VR 9 ($2.50e-03$ m/voxel) |
| Simulation time | 324000 timesteps (3 sec) |
| Reynolds | $1.04402e+07$ |

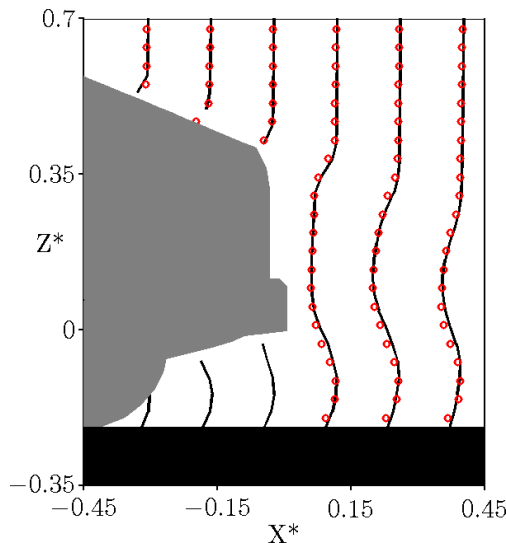


Figure 3. Comparison between numerical and experimental results. Mean streamwise velocity profiles. \circ Experimental, — Numerical

Base Geometry flow analysis

This section analyzes the mean properties of the flow field modifications due to afterbody rounding. At first, the zero yaw flow field and forces are analyzed. At the second stage, the crosswind performances are investigated.

Table 2 reports the variation of aerodynamic coefficients and averaged base pressure with respect to the reference case S_0 . Increasing the side radius generates a small drag reduction and significant lift reduction. For the S_0 configuration, most of the rear lift is generated over the rear end by the low value of pressure over the curved roof edge and from the low pressure foot-print of the longitudinal vortices, the so-called C-pillar vortices (see figure 10(a)). These vortices are generated by the interaction of the flow coming from

the side of the model and the flow over the rear window. Since the roof radius is constant among the four models, lift reductions are caused by the C-pillar vortices intensity modifications due to side rounding. For a moderate value of C-pillars rounding, the origin of the longitudinal vortices is displaced towards the base of the body along the C-pillars [6]. For larger rounding, three-dimensional flow separation does not occur anymore on the side of the model and thus the side vortices disappear [10]. The weakening of the C-pillar vortices allows a pressure recovery over the rear window reducing its contribution to drag and lift. However, the variation of the average base pressure over the vertical surface, reported in figure 2 and in table 2, gives evidence that the base pressure is reduced when the curvature side radius is increased. For S_{40} , the base pressure is 17% lower than for S_0 , resulting in an important local drag increase. This effect counter-balances the local drag reduction of the rear window and can explain the weak effect of pillars rounding on the global drag (table 2).

Table 2. Variation of aerodynamic coefficients and averaged base pressure relative to S_0 .

| | ΔC_d | ΔC_l | ΔC_p Base |
|----------|--------------|--------------|-------------------|
| S_0 | - | - | - |
| S_8 | 0% | -13% | -12% |
| S_{20} | -1.5% | -18% | -15% |
| S_{40} | -2% | -27% | -17% |

The mean velocity fields in the symmetry plane are reported in figure 4. It was chosen not to report the intermediate configurations, i.e. S_8 and S_{20} , to focus on the main differences between the most rounded rear pillar model S_{40} and the sharpest one S_0 . The symmetry plane is far from sufficient to describe the entire topology of the tridimensional near wake, nevertheless it is very useful to get a first hint of the changes made by side rounding. Over the rear window, no major differences are noticed between the two models. The flow is attached to the slanted surface due to the important roof radius for both models. For S_0 , the average separated zone in the close wake is characterized by two counter-rotating structures. The mean recirculating length, identified by the saddle point of the 2D mean streamlines, is at $X^* = 0.33$ and $X^* = 0.23$ respectively

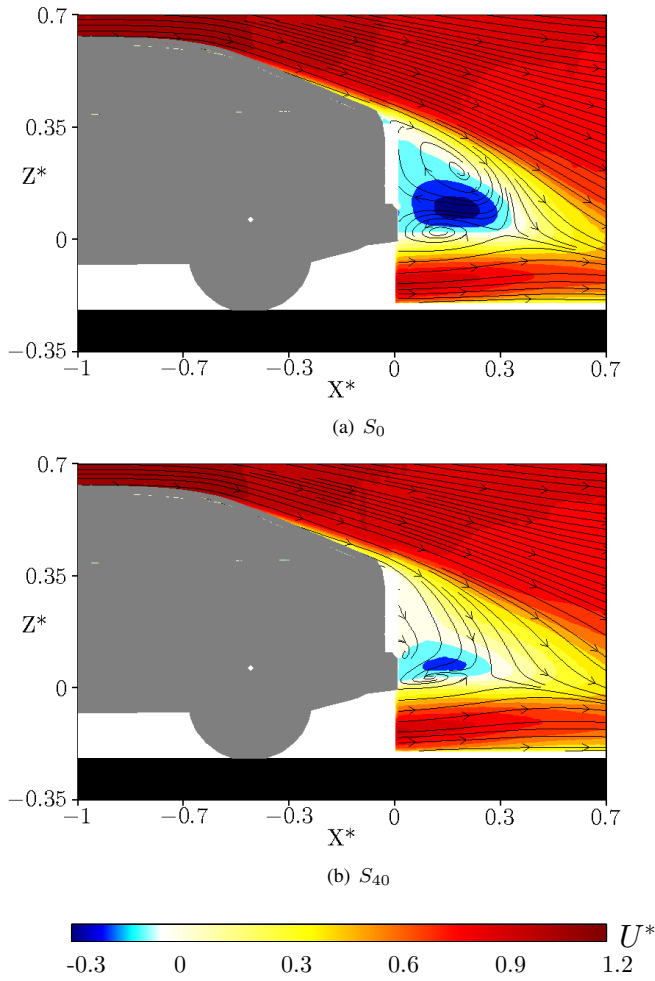


Figure 4. Time averaged streamlines and mean streamwise velocity U^* at $Y^*=0$.

for S_0 and S_{40} . Adding pillar curvature reduces then the length of the near wake and modifies the topology of the enclosed structures. For S_{40} , the mean curvature of the near wake is increased due to important negative normal velocity. Regarding the flow organization inside the near wake, the upper structure is not evidenced anymore and the lower structure seems to be reduced. Such a strong modification of the near wake properties in the symmetry plane, may result from a 3D modification of the flow field due to side rounding.

To understand this complex mechanism, cross-flow planes are displayed in *figure 5*. The data are issued from the numerical simulations. Each picture is divided in two: the left side represents S_0 and the right side S_{40} . At $X^*=0.02$, right after the rear slant, the longitudinal vorticity ($\Omega_x^* = \frac{\Omega_x \cdot \xi}{U_0}$) is concentrated in the C-pillar vortex for S_0 (left part of top of *figure 5*). At the same X plane, a diffuse horizontal small area of longitudinal vorticity is present for S_{40} located in the shear layer (right part of top of *figure 5*). Two-dimensional lines tangent at each point to the vector (V, W) are also drawn in *figure 5* to underline the different organization of flow fields due to afterbody rounding. At $X^*=0.23$, i.e. the S_{40} saddle point location, the overall longitudinal rotation of the

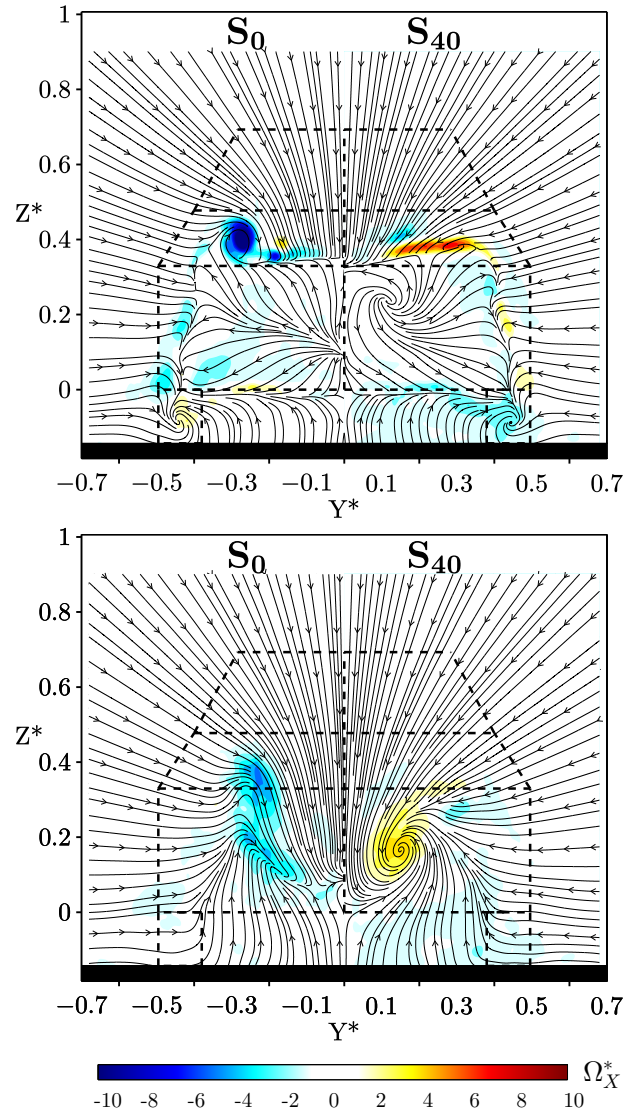


Figure 5. Mean Streamwise Vorticity Ω_x^* . Top $X^*=0.02$, bottom $X^*=0.23$. Left S_0 , Right S_{40} .

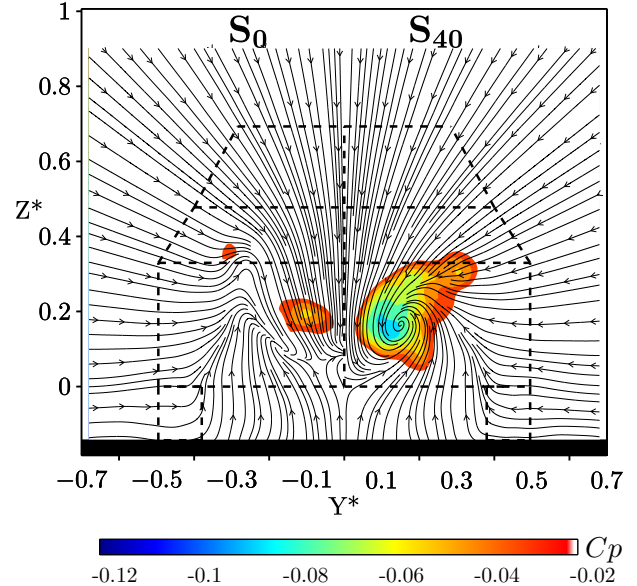


Figure 6. Mean pressure coefficient C_p at $X^*=0.23$. Left S_0 , Right S_{40} .

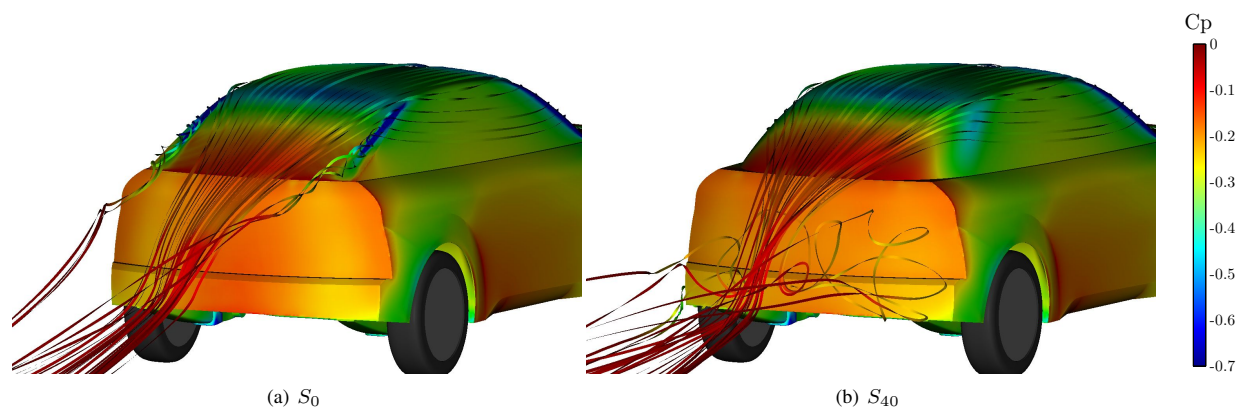


Figure 7. Time averaged streamlines from numerical simulations. The streamlines and the surface of the body are colored by the pressure coefficient C_p

S_{40} near wake is showed in the bottom of figure 5. The high spanwise and vertical velocity associated to the transversal flow in S_{40} , therefore results in a global longitudinal rotation of the flow in the near wake. To quantify the rotation of the flow, the longitudinal evolution of the mean circulation $\Gamma^* = \int_{S^*} \Omega_x dS$ was analyzed as in the work of Rossitto et al. [6]. The domain of the calculation included all the numerical domain presented in figure 5. Despite the high levels of vorticity of the C-pillar vortices for S_0 , the overall circulation is higher for S_{40} . At $X^* = 0.23$, Γ^* for S_{40} is 30% higher than S_0 . The flow overcoming the rounded edge results then in a notably 3D organization characterized by a large scale rotation around the longitudinal axis. The longitudinal rotation, as reported in figure 6, generates a lower pressure for S_{40} respect to S_0 , consistently with the surface pressure measurements analyzed previously in figure 2 related to the local base drag increase.

To help to visualize the tridimensional flow modifications due to afterbody rounding, streamlines from numerical simulation are reported in figure 7. Consistently with the cross-flow visualizations, it can be noticed the presence of the C-pillar vortices for the S_0 thanks to the low pressure foot-print of the vortices. The sharp side pillars force the lateral flow to separate, generating longitudinal vortices. As analyzed by the same authors in [6], it is suggested that, for S_0 , the sharp lateral edges "shield" the wake separation region at the base and enable a "two-dimensional" separation, "2D" meaning that the mean streamlines at separation are more parallel to the orientation of the flow over the window, while longitudinal vorticity is concentrated in the C-pillar vortices. On the contrary, for rounded edges, the flow is drawn in from the sides, toward the center over the slanted surface. The separation at the base is then notably 3D for S_{40} , associated with high spanwise and vertical velocity components.

Crosswind

To gain further insight on the influence of afterbody rounding on the aerodynamic performances, crosswind tests were performed. A sketch of the crosswind aerodynamic characteristic is drawn in figure 8. In the present experiments, the yaw angle β varied from -30° to 30° and the wind tunnel speed was 40m/s. All the aerodynamic coefficients

are scaled by the same frontal surface area as usual in the study of crosswind characteristic [11]. The model being symmetric, only the results in $[-30^\circ; 0^\circ]$ are reported. The choice of such large range of angles is motivated in what follows. Due to meteorological phenomena, small angles of crosswind have a non negligible probability of exceedance. As reported by Palin et al. [12], the majority of possible yaw angles are within the band of zero to 10 degrees, which covers more than 99% of the probability distribution. The study of this interval permits then to complete the aerodynamic performance analysis of the model. Angles in $[-30^\circ; -20^\circ]$ are tested mostly for safety reasons. Even though the natural probability of exceedance of such angles is extremely rare, they can occur due to driving condition as overtaking [13] or extreme weather conditions [14].

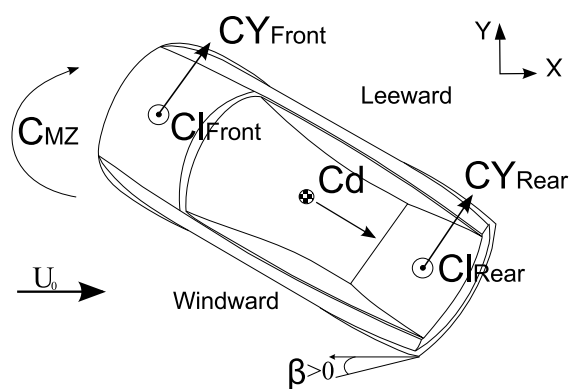


Figure 8. Sketch of crosswind aerodynamic characteristics

The yawing moment is generated by the front and rear contribution of the side forces. It is computed by using the middle of the wheelbase and truck as a reference. The modification of the side pillars radii being in the model rear end, the analysis will be focused on the generation of the rear forces, i.e. Cy_{rear} and Cl_{rear} . The overall drag will be discussed as well. Figures 9 reports experimental aerodynamic coefficients in $[-30^\circ; 0^\circ]$ yaw angles. The starred coefficients are normalized by the value of S_0 at -30° . As a general trend, drag experiences almost 30% of

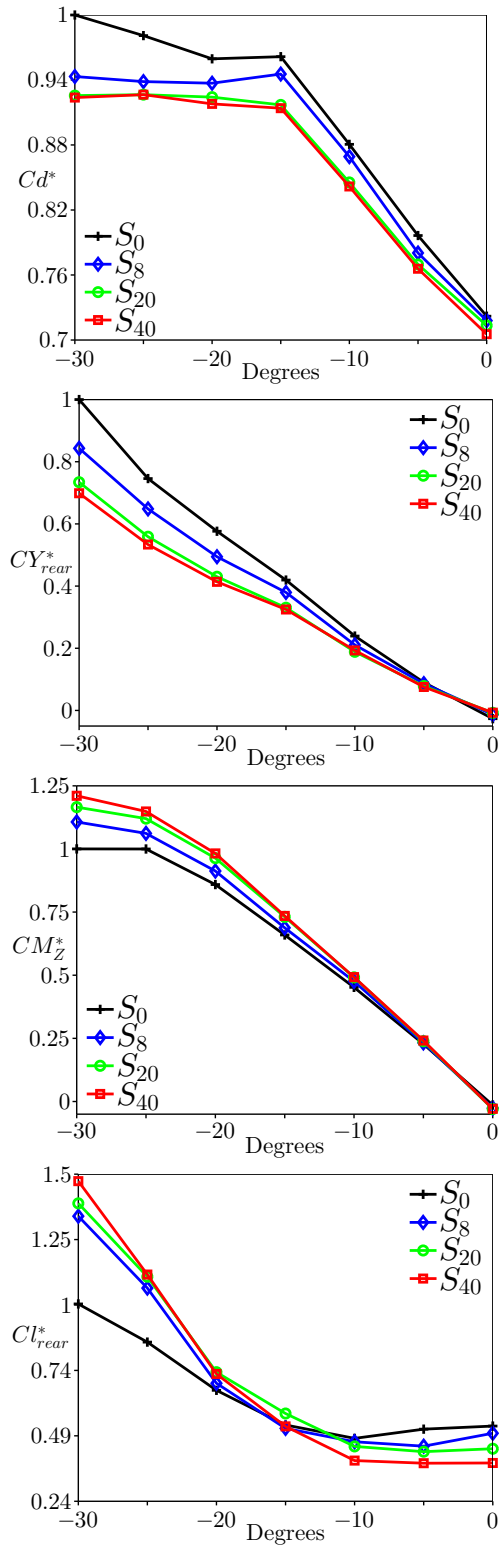


Figure 9. Normalized aerodynamic coefficients. From top to bottom: Cd^* , CY_{rear}^* , CM_Z^* , Cl_{rear}^*

increase in $[-15^\circ; 0^\circ]$. At -5° and -10° of yaw angle, S_{40} drag is respectively 3.5% and 4.5% lower than to S_0 . The drag increase due to yaw angle increasing is more important for the sharp side pillar. Moreover while drag is constant

in $[-30^\circ; -20^\circ]$ for the rounded models, it continues to increase for S_0 .

Since yaw angles do not have the same probability of occurrence, many authors have performed their performance analysis in terms of wind average drag coefficient as Buckley et al. [15] and Cooper [16]. Tacking into account the yaw angles probability distribution proposed by [12], S_{40} averaged drag in $[-10^\circ; 0^\circ]$ is 3% lower than S_0 .

CY_{front} , not shown here, does not have important differences among the four rear ends. On the contrary, CY_{rear} experiences significant changes. S_{40} side rear force is 20% and 30% lower than S_0 respectively at -10° and -30° . It is important to notice that CY_{rear} acts as a counter-rotating force to the yawing moment (figure 8). This means that, reducing the side rear force, induces the increase of yawing moment. The value of the yawing moment CM_Z , grows then with an increasing C-pillar radius. At -30° , S_{40} yawing moment is 21% higher than S_0 . It is interesting to notice that S_8 , featuring a very small side radius, resulted already in 12% CM_Z increase with respect to S_0 . It results then that the yawing moment has a pronounced increase as soon side edges features a small radius [2].

Howell et al. [17] analyzed the relationship between lift and lateral aerodynamics. According to them, when the rear lift is reduced, there is often a reduction in yawing moment. However, the use of rounded edges does not follows this pattern since the model with the lowest lift at zero yaw angle results to have the highest yawing moment. The rear lift in $[-10^\circ; 0^\circ]$ is alike 0° yaw angle: the S_{40} model has lower rear lift compared to S_0 due to the C-pillar vortices and their induced flow elimination over the rear window (-27% at 0° yaw angle). Interesting inversion of the behavior appears for yaw angles bigger than -15° . The rounded models experience a sudden growth of rear lift (+47% at -30° yaw angle) due to the flow acceleration around the rounded rear pillar, creating a strong suction on the windward side of the model [18]. On the contrary, the windward side sharp edge of S_0 , promotes flow separation over the rear window, resulting in moderate growths of rear lift compared to the rounded model. The differences in the yawing moment can be explained by the different pressure distributions over the model, reported in figure 10.

The top view of the numerical pressure distributions at 0 yaw angle are reported to show the rear pressure characteristics. The C-pillar vortices pressure foot-prints is clearly remarked over the side sharp pillar for S_0 (figure 10(a)). At $\beta = -30^\circ$, C-pillar vortices disappear due to the flow separation imposed by the windward sharp edge. Strong acceleration over the windward rounded edge is visible for S_{40} thanks to the important pressure decrease over the edge (figure 10(d)). Side views are reported in figures 10(e)-10(h) to complete the pressure distribution analysis. In fact, not only the windward side, i.e. the suction over rounded C-pillar, contributes to the overall yawing moment. It is interesting to notice that, on the leeward side, the reduced pressure foot-print of the vortex generated at the forebody and the pressure recovery over the rounded C-pillar contribute to the yawing moment increase. Figure 11 reports an horizontal pressure profile over the vehicle as in the work of Howell [19]. Those plots quantify

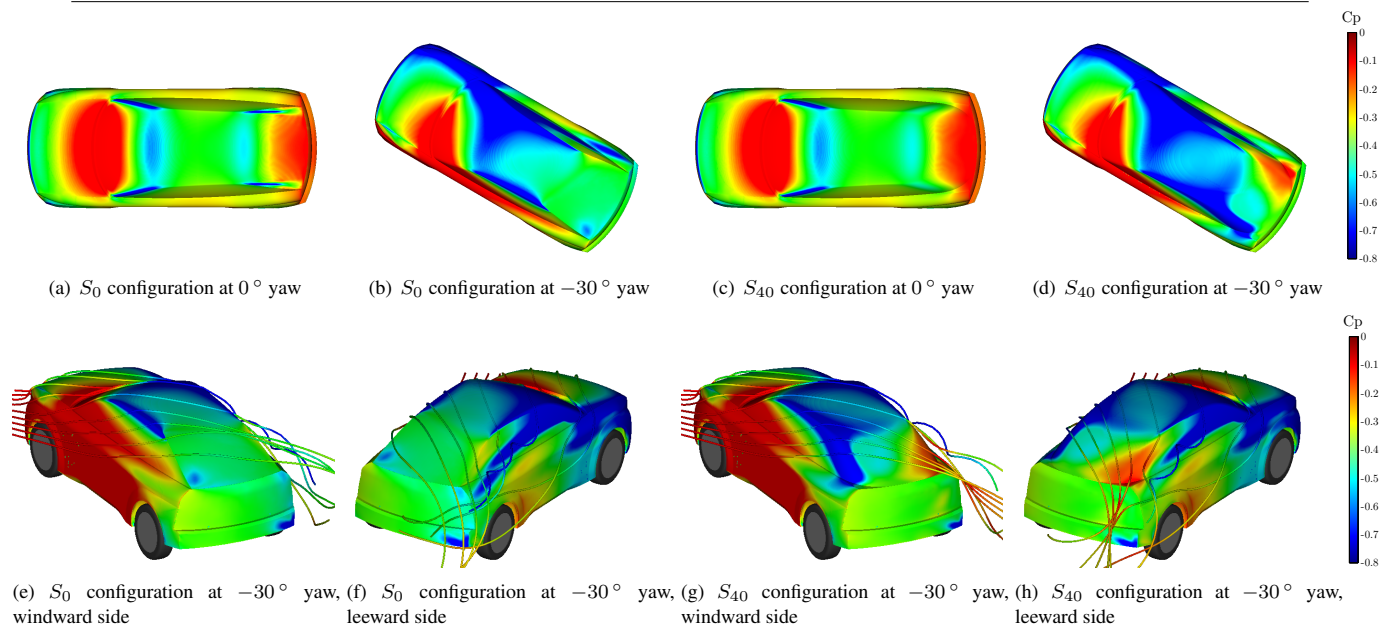


Figure 10. Surface pressure and streamlines visualizations from numerical simulations.

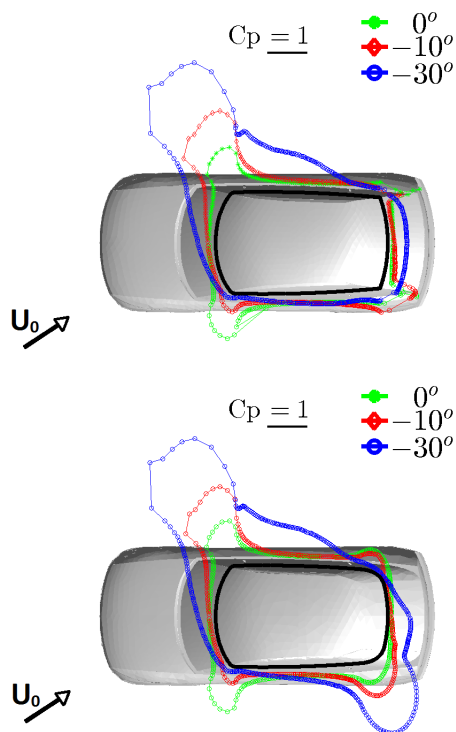


Figure 11. Pressure distribution at $Z^* = 0.43$: Top S_0 , Bottom S_{40} . Values outside the solid black line correspond to negative pressure coefficient

the effects of the rear slant pressure to the yawing moment. Values outside the solid black line are negative. For S_0 , the contribution to the yawing moment derives mainly from the leeward front part. Moreover this contribution is constant for both models. For S_{40} , the windward rear side low pressure is visible due to the rear peak outside the solid black line. The differences between the two models plots underline the origin of the increased yawing moment for S_{40} .

Geometry modifications

Spoilers

Rear spoilers are undoubtedly efficient devices to increase vehicles downforce in race cars [20]. Nowadays, small spoilers are used in commercial vehicles to modify the near wake flow field. To investigate the influence of afterbody rounding on the efficiency of rear spoilers, additional experiments are presented in what follows. In this tests, three different spoilers at the rear slant end where used. The size of the spoilers, their placement and their shape are chosen by the PSA style department. In fact, small devices that extend the rear slant line are an interesting solution for both style and aerodynamic performances. The position of the spoilers and their numbering is reported in figure 12.

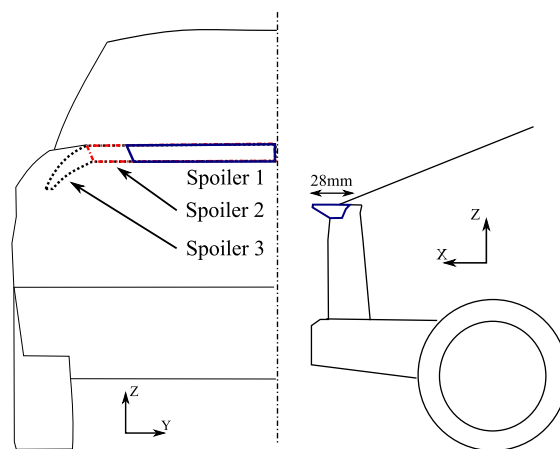


Figure 12. Spoilers location over the model. Spoiler2 includes spoiler1 and spoiler3 includes spoiler2

Regarding the flow modifications generated by the use of such devices, a pressure recovery is expected upstream

the spoiler. It results in a rear slant drag reduction. This effect, coupled with the high pressure over the spoiler itself, contributes to the overall drag and lift reductions. The spoiler allows also base drag reduction due to modification of the near wake close to the vehicle base. If the mechanisms associated with rear spoilers are well known and understood [21], the interactions with the flow modifications generated by rounded side pillars have not been investigated yet.

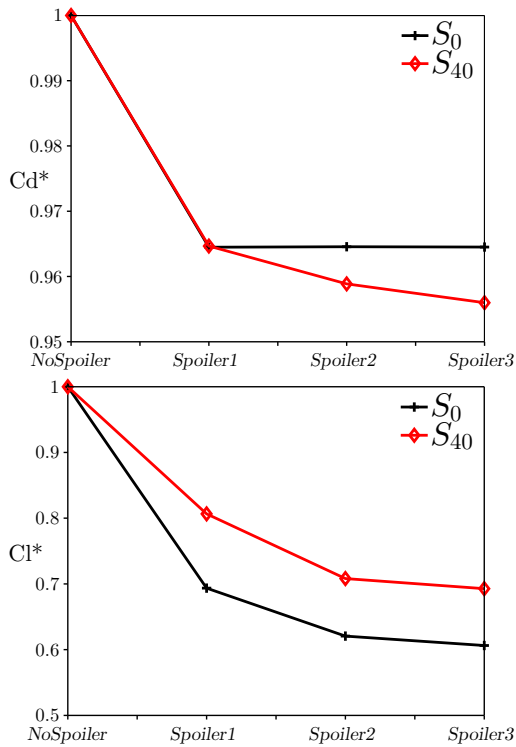


Figure 13. Normalized aerodynamic coefficients for the different rear spoiler configurations. Top: drag coefficient, bottom: lift coefficient

The normalized aerodynamic coefficients relative to the different rear spoiler configurations are reported in figure 13. They are normalized by the values of the model without spoiler, referred as *NoSpoiler*. *Spoiler1* generates the same drag reduction for both S_0 and S_{40} , i.e. 3.5% with respect to *NoSpoiler*. Increasing the size of the spoiler does not further reduce drag for S_0 . On the contrary, S_{40} with *spoiler3*, experiences drag reduction up to 4.5% compared to S_{40} without spoiler. Regarding the relative comparison between the two models with *spoiler3*, drag is 3% lower for S_{40} with respect to S_0 . As previously explained, rounding the edges resulted in a local increase of base drag. Furthermore, in the 2D analysis of the flow field, figure 4, the shortening of the near wake, imposed by the side flow downwash, was related to the base drag increase. In terms of drag, the use of spoilers placed at the rear slant end, is then more effective when the near wake length is not optimal as for S_{40} .

Regarding the lift, *spoiler1* impacts strongly S_0 rather than S_{40} . In fact, *spoiler1* generates 30% lift reduction for S_0 and only 20% for S_{40} . The S_0 model with *spoiler3*, experiences lift reduction up to 40% compared to the same model without

spoiler. Despite this important reduction, the overall lift coefficient for S_{40} is still 15% lower than S_0 . As a matter of fact, the lift without spoiler for S_{40} is 27% lower than S_0 as reported in table 2. The higher lift reduction for S_0 can be related to the presence of the C-pillar vortices due to the sharp side edges. The spoilers, promoting a pressure recovery over the rear window, impact directly the strength of those vortices, resulting in an important lift reduction.

As a general trend, spoilers are able to reduce the negative local effects generated by the side pillar edges. They are then more efficient in terms of drag reduction for models with rounded rear edges. Regarding the lift, spoilers are suitable passive devices to improve lift reduction for sharp rear edge models.

Diffuser

Underbody diffuser is commonly used in racing cars to develop large downforce. Recently, diffusers have become a good strategy for drag and lift reduction even for passenger cars [22]. Three different mechanisms contribute to produce high levels of downforce and drag reduction in a passenger car. The first mechanism is due to the ground interaction. By placing the body in ground proximity, the acceleration of the flow underneath the body will reduce the underbody pressure resulting in a downforce (i.e. negative lift) [23]. The second mechanism generating downforce is related to the upswEEP of the rear underbody. The angle of the diffuser will camber the flow resulting in a local pressure reduction around the diffuser edge. The last principle, is commonly referred as “diffuser pumping”. As the ratio of the inlet to outlet area increases, pressure recovery is performed in the diffuser area. Given that the near wake pressure remains constant, the pressure upstream the diffuser decreases and the underbody flow rate increases. These effects result in further decrease in underbody pressure, which produce the “pumping down” [24].

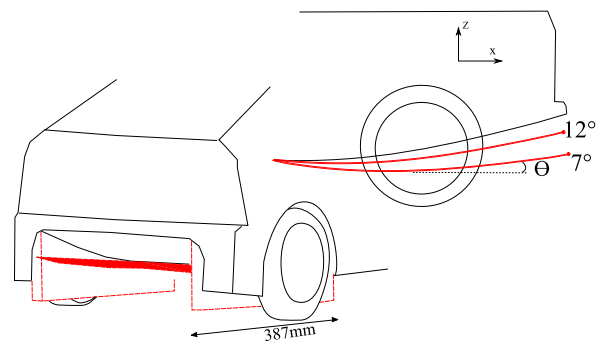


Figure 14. Schematics of the underbody diffuser. The side view in the top shows the maximum and minimum diffuser angles tested.

The diffuser used in these experimental tests was produced by means of 3D printer. A flat underbody was used here instead of the realistic underbody used for the previous tests. The underbody featured already a diffuser angle of $\Theta=15$ degrees. The schematics of the underbody diffuser are drawn in figure 14. The underbody used was made from a thin

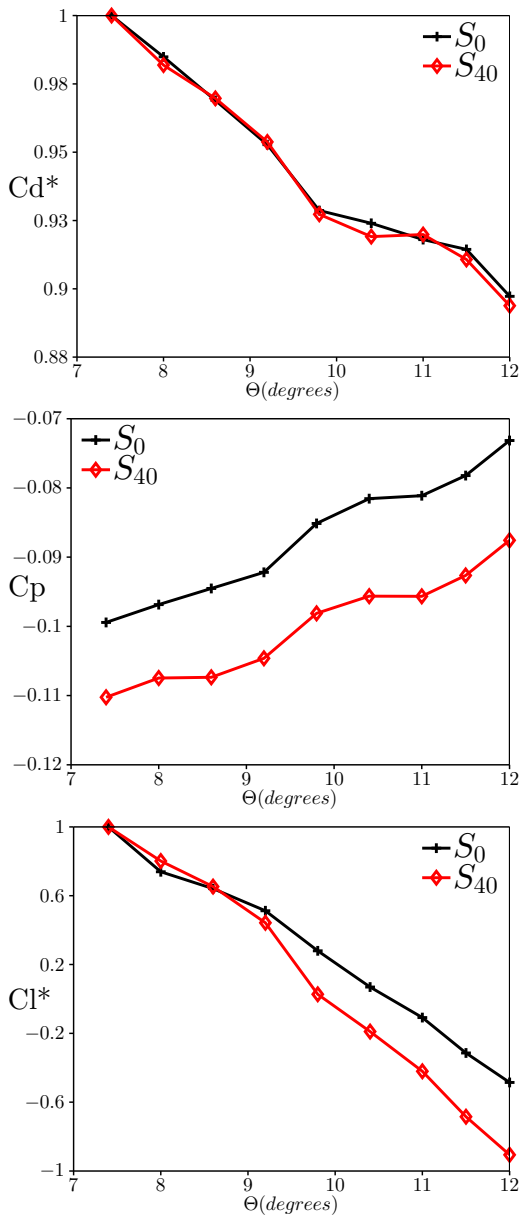


Figure 15. Normalized aerodynamic coefficients for underbody diffuser angles variation. Top: drag coefficient, center: averaged base pressure, bottom: lift coefficient

cambered plate reproducing the original diffuser shape. Its angle variation had several limitations. Since the original diffuser was not flat but featured a convex shape, reducing the angle Θ increased the frontal surface of the model. For that reason the minimum angle tested was 7 degrees that results in a frontal area variation of approximately 2%. All the aerodynamic coefficients are rescaled to take into account the area variation. Moreover the maximum angle was limited to 12 degrees due to the hinge limitation of the diffuser. The diffuser was fitted with side plates as in the works of Cooper et al. [25] to prevent flow overcoming the side of the diffuser and to provide fixation for the diffuser sides.

The starred aerodynamic coefficients are normalized by the value at 7 degrees for each model. Drag evolution for diffusers angles variation is reported in the top of figure 15.

The diffuser drag reduction is the same for both models. Increasing the diffuser angle, from 7 to 12 degrees, results in drag reduction up to 10% for both models. At 12 degrees, S_{40} drag is 1.5% lower than S_0 . This is consisted with the base geometry trends reported in table 2. The averaged base pressure, reported in the center of figure 15, increases as well for increasing diffuser angles, in accord with the drag reduction. It is quite striking to notice how the plots are “parallel”. The gap between the lines seems to be imposed then by the side radius and remain then constant for all diffuser angles.

The bottom of figure 15 reports the lift evolution. As expected by the use of the diffuser, increasing its angle results in downforce, i.e lift reduction. The lift for both models is canceled out. The lift reduction is the same for both models from 7 to 9 degrees. For diffuser angles greater than 9 degrees the lift reduction is more effective for the rounded model. For S_{40} , the upsweep of the diffuser should makes the wake more symmetrical with respect to flow structures organization reported in figure 4. For S_0 , since the reference wake was already symmetric, it is suggested that high diffuser angle tends to break the symmetry for S_0 resulting in a wake directed upwards. It could explain that high diffuser angles for S_0 has moderate lift reduction with respect to S_{40} [22].

Conclusions

Experimental and numerical analyzes were used to study the influence of afterbody rounding on the aerodynamic characteristics of a fastback vehicle model. At zero crosswind, rounded edges resulted having minimal impact on drag due to opposite effects over the rear slant and the base. Important lift reduction were achieved thanks to the elimination of the C-pillar vortices. The impact of rounded edges on the near wake organization due to the different longitudinal vorticity distribution was highlighted. Unfortunately, rounded edges resulted in a detriment of the lateral stability, generating a severe increase of yawing moment and rear lift. Geometry modifications were also tested to study their efficiency variation due to side rounding. Spoilers resulted to recover the negative base drag effects of side rounding. The lift reduction was much more effective for sharp rear edge. Regarding the use of diffuser, the overall drag modifications due to diffuser angles variations were not sensitive to afterbody rounding. Lift force is found to be more sensitive to high diffuser angles for the rounded edge model.

This analysis helps for future vehicles efficient design giving the overall aerodynamic behavior of afterbody rounding. Innovative design should take into account the right balance between sharp and rounded edge since they resulted to have different performances with respect to yaw angles. Additional tests should be performed to study the effects of a non-constant side radius to find an optimal compromise in terms of drag, lift and lateral stability.

Acknowledgements

The authors are thankful to B. Tixier from the Exa company for performing the numerical simulations and to Y. Goraguer, the wind tunnel manager, for his time and efforts during the experimental tests. We acknowledge the PSA designer Yong Wook Sin for the fruitful collaboration.

This work has been performed in the framework of the "OpenLab Fluidics" @Poitiers.

References

- [1] Gilhaus AM, Renn VE. Drag and driving-stability-related aerodynamic forces and their interdependence—results of measurements on 3/8-scale basic car shapes. SAE Technical Paper; 1986.
- [2] Howell J. Shape features which influence crosswind sensitivity. C466/036. 1993;9(1):43–43.
- [3] Thacker A, Aubrun S, Leroy A, Devinant P. Effects of suppressing the 3D separation on the rear slant on the flow structures around an Ahmed body. Journal of Wind Engineering and Industrial Aerodynamics. 2012;107:237–243.
- [4] Fuller J, Passmore MA. The importance of rear pillar geometry on fastback wake structures. Journal of Wind Engineering and Industrial Aerodynamics. 2014;125:111–120.
- [5] Palin R, Johnston V, Johnson S, D’Hooge A, Duncan B, Gargoloff JJ. The Aerodynamic Development of the Tesla Model S-Part 1: Overview. SAE Technical Paper; 2012.
- [6] Rossitto G, Sicot C, Ferrand V, Borée J, Harambat F. Influence of afterbody rounding on the pressure distribution over a fastback vehicle. Experiments in Fluids. 2016;57(3):1–12.
- [7] Benedict L, Gould R. Towards better uncertainty estimates for turbulence statistics. Experiments in fluids. 1996;22(2):129–136.
- [8] Fares E. Unsteady flow simulation of the Ahmed reference body using a lattice Boltzmann approach. Computers & fluids. 2006;35(8):940–950.
- [9] Duncan BD, Sengupta R, Mallick S, Shock R, Sims-Williams D. Numerical simulation and spectral analysis of pressure fluctuations in vehicle aerodynamic noise generation. SAE Technical Paper; 2002.
- [10] Rossitto G, Sicot C, Ferrand V, Borée J, Harambat F. Wake structure and drag of vehicles with rounded rear edges. In: 50th International Conference on Applied Aerodynamics. 3AF; 2015. p. 1.
- [11] Hucho Wh, Sovran G. Aerodynamics of road vehicles. Annual review of fluid mechanics. 1993;25(1):485–537.
- [12] Palin R, Rebbeck L, Gargoloff J, Duncan B. Alternative Simulation Methods for Assessing Aerodynamic Drag in Realistic Crosswind. SAE Paper. 2014;p. 2014–01–0614.
- [13] Noger C, Regardin C, Szechenyi E. Investigation of the transient aerodynamic phenomena associated with passing manoeuvres. Journal of fluids and structures. 2005;21(3):231–241.
- [14] Baker C, Reynolds S. Wind-induced accidents of road vehicles. Accident Analysis & Prevention. 1992;24(6):559–575.
- [15] Buckley FT, Sekscienski WS. Comparisons of effectiveness of commercially available devices for the reduction of aerodynamic drag on tractor-trailers. SAE Technical Paper; 1975.
- [16] Cooper KR. Truck aerodynamics reborn: lessons from the past. SAE transactions. 2003;112(2):132–142.
- [17] Howell J, Fuller JB. A relationship between lift and lateral aerodynamic characteristics for passenger cars. SAE Technical Paper; 2010.
- [18] Cairns RS. Lateral aerodynamic characteristics of motor vehicles in transient crosswinds. Cranfield University. 1994;.
- [19] Howell J. The side load distribution on a Rover 800 saloon car under crosswind conditions. Journal of wind engineering and industrial aerodynamics. 1996;60:139–153.
- [20] Katz J. Aerodynamics of race cars. Annu Rev Fluid Mech. 2006;38:27–63.
- [21] Fukuda H, Yanagimoto K, China H, Nakagawa K. Improvement of vehicle aerodynamics by wake control. JSAE review. 1995;16(2):151–155.
- [22] Marklund J, Lofdahl L, Danielsson H, Olsson G. Performance of an automotive under-body diffuser applied to a sedan and a wagon vehicle. SAE International Journal of Passenger Cars-Mechanical Systems. 2013;6(1):293–307.
- [23] Barlow JB, Guterres R, Ranzenbach R. Experimental parametric study of rectangular bodies with radiused edges in ground effect. Journal of Wind Engineering and Industrial Aerodynamics. 2001;89(14):1291–1309.
- [24] Cooper KR, Bertenyi T, Dutil G, Syms J, Sovran G. The aerodynamic performance of automotive underbody diffusers. SAE Technical Paper; 1998.
- [25] Cooper KR, Syms J, Sovran G. Selecting automotive diffusers to maximise underbody downforce. SAE Technical Paper; 2000.

Influence of afterbody rounding on the aerodynamics of a fastback vehicle

Keywords : Wakes, Automobiles-Aerodynamics, Drag, Turbulence.

For the last decades car manufacturers have been facing the challenging task of reducing fuel consumption and CO₂ emissions. In response to that, optimization processes have been applied to generate new vehicle shapes minimizing the aerodynamic drag. Since the obtained optimal shapes have no brand differentiating details, stylists are nowadays trying to give back a brand signature by proposing "non-conventional" shapes characterized by important rear pillars rounding. The present PhD work experimentally quantifies the influence of such afterbody rounding on the aerodynamic loads and on the flow field development over fastback vehicle models. Rounding the roof/backlight of the well-known Ahmed body intersection is shown to reduce drag. Surprisingly, additional rear curvature associated with side pillars rounding does not further modify the drag. However, the zero net effect is found to result from opposite drag effects. To further increase the complexity and fidelity of the model, a model is realized in partnership with the style department of PSA. Crosswind sensitivity is also investigated by means of yaw angle variation. It is shown that the rear ends with rounded edges deteriorate the lateral aerodynamics. The understanding of the afterbody rounding effects is shown to be valid even for increasing complexity of the models. Finally, full scale test confirms the trends observed with the scaled models.

Influence de montants arrières arrondis sur l'aérodynamique des véhicules bicorps

Mots clés: Sillage, Automobiles, Trainée, Tourbillons.

Pendant les dernières décennies les constructeurs automobiles ont été confrontés à la tâche difficile de réduire la consommation de carburant et les émissions de CO₂. En réponse à cela, des processus d'optimisation ont été appliquées pour générer de nouvelles formes de véhicule pour réduire la trainée aérodynamique. Malheureusement, les formes optimales obtenues n'ont aucun signe distinctif pour se différencier entre les différentes marques. Les stylistes tentent aujourd'hui de redonner une signature de marque en proposant des formes *non-conventionnelles* caractérisés par des montants arrières fortement arrondis. Ce travail de thèse quantifié expérimentalement l'influence des montants arrondis sur l'aérodynamique des véhicules bi-corps (fastback). Rayonner l'arrêt entre le pavillon et la lunette du corps d'Ahmed s'avère efficace pour réduire la trainée. Ajouter un rayon de courbure sur les montants arrière latéraux ne modifie pas davantage la trainée. Cependant, l'effet net nul sur la trainée est dû à des modifications de trainée opposée. L'organisation du sillage proche et le transport de vorticit  ont  t  analys s et reli    l'augmentation locale de la train e. Pour augmenter encore la complexit  et de la fid lit  du mod le, un mod le a  t  r alis  en partenariat avec le d partement du style de PSA. La sensibilit  au vent lat ral a  galement  t   tudi e. Il a  t  montr  que les montants arri res arrondis d t riorient les performances en vent lat ral. La compr hension des effets d'arrondi de la partie arri re des mod les de v hicule s'av re  tre valide malgr  la complexit  croissante des mod les. Enfin, des tests   l' chelle 1 ont confirm  les tendances observ es sur les mod les    chelle r duite.